T2R2 東京科学大学 リサーチリポジトリ
Science Tokyo Research Repository

論文 / 著書情報
Article / Book Information

題目(和文)	
Title(English)	Hydrogen Diffusion and Termination Effects in Hydrocarbon-Molecular-Ion Implanted Silicon Epitaxial Wafers for Advanced CMOS Image Sensors
著者(和文)	奥山亮輔
Author(English)	Ryosuke Okuyama
出典(和文)	学位:博士(工学), 学位授与機関:東京工業大学, 報告番号:甲第11599号, 授与年月日:2020年9月25日, 学位の種別:課程博士, 審査員:若林 整,筒井 一生,大見 俊一郎,宮島 晋介,角嶋 邦之
Citation(English)	Degree:Doctor (Engineering), Conferring organization: Tokyo Institute of Technology, Report number:甲第11599号, Conferred date:2020/9/25, Degree Type:Course doctor, Examiner:,,,,
学位種別(和文)	博士論文
Type(English)	Doctoral Thesis

Powered by T2R2 (Science Tokyo Research Repository)

Hydrogen Diffusion and Termination Effects in Hydrocarbon-Molecular-Ion Implanted Silicon Epitaxial Wafers for Advanced CMOS Image Sensors

by

Ryosuke Okuyama

Submitted to the
Department of Electrical and Electronic Engineering on July, 2020
in partial fulfillment of the requirements for the degree of
Doctor of Philosophy in Engineering

Author: ____

Department of Electrical and Electronic Engineering, July, 2020

Certified by: ____

Hitoshi Wakabayashi
Professor of Electrical and Electronic Engineering
Thesis Supervisor

Certified by: ____

Kazuo Tsutsui
Professor of Laboratory for Future Interdisciplinary Research of Science and Technology
Thesis Supervisor

Certified by: ____

Shunichiro Ohmi
Associate Professor of Electrical and Electronic Engineering
Thesis Supervisor

Certified by: ____

Kuniyuki Kakushima
Associate Professor of Electrical and Electronic Engineering
Thesis Supervisor

Certified by: ____

Shinsuke Miyajima
Associate Professor of Electrical and Electronic Engineering
Thesis Supervisor

Hydrogen Diffusion and Termination Effects in Hydrocarbon-Molecular-Ion Implanted Silicon Epitaxial Wafers for Advanced CMOS Image Sensors

by

Ryosuke Okuyama

Submitted to the
Department of Electrical and Electronic Engineering on July, 2020
in partial fulfillment of the requirements for the degree of
Doctor of Philosophy in Engineering

Abstract

Complementary Metal Oxide Semiconductor (CMOS) image sensor has been widely used for ubiquitous devices, such as smartphones and smart watches. In consumer markets, CMOS image sensors with high dynamic range are strongly demanded also with high sensitivity, high saturation signal and low noise. Especially, for automotive and surveillance systems, random noises caused by dark currents and random telegraph signals (RTS) are required to be reduced. To reduce the dark currents, the defects with deep energy level caused by metallic impurities are needed to be suppressed in the device active region during the fabrication processes. A gettering technology is well known to remove metallic impurity contaminations through device integration procedure, and also, a silicon epitaxial wafer technology are widely used for CMOS image sensors, to reduce the dark currents because of less crystal defects. Moreover, to reduce the dark currents and RTS noise simultaneously, the carrier generation from interface state traps at the interface between silicon dioxide (SiO_2) film and silicon (Si) substrate is needed to be reduced in the deep trench isolation (DTI) and transistor gate oxide. The interface state density (D_{it}) is reduced by hydrogen forming gas annealing (FGA) after back end of line (BEOL) processes, in which the silicon dangling bonds are terminated with hydrogen at the interface between the SiO_2 and Si called Pb_0 centers. However, the most of the hydrogen atoms are concerned to be trapped in multiple interconnect layers during the FGA. Consequently, it is possible to perform the FGA before BEOL processes, however, it has been reported that desorption of hydrogen from the interface between the SiO_2 and Si was observed due to thermal energies during the BEOL processes. To solve the above issues, new technologies are expected from the wafer side, independent of BEOL processes and the number of interconnect layers.

Therefore, I have developed the novel epitaxial wafer with hydrocarbon molecular ion implantation, and this thesis discusses comprehensive characteristics regarding the hydrogen termination effects because of this wafer.

First, the defects in hydrocarbon molecular ion implanted silicon wafer, which are different from that in monomer one, were observed even after the epitaxial growth. In addition, it is speculated using Technology Computer Aided design (TCAD) analysis that the carbon induced complexes trap the metallic impurities. In contrast, I found that hydrogen species are maintained in this region, such as a hydrogen reservoir.

This thesis further investigates the hydrogen diffusion behavior from the reservoir, in which two types of hydrogen diffusions from the implanted region of hydrocarbon molecular ions are discussed for the small and large thermal budget processes, respectively. In this small thermal budget, the activation energy of hydrogen dissociation from the implanted region was calculated as 0.76 eV, which corresponds to the activation energy of C-H_2 binding energy relating to the carbon-induced defects with hydrogen. In contrast of large thermal budget, the activation energies of hydrogen dissociation was calculated as 0.42 eV, which is close to the binding energy of oxygen and hydrogen (O-H). These results for small and large thermal budgets convince these molecular and atomic hydrogen diffusions from the implanted region.

Finally, this thesis discusses on the reduction of D_{it} at the interface between SiO_2 and Si, because of the hydrogen termination effects, by using capacitance voltage (C-V) and electron spin resonance (ESR) measurements.

These results in this thesis indicate that hydrocarbon molecular ion implanted epitaxial silicon wafer simultaneously achieves the high gettering ability for metallic impurities and the hydrogen termination effect for the SiO_2/Si interface. Therefore, I have conclude that the hydrocarbon molecular ion implanted epitaxial silicon wafer remarkably improves the dark currents and RTS noise, simultaneously. Eventually, there is no question that this wafer is able to be applied for not only CMOS image sensor but also any type of advanced LSI products.

Thesis Supervisor: Hitoshi Wakabayashi
Title: Professor of Department of Electrical and Electronic Engineering

Thesis Supervisor: Kazuo Tsutsui
Title: Professor of Laboratory for Future Interdisciplinary Research of Science and Technology

Thesis Supervisor: Shunichiro Ohmi
Title: Associate Professor of Department of Electrical and Electronic Engineering

Thesis Supervisor: Kuniyuki Kakushima
Title: Associate Professor of Department of Electrical and Electronic Engineering

Thesis Supervisor: Shinsuke Miyajima
Title: Associate Professor of Department of Electrical and Electronic Engineering

Acknowledgements

The support and encouragement of many individuals contributed to the successful completion of this work. I would like to express sincere gratitude to Professor Hitoshi Wakabayashi for providing technical guidance. I was very fortunate to have had the opportunity to learn from him. I would like to thank Professor Kazuo Tsutsui, Associate Professor Shunichiro Ohmi, Associate Professor Kuniyuki Kakushima and Associate Professor Shinsuke Miyajima for their comments, advice and helpful discussions on this thesis.

I would like to express deep gratitude to Dr. Hisashi Furuya, COO & President of SUMCO Corporation, Mr. Naoki Ikeda, Executive Officer of SUMCO Corporation and Dr. Kazunari Kurita, general manager of SUMCO Corporation for their management, helpful advice and encouragements of this study.

I would like to thank to Mr. Tadashi Ikejiri, General Manager of NISSIN ION EQUIPMENT CO.,LTD., Mr. Tsutomu Nagayama, Group Manager of NISSIN ION EQUIPMENT CO.,LTD., and Dr. Naoki Miyamoto of NISSIN ION EQUIPMENT CO.,LTD. for their continuous helps and contributions in this study.

I also would like to thank to Mr. Yoshihiro Koga, Mr. Hidehiko Okuda, Mr. Takeshi Kadono, Dr. Ayumi Onaka-Masada, Dr. Ryo Hirose, Mr. Satoshi Shigematsu, Mr. Koji Kobayashi, Dr. Akihiro Suzuki of SUMCO Corporation for their significant discussions and experimental advices.

Author has been strongly supported by my wife, Yukari, and daughter, Rin, and son, Aoi, and would like to thank them gratefully.

July 29th, 2020

Ryosuke Okuyama

Contents

1 Introduction **1**
1.1 Technical trends of CMOS image sensors . . . 1
1.2 Silicon wafer technology for CMOS image sensors . . . 9
1.3 Hydrocarbon molecular ion implantation technology . . . 12
1.4 Thesis Focus and Organization . . . 19

2 Analysis methodology **21**
2.1 Experimental procedure . . . 21
2.2 Analysis methods . . . 23
2.2.1 Secondary ion mass spectrometry (SIMS) . . . 23
2.2.2 Transmission electron microscopy (TEM) . . . 25
2.2.3 Technology computer aided design (TCAD) . . . 27
2.2.4 Quasi-static capacitance voltage (CV) measurement . . . 31
2.2.5 Electron spin resonance (ESR) . . . 33

3 CI-cluster formation in hydrocarbon-molecular-ion implanted region **35**
3.1 Introduction . . . 35
3.2 Experiments . . . 36
3.3 Defect formation behavior in the hydrocarbon-molecular-ion implanted region . . . 39
3.4 Mechanism of defect formation behavior in the implanted region of the hydrocarbon molecular ion . . . 44
3.5 Summary . . . 47

4 Diffusion behavior of hydrogen in small thermal budget **48**
4.1 Introduction . . . 48
4.2 Experimental methods . . . 51
4.3 Hydrogen diffusion behavior in hydrocarbon-molecular-ion implanted region . . . 52
4.4 Mechanism of hydrogen out-diffusion behavior in small thermal budget 61

4.5 Summary 64

5 Kinetic analysis of hydrogen diffusion behavior with TCAD simulation 65

5.1 Introduction 65
5.2 Theoretical and experimental methods 67
5.3 Trapping and diffusion behavior of hydrogen simulated by TCAD . . 70
5.4 Mechanism of hydrogen trapping and diffusion behavior 74
5.5 Summary 77

6 Hydrogen diffusion behavior in large thermal budget 78

6.1 Introduction 78
6.2 Experiments and analysis methods 81
6.3 Hydrogen diffusion behavior in hydrocarbon-molecular-ion implanted regions after high-temperature annealing 82
6.4 Model of hydrogen diffusion by reaction kinetic analysis 88
6.5 Mechanism of hydrogen diffusion in implanted region 91
6.6 Summary 97

7 Termination effect of hydrocarbon molecular ion implanted silicon wafers 98

7.1 Introduction 98
7.2 Experiments 100
7.3 Hydrogen termination effect of hydrocarbon molecular ion implanted wafer 102
7.4 Mechanism of hydrogen termination effect of hydrocarbon molecular ion 108
7.5 Summary 114

8 Conclusions 115

8.1 Thesis summary 115
8.2 Future technologies and directions 117
8.3 Conclusions on this thesis 118

List of Figures

1.1 CMOS image sensor market trend. 2
1.2 Schematic diagram of 4Tr pixel. 4
1.3 Schematic diagram of dark current components. 6
1.4 Temperature dependence of total dark current. 6
1.5 Relationship of dynamic range and noise floor. 7
1.6 Cross section of one pixel of CMOS image sensor. 8
1.7 Concept of gettering technology and process. 10
1.8 Issues of advanced CMOS image sensors. 11
1.9 Concept of proximity gettering sink using high-energy monomer ion implantation. 13
1.10 Surface interaction with silicon during gas cluster ion beam implantation. 13
1.11 Fabrication process of the hydrocarbon molecular ion implanted epitaxial wafer. 15
1.12 Concept of the hydrocarbon molecular ion implanted wafer. 17
1.13 Histogram of white-spots-counts after CMOS image sensor fabrication process on wafers with and without hydrocarbon-molecular-ion implantation. 17
1.14 Histogram of white-spots-counts after CMOS image sensor fabrication process on wafers with and without hydrocarbon-molecular-ion implantation. 18
1.15 Thesis structure. 20

2.1 Schematic diagram of analysis flow. 22
2.2 Schematic diagram of secondary ion generation in SIMS instrument. . 24
2.3 Schematic diagram of TEM. 26
2.4 Structures of (a) C_i and (b) C_iC_s. 29
2.5 Schematic diagram of (a) low and (b) high frequency CV measurement. 32
2.6 Schematic diagram of the Zeeman effect. 34
2.7 Schematic diagram of ESR analysis in this study. 34

3.1 Process and analysis flow diagram of this study. 38
3.2 XTEM images of C_3H_5-cluster-ion-implanted Si wafers with carbon doses of (a) 1.0×10^{15}, (b) 2.0×10^{15}, and (c) 3.0×10^{15} carbon atoms/cm^2. 40
3.3 SIMS profile of C_3H_5-cluster-implanted and monomer-carbon-implanted samples for carbon dose of 2.0×10^{15} carbon atoms/cm^2. . 40
3.4 XTEM images of carbon-monomer-ion-implanted Si wafers with carbon doses of (a) 1.0×10^{15}, (b) 2.0×10^{15}, and (c) 3.0×10^{15} carbon atoms/cm^2. 42
3.5 XTEM images of after epitaxial growth with carbon doses of (a) 1.0×10^{15}, (b) 2.0×10^{15}, and (c) 3.0×10^{15} carbon atoms/cm^2. (a) - (c) using C_3H_5 cluster size, (d) 2.0×10^{15} carbon atoms/cm^2 using C_2H_5 cluster size. 43
3.6 High-magnification XTEM images of carbon doses of (a) 1.0×10^{15} and (b) 3.0×10^{15} carbon atoms/cm^2 for after-epitaxial-growth samples. 43
3.7 HR-XTEM image and electron diffraction pattern from n-ED observation with carbon dose of 3.0×10^{15} carbon atoms/cm^2 for after-epitaxial-growth sample. 45
3.8 TCAD result by using KMC code of distribution for carbon (black) and Si self-interstitial (red) in implanted region of carbon cluster after epitaxial growth. 46

4.1 Process and analysis flow diagram of this study. 51
4.2 SIMS profile of hydrogen and carbon of as-implanted (solid lines) and annealed (dashed lines) samples with C_3H_5 dose of 3.3×10^{15} atoms/cm^2. 53
4.3 SIMS profiles of as-implanted sample and after 600°C annealing of sample with monomer hydrogen implantation. 53
4.4 Simulated damage profiles of C_3H_5 and monomer carbon implantation by TCAD simulator sentaurus process and SIMS profiles of carbon and carbon with hydrocarbon-molecular-ion. 54
4.5 SIMS profile of hydrogen after epitaxial growth with C_3H_5 dose of 3.3×10^{14} atoms/cm^2. 56
4.6 Dependence of hydrogen-peak concentration after epitaxial growth on C_3H_5 dosage. 56
4.7 SIMS profile of hydrogen after annealing at 300 to 900°C for 30 min at 200°C intervals. 57
4.8 Plot of integral values in 1.0 μm region around hydrogen peak after annealing from 600 to 900°C for 30 min. 57

4.9 Plots of logarithm of hydrogen concentration on vertical axis and annealing time on horizontal axis. 59
4.10 Arrhenius plot of reaction rate constant k. 60
4.11 HR-XTEM images of (a) low, (b) high magnification and (c) Electron diffraction pattern from n-ED observation with carbon dose of 1.0×10^{15} carbon atoms/cm^2 for after-epitaxial-growth sample. 63
4.12 Schematic of (a) hydrogen molecule at T_d site of unit cell of silicon crystal and (b) dissociation process of hydrogen molecule trapped at multi-vacancy. 63

5.1 The profile of carbon total (dotted line), C_3I_3 cluster (solid line), C_3I_2 cluster (solid line), and Ci (dashed line) after epitaxial silicon growth at 1100°C with C_3H_5 dose of 1.6×10^{14} molecular ions/cm^2 by TCAD simulation. 69
5.2 Depth profile of hydrogen after epitaxial silicon growth at 1100°C with SIMS analysis and TCAD simulation with C_3H_5 dose of 3.3×10^{14} molecular ions/cm^2. 71
5.3 Depth profile of hydrogen after 900°C, 60-min annealing in a nitrogen atmosphere with SIMS analysis and TCAD simulation with C_3H_5 dose of 3.3×10^{14} molecular ions/cm^2. 72
5.4 Dependence of hydrogen-peak concentration after epitaxial silicon growth at 1100°C and after annealing at 900°C for 60 min in a nitrogen atmosphere with TCAD simulation on C_3H_5 dose. 73
5.5 Simulated carbon (C), hydrogen (H), and silicon interstitial (I) profiles of C_3H_5-molecular ion implantation by TCAD simulation. . . 75
5.6 HR-XTEM images of (a) low and (b) high magnification with carbon dose of 3.3×10^{14} atoms/cm^2 after epitaxial growth and annealing at 900°C for 60 min sample. 76

6.1 Depth profiles of carbon and hydrogen by SIMS analysis after (a) ion implantation and (b) 30 min annealing at 600°C at the C_3H_5 dose of 6.6×10^{14} cluster atoms/cm^2. 83
6.2 Depth profiles of hydrogen after epitaxial growth at C_3H_5 doses of 1.6×10^{14} (dotted line) and 3.3×10^{14} (solid line) cluster atoms/cm^2. 84
6.3 Dependence of hydrogen peak concentration after epitaxial growth on C_3H_5 dosage. 84
6.4 SIMS profiles of hydrogen peak after epitaxial growth (solid line) and subsequent annealing for 30 min at temperatures 900°C (dashed line) and 1100°C (dotted line) at C_3H_5 dose of 3.3×10^{14} cluster atoms/cm^2. 85

6.5 Plots of hydrogen density that out-diffused obtained by the finite difference in integral values in a 1.0 μm region around the hydrogen peak concentration before and after annealing from 600 to 1100°C for 30 min. 87
6.6 Plots of hydrogen density in C_3H_5 implanted region after heat treatments at 800 to 1100 °C with heat treatment time on the horizontal axis and logarithm of hydrogen density on the vertical axis. 87
6.7 Fitting results for the ratio of D_0 to D_H at 800 to 1100°C. 89
6.8 Arrhenius plots of the reaction rate constants k_1 and k_2 of reactions expressed in reactions 6.1 and 6.2. 90
6.9 Carbon and hydrogen profiles after epitaxial growth at C_3H_5 dose of 1.6×10^{14} atoms/cm^2 obtained by SIMS analysis. 93
6.10 Profiles of total carbon (dotted line), C_3I_3 clusters (solid line) and carbon interstitials (C_i) (dashed line) after epitaxial growth at C_3H_5 dose of 1.6×10^{14} atoms/cm^2 obtained by TCAD simulation. 93
6.11 (a) low-magnification XTEM image and (b) HR-XTEM image of epitaxially grown sample. 94
6.12 HR-XTEM image of C_3H_5 implanted region and (b) KMC simulation result of CI clusters. 94
6.13 Depth profiles of carbon, oxygen and hydrogen by SIMS analysis after epitaxial growth. 96

7.1 Schematic of sample flow and structure. 101
7.2 C-V curve of theoretic calculation (black dotted line) and quasi static C-V measurement with the unannealed samples without C_3H_5 (blue dashed line) and with C_3H_5 (red solid line). 103
7.3 D_{it} without C_3H_5 (black circle) and with C_3H_5 samples (blue square) after 700°C annealing. 103
7.4 D_{it} at midgap with annealing temperature in without and with C_3H_5 implanted wafer. 104
7.5 ESR spectrum with C_3H_5 after annealing at 500°C for 30 min. 105
7.6 D_{it} vs density of Pb_0 center each annealing temperature in without and with C_3H_5. 107
7.7 D_{it} at the midgap of wafer with C_3H_5 implantation after 500, 600, 700, 800 and 900°C annealing. 109
7.8 Fitting result of the D_{it} plot from equation 7.5. 111
7.9 Arrhenius plot using L_1 for each temperature. 111
7.10 Schematic diagram of termination of Pb_0 center by molecular hydrogen diffused from C_3H_5-implanted region. 113

8.1 Thesis approaches and solutions. 115

List of Tables

1.1 Noise and causes of typical CMOS image sensors. 3

2.1 CI cluster complexes for Sentaurus process simulator. 29
2.2 Carbon cluster complexes calculated by Sentaurus process KMC. . . . 30

Chapter 1

Introduction

1.1 Technical trends of CMOS image sensors

In recent years, Complementary Metal Oxide Semiconductor (CMOS) image sensors have been used in consumer electronic devices such as digital cameras and smartphones. In addition, CMOS image sensors have been used in other fields such as automotive, monitoring cameras and medical applications. The global market for CMOS image sensors is growing significantly.

Figure 1.1 shows the dollar-based market growth of the CMOS image sensor market trend [1]. Large growth is forecast from 2019 onwards, indicating that the product group is expected to continue to grow in the future. The CMOS image sensors market has been growing by mounting it in consumer electronic devices such as digital cameras and smartphones. Furthermore, in recent years, CMOS image sensors have also been applied to the term of automotive and medical application. Therefore, the market of CMOS image sensors is expected to grow significantly in the future. In addition, consumer market strongly demands more high sensitivity and more high speed image data processing for achieving fabricate high performance CMOS image sensors. Although CMOS image sensors are used in various fields today, the concept of a solid-state image sensor was shown by a photo scanner of SR Morrison in 1963 and a scanister of IBM in 1964 [2, 3]. However, it has been technically difficult to achieve the number of pixels required for a practical image sensor on a silicon substrate with a high yield. In 1970, Bell Labs W. S. Boyle and G. E. Smith developed a charge coupled device (CCD) [4]. CCDs can transfer signal charges spatially distributed on the surface of a silicon semiconductor while maintaining their positional relationship. As a result, the development of solid-state imaging devices will begin rapidly. Kosonocky in *et al.* proposed an overlapping gate electrode structure [5]. In addition, Walden in *et al.* proposed a buried channel structure as a structure for improving the charge transfer efficiency of a CCD [6].

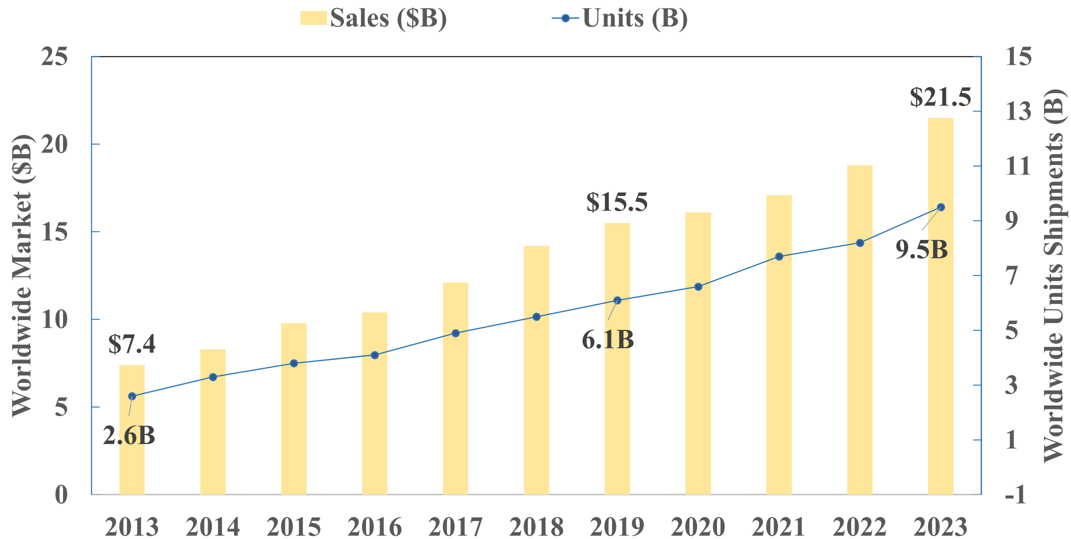

Figure 1.1: CMOS image sensor market trend [1].

Furthermore, for the detection of signal charges, Kosonocky in *et al.* indicated the advantage that the charge detection method using a floating diffusion layer (Floating Diffusion) structure [7] can improve the detection sensitivity by reducing the capacitance of the floating diffusion layer. On the other hand, regarding MOS imaging devices, a video camera was released using MOS imaging devices in 1981. However, the parasitic capacitance of the column readout line and the row readout line increases as the number of pixels increases in the MOS imaging device. Therefore, the sensitivity of MOS image sensor is lower than that of the CCD image sensor, and the image quality is degraded due to the fixed pattern noise. After that, the improvement of MOS imaging devices was continued, but they were not widely used due to poor compatibility with the CMOS LSI process. CMOS-APS (Active Pixel Sensor), the prototype of a CMOS image sensor, was reported by E.R. Fossum in *et al.* in 1993 [8]. This device has a 3Tr configuration in which the photodiode potential is read out by a source follower amplifier. It could be manufactured with a single power supply, low power consumption, high speed by reading signals in parallel in row units, and a standard CMOS process. In addition, it attracted attention because of its advantages such as system-on-chip being easy [9]. Since CMOS-APS amplifies signals for each pixel, it has the advantage of being less susceptible to noise on vertical and horizontal signal lines. However, the fixed pattern noise due to the variation of the amplifier for each pixel and the dark current noise of the photodiode are large. Therefore, there was a difference in sensitivity and image quality from CCD, and these solutions are issues of CMOS-APS. With regard to fixed pattern noise, noise equivalent to that of CCD has been reduced by the configuration of a column-parallel charge-region-difference-type noise canceling circuit and AD converter. Also, regarding the random noise, White in *et al.* developed a correlated

Table 1.1: Noise and causes of typical CMOS image sensors.

	Noises	Causes
Random noise	kTC noise	During charge-voltage conversion
	1/f noise	Interface states of MOS transistor
Fixed pattern noise	Dark current noise	Interface states in surface of photodiode
	Variation of the amplifier	Variation of the MOS transistors

double sampling (CDS) method to reduce the kTC and 1/f noise [10]. This circuit can reduce kTC and 1/f noise and is still widely used. To improve the dark current noise of the photodiode, a pinned photodiode and the development of a 4Tr pixel using a complete transfer type pinned photodiode have suggested for the image quality equivalent to that of CCD [11, 12]. Figure 1.2 shows schematic diagram of 4Tr pixel. The pixel of 4Tr CMOS image sensors is composed of a pinned photodiode (PPD) and four transistors (reset transistor: M_{RST}, charge transfer electrode: TX, amplification transistor: M_D, row selection transistor: M_{RS}), and floating diffusion (FD) [13]. The signal charge stored in the photodiode is transferred from PPD to FD by TX. Just before that, FD is initialized to the reset voltage. The initialization voltage in the FD and the voltage after signal charge transfer are read out as voltage signals by COLUMN outside the M_D and pixel via M_{RS}. The noise generated when resetting the FD is called reset noise (kTC noise). Complete charge transfer is achieved by appropriate design of the impurity profile under PPD and TX so that there is no potential barrier in the charge transfer path from PPD to FD. This complete charge transfer means that all the signal charges accumulated in the PPD are transferred to the FD. Thus, the 4Tr embedded photodiode pixel has been adopted as a basic configuration of a CMOS image sensor because of its excellent features of low noise, low dark current, and no image lag. Table 1.1 shows the noise and causes of typical CMOS image sensors.

Although the complete transfer type pinned photodiode structure cannot be realized by the standard CMOS process, the CMOS process has been modified to improve sensitivity and image quality. In 2004, a 2-megapixel CMOS-APS was developed, enabling image quality comparable to CCD. As a result, competition with CMOS-APS and CCD has begun in the high-end camera market, where CCD image sensors have been dominant until now. Furthermore, the reduction in the light utilization rate due to the miniaturization of pixels has been greatly improved, and high sensitivity has been achieved even when the chip size and pixel size are

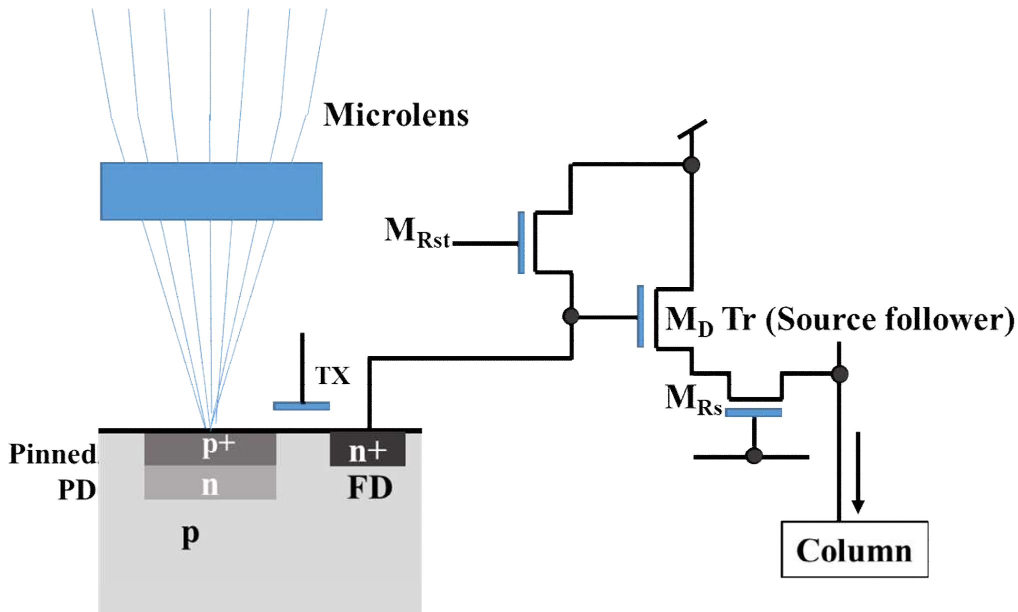

Figure 1.2: Schematic diagram of 4Tr pixel.

reduced. However, one of the features of manufacturing technology required for CMOS image sensors is that "pixel defect" control is very important. The defect affects the performance of the solid-state imaging device, such as "pixel defect" represented by "white spot defects". Particularly in an image sensor for human vision, it is necessary to suppress the number of white spots in the screen to less than ppm for all pixels. In addition, since it is not possible to introduce a redundant circuit commonly used in a memory device, all the pixels need to be pixel defect free.

A schematic image of the PD is shown in Figure 1.2 In the PD, photoelectric conversion is performed by generation and separation of electrons and holes using energy obtained by absorbing incident light. The light intensity is determined by the density of electrons and holes generated at this time. Therefore, it is important to increase the sensitivity of the CMOS image sensor by converting the incident light energy into a pair of electrons and holes without waste and extracting this pair as an electrical signal. White spot defects occur in which a pair of electrons and holes is formed even when light is not incident due to a deep energy level in the band gap of a silicon crystal. Thus, it is called dark current because it is a current generated through deep energy levels when no light is incident.

In CMOS image sensors, it is known that the factor of the dark current is classified by three; surface generation current, bulk generation current and diffusion current [13]. The surface generation current is caused in the surface of PD or SiO_2/Si interface at isolation region. The amount of surface current at a room temperature

is known highest in the dark current. The surface current can be suppressed by making an inversion layer at the surface of the PD such as PPD structure [11, 12]. However, the current generated through the SiO_2/Si interface in the isolation region is a problem of dark current due to surface generation current. The surface generated current is expressed by the following equation

$$J_{gen,surf} = qs_0\frac{n_i}{2}. \tag{1.1}$$

The $J_{gen,surf}$ is the surface generated current. q is quantity of electricity. s_0 is surface recombination rate. n_i is intrinsic carrier density.

The bulk generation current is caused by deep energy levels formed by the metallic contaminations or crystal defects. The bulk generation current is expressed by the following equation

$$J_{gen,bulk} \propto exp(\frac{E_g/2 + |E_t - E_i|}{k_B T}). \tag{1.2}$$

The $J_{gen,bulk}$ is bulk generation current. E_t is trap energy. E_i is fermi energy. The bulk generation current is much higher than diffusion current at room temperature.

The diffusion current is caused by the diffusion of minority carrier from the bulk of silicon substrate to the PD. The diffusion current is expressed by the following equation

$$J_{diff} \propto exp(\frac{E_g}{k_B T}). \tag{1.3}$$

The J_{diff} is the diffusion current. E_g is bandgap energy. k_B is Boltzmann constant. The amount of this current is the smallest in the dark current at a room temperature.

Equations 1.2 and 1.3 show the temperature dependence of the surface/bulk generation current and the diffusion current. The surface/bulk generation current is dominant at low temperatures, and the diffusion current is dominant at high temperatures. Dark current is determined by the above three current components. Figure 1.3 shows the schematic diagram of dark current components. Assuming that the surface generated current is almost suppressed by the PPD structure, it is known that it has a temperature dependence as shown in Figure 1.4.

Therefore, considering the imaging at room temperature, it is important to reduce the bulk generation current. The cause of the bulk production current is the deep level formed in PD. The deep level is formed by metal impurities or crystal defects. Crystal defects have been solved by applying a silicon epitaxial wafer having high crystallinity. The main issue is dark current due to deep levels formed by metal impurities, and their reduction has been performed. Therefore, a ppm level of the

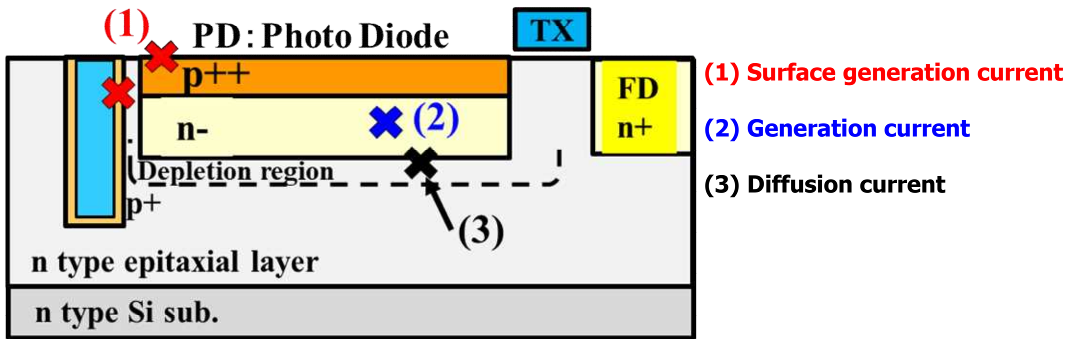

Figure 1.3: Schematic diagram of dark current components.

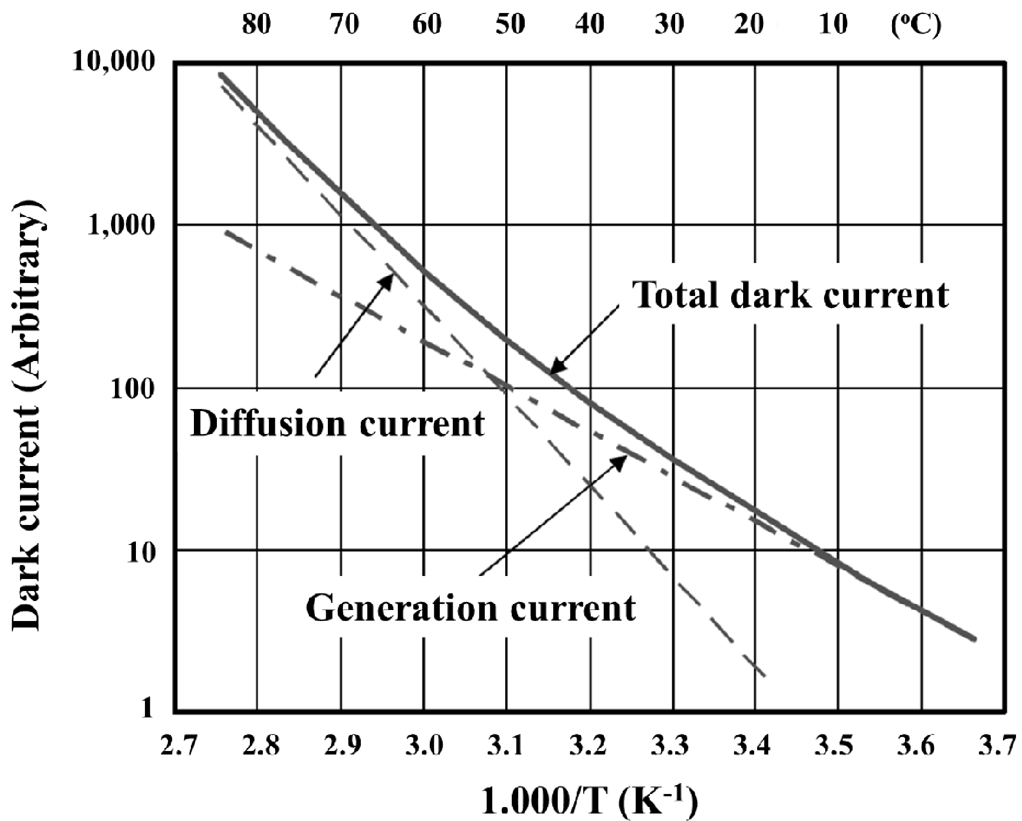

Figure 1.4: Temperature dependence of total dark current.

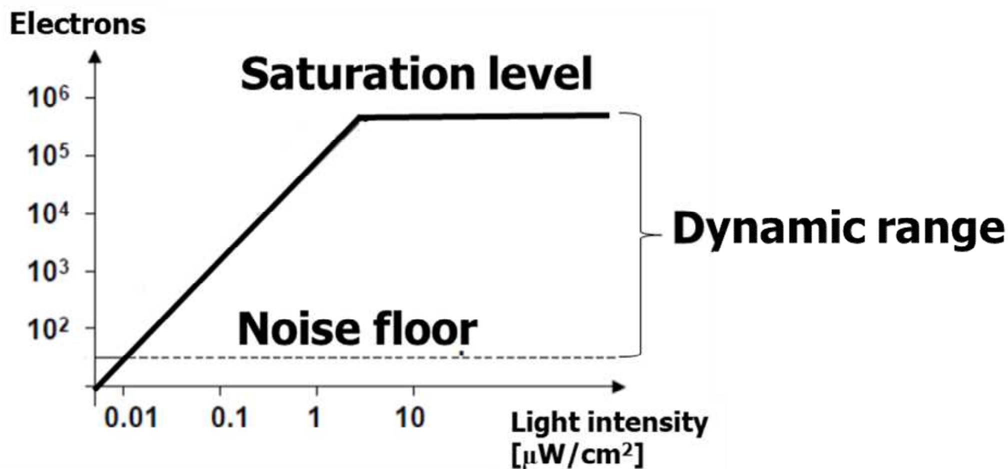

Figure 1.5: Relationship of dynamic range and noise floor.

metal contamination required for the general purpose CMOS manufacturing process is required.

However, in recent years, the surface generated current caused by the SiO_2/Si interface has an issue due to the suppression of other dark current components.

This is due to the fact that human vision is very sensitive to periodic noise and defects. Furthermore, the product performance indicators of CMOS image sensors for automotive use include the expansion of the dynamic range at low illumination (at night) and the improvement of noise characteristics such as RTS noise. Figure 1.5 shows the relationship of dynamic range and noise floor. The dynamic range is determined by the ratio of saturation level and noise floor. Thus, noise reduction is especially important at low illumination.

There have been many reports of R&D results aimed at improving these two product performance indicators [14]. Optimization of Full Well Capacitance (FWC) in PPD and FD transfer transistors that constitute one pixel of a CMOS image sensor and noise generated from these circuits in order to achieve high dynamic range and low noise characteristics has been an important issue. Figure 1.6 shows the cross-sectional structure of one pixel of a CMOS image sensor. One pixel is composed of four transistors including PPD and FD [15]. The performance index of a CMOS image sensor is dark current random telegraph signal noise (DC-RTS) generated from PPD and source follower random telegraph signal (SF-RTS) noise generated from an FWC circuit constituting a transfer transistor. It is understood that SF-RTS noise is dominant in noise generated from circuits [15] Here, RTS noise in the field of semiconductor devices refers to a phenomenon in which a current flowing between a source and a drain fluctuates randomly when a MOS-FET is turned on, and is called SF-RTS noise. According to previous research, the cause of

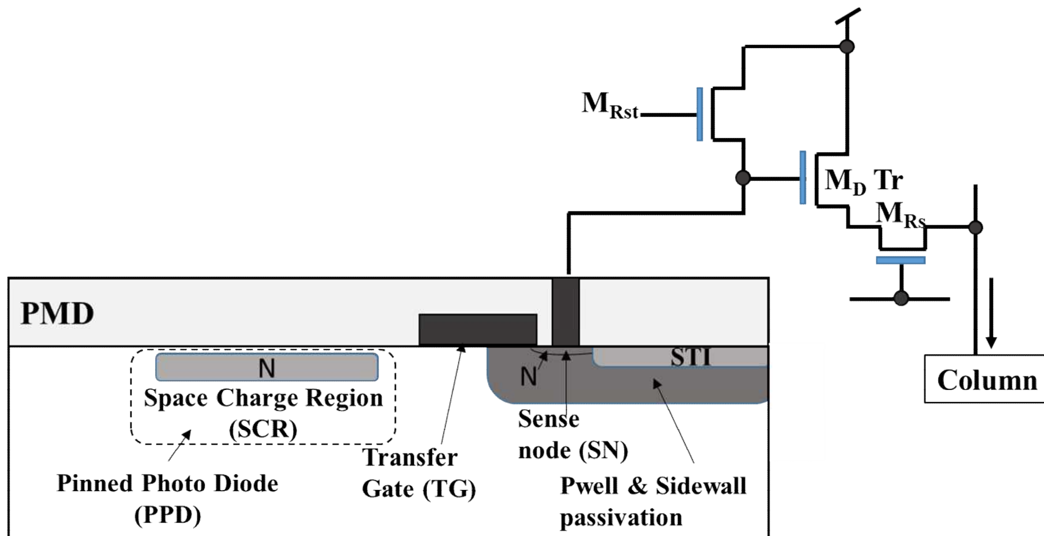

Figure 1.6: Cross section of one pixel of CMOS image sensor [15].

SF-RTS noise is that the current drifting between the source and drain is captured and emitted by a dangling bond-induced defect (*e.g.*, Pb center) located at the interface between the transistor and the gate oxide film. It is understood that the main factor is that the current between the source and the drain fluctuates. On the other hand, the main cause of DC-RTS noise generated by CMOS image sensors is not always clear, and research for elucidating the origin is being vigorously pursued. In order to improve RTS noise, it is necessary to reduce interface state defects generated at the interface of the gate oxide film of the transfer transistor, which is the main cause of noise generation, and dangling bonds generated at the SiO_2/Si interface by low-temperature hydrogen sintering has been inactivated electrically. However, with the adoption of the CMOS image sensor, it tends to be difficult to thermally diffuse hydrogen to the vicinity of the interface in the hydrogen sintering process near the post-process due to the multilayer film in the mounting and wiring process. Furthermore, three-dimensional transistors such as FinFET will be adopted as the logic circuit for scaling. Even in that case, there is a concern that the interface state traps will increase.

Therefore, it is conceivable that CMOS image sensor manufacturers are also working on the development of techniques for inactivating RTS noise and interface state defects due to miniaturization. As above-mentioned, in the manufacture of a CMOS image sensor, there are always issues of managing heavy metal contamination, reducing crystal defects, and inactivating interface state defects with higher performance. The next section describes silicon wafer technology to address these issues.

1.2 Silicon wafer technology for CMOS image sensors

Electrical characteristics of semiconductor devices such as pn junction leakage current, recombination lifetime, gate oxide breakdown voltage [16] strongly influences heavy metal impurities in device processes (*e.g.*; oxidation, diffusion annealing, plasma etching and ion implantation). For this reason, cleanliness of the device process has been developed since the late 1980s. However, even in the current 300 mm ULSI (Ultra Large Scale Integration) manufacturing line, there is a concern about heavy metal impurities of the active layer of the semiconductor device. Therefore, gettering techniques for trapping and removing heavy metal impurities from the device active layer have been developed in order to avoid the influence of heavy metal contamination on the electrical characteristics of semiconductor devices [16–22].

In the past, the word "gettering" was used as a process technology to trap and remove heavy metals generated in the device process by the polysilicon deposited on the backside of the wafer in the diode manufacturing process [17]. In general, when the process temperature is high, heavy metal impurities generated in the device process diffuses in the silicon crystal due to a large diffusion coefficient, and out-diffuses the front or back surface of the wafer. Then, precipitates are formed due to a decrease in solid solubility as the process temperature decreases. These precipitates can be a factor of forming secondary defects and a major factor of degrading the electrical characteristics of the device. Therefore, the primary purpose of gettering is to remove metal impurities that may form electrically active defects from the device active layer region and to achieve a clean device active layer.

The technology to achieve these is called gettering technology. Gettering technology consists of three processes: (1) removing and releasing heavy metals from the wafer surface; (2) diffusing the removed heavy metals into the gettering layer; (3) trapping them. Figure 1.7 shows the concept of gettering technology and process [16–22]. The gettering technology is a relaxation type gettering in which a metal element once dissolved in a substrate during a high-temperature annealing becomes supersaturated in the cooling process and precipitates on a gettering sink. Another is segregation-type gettering, in which the metal impurities segregates toward the higher solid solubility due to the difference in solid solubility between the silicon wafer and the gettering sink.

An example of the gettering method is intrinsic gettering (IG) using a bulk micro defect (BMD) of an oxygen precipitate formed on a silicon substrate as a gettering sink. Another example is extrinsic gettering (EG), which forms a gettering

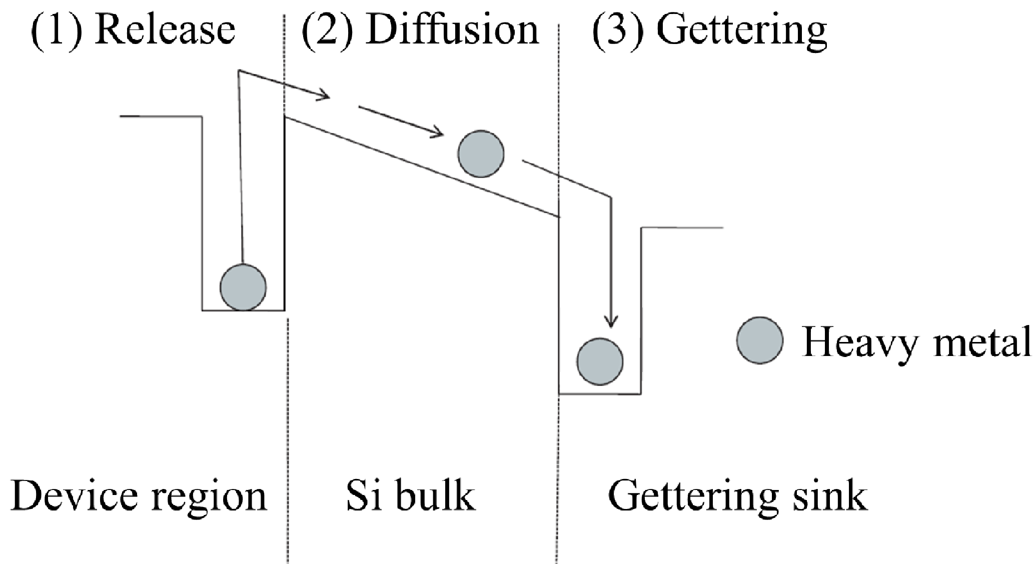

Figure 1.7: Concept of gettering technology and process.

sink by phosphorous ion implantation or poly-silicon (Poly Back Seal: PBS) on the backside of the substrate. The IG method by BMD is a gettering technique utilizing the fact that high-concentration oxygen is dissolved in a silicon wafer from a quartz crucible when manufactured by the CZ method. BMDs are nucleated by annealing at 700 to 900°C and then grown by annealing above 1000°C. The BMD is an oxygen precipitate, and when the BMD forms a strain field with the base silicon, the metal impurities is gettered in the strain field. The IG method is known to be a relaxed gettering method. On the other hand, as the EG method, a PBS method using poly-silicon formed on the back surface of the gettering method is well known. The PBS method is segregation-type gettering in which gettering is performed by segregation of a metal impurities having a higher solid solubility in poly-silicon than a silicon substrate. The above-mentioned gettering technique is a technique applied to a silicon wafer in order to remove the influence of metal impurities in a device process, and is a technique that has contributed to an improvement in yield. However, in recent years, the growth of oxygen precipitates (Bulk Micro Defect: BMD) formed in the wafer has been suppressed along with the low-temperature and short-time annealing in the semiconductor manufacturing process. In addition, due to the decrease of gettering sinks due to the thinning of silicon wafers in the post-device process, it is difficult for conventional gettering technology to show sufficient gettering effect on heavy metal impurities [23]. Therefore, the development of new gettering technology that can solve these technical issues has been required. Furthermore, CMOS image sensors require a different approach to gettering. A dark current characteristics are well known as the imaging characteristics of CMOS image sensors [24]. Figure 1.8 shows the issues of advanced CMOS image sensors.

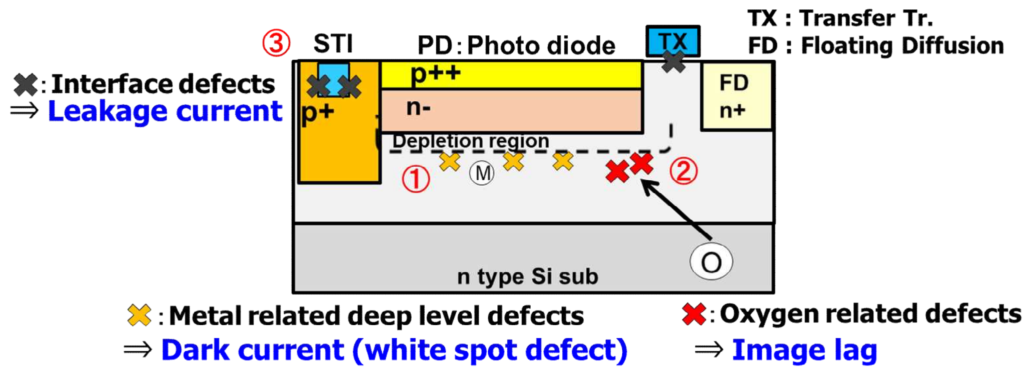

Figure 1.8: Issues of advanced CMOS image sensors.

It is understood that the dark current is generated by heavy metal impurities in the CMOS image sensor manufacturing process, where recombination centers are formed in the space charge region of the photodiode constituting the sensor, and are caused by bulk generation current from those deep energy levels [25, 26]. For this reason, in order to improve the imaging characteristics, it is necessary to control heavy metal impurities resulting from the device manufacturing process. Also, during the CMOS image sensor fabrication process, oxygen dissolved in the Si wafer substrate out-diffuses into the space charge region of the photodiode to form electrically active defects such as potential pockets. This has a negative effect on complete transfer and is a factor that degrades pixel quality such as "image lag" [12]. In addition, Shallow Trench Isolation (STI) and Deep Trench Isolation (DTI) are used as isolation between photodiodes and transfer transistors. The silicon dangling bonds at the interface of Si and SiO_2 in STI or DTI forms an interface state, which generates surface generation current of the dark current. Therefore, high-sensitivity CMOS image sensors require gettering wafers that can not only reduce heavy metal impurities in the device manufacturing process but also reduce substrate oxygen and interface states. Furthermore, a device for reducing interface state generated in the isolation region is an essential requirement for improving the performance of the CMOS image sensor. Thus, there is a demand for the development of a new gettering technology that can contribute to improvement these technical issues.

1.3 Hydrocarbon molecular ion implantation technology

As mentioned in the previous section, CMOS image sensors require new gettering technology. The reason is that the low-temperature and short annealing time during the device process make it difficult to grow BMD in the silicon wafer. In addition, due to the decrease of gettering sinks and the thinning of silicon wafers in the back end of line (BEOL) process, it is difficult for conventional gettering technology to show sufficient gettering effect on heavy metal impurities [23]. Furthermore, in the case of a CMOS image sensor, an epitaxial wafer (mainly an n/n- epitaxial wafer) is used as a silicon wafer. There has been a tendency to form a photodiode with a low concentration and a deep p-layer (deeper 3 μm from the surface) in order to improve the imaging characteristics. Therefore, a gettering technology that forms a gettering sink directly under the device active region by high-energy ion implantation has been reported in previous study [27]. Previous study has reported a technique using high-energy monomer carbon ion implantation in order to form a gettering sink beneath the space charge region [27,28]. Figure 1.9 shows the concept of proximity gettering sink using high-energy monomer ion implantation. However, since implantation defects are formed in these silicon wafers, a recovery annealing is required, and there is a concern that wafer manufacturing costs will increase. Therefore, I studied a new gettering technology that does not require a recovery annealing and can form a gettering sink closer to the device active region than the conventional gettering technique.

Thus, I focused on molecular ion implantation technology. The collision phenomenon of molecular ion with the silicon wafer surface layer is implanted into the cascade while colliding with silicon atoms according to the two-body collision model. Compared with monomer ion implantation, molecular ion implantation is known to be implanted near the surface by the many-body collision effect [29].

Yamada et. al. has developed the gas cluster ion beam [29]. Figure 1.10 shows the surface interaction with silicon during gas cluster ion beam implantation. However, it is difficult to apply the method to a CMOS image sensor because a large cluster ion (molecular ion) implantation causes a large damage to the surface layer and a crystal defect is formed. I focused on small-sized molecular ions, and considered to apply them to gettering sinks in a very shallow region on the wafer surface.

I have developed a gettering technique using hydrocarbon molecular ion implantation [30]. In hydrocarbon molecular ion implantation, a hydrocarbon compound composed of carbon and hydrogen atoms is ionized using thermal

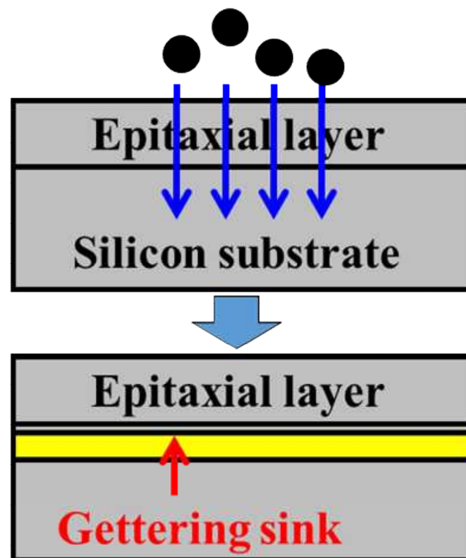

Figure 1.9: Concept of proximity gettering sink using high-energy monomer ion implantation.

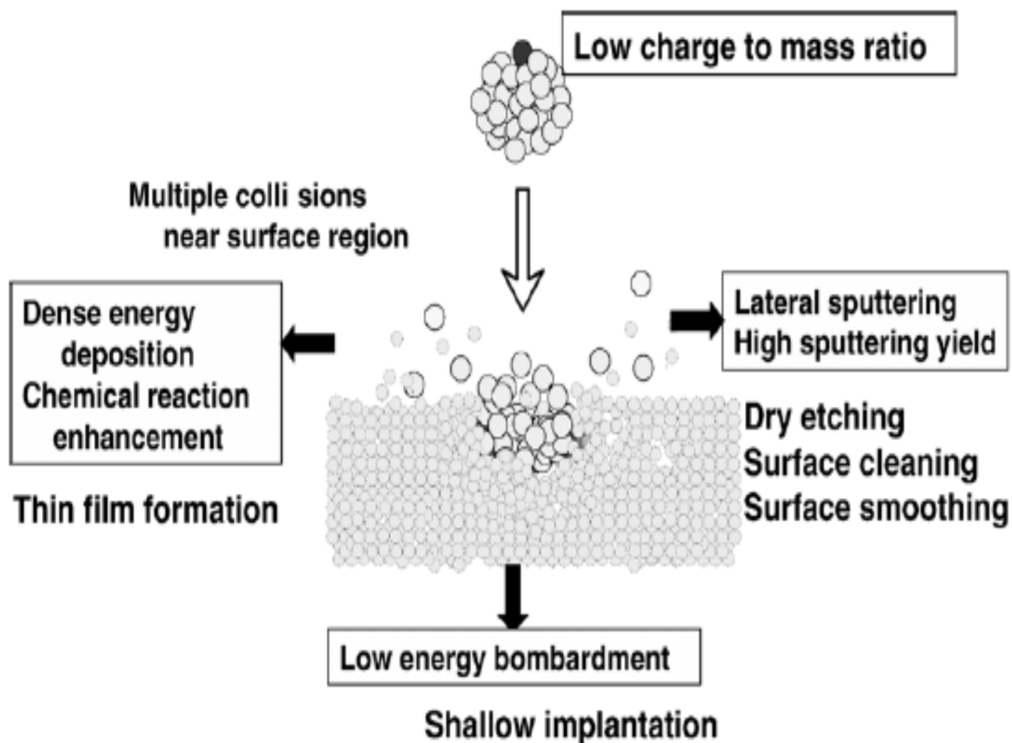

Figure 1.10: Surface interaction with silicon during gas cluster ion beam implantation [29].

electrons by electron bombardment and implanted into the silicon surface. In addition, there are three characteristics of hydrocarbon molecular ion implantation technology. First, even if ions are implanted at a high accelerating voltage, they can be equally divided by the mass number or the number of atoms, so that the implantation energy per atom is low and the implanted region can be formed in a shallow region. The following equation shows the energy distribution of molecular ion implantation.

$$E_M = E\frac{M}{M_{molecular}}. \tag{1.4}$$

E_M is the energy distributed to one atom. E is the implantation energy applied to the molecular ions. M is the atomic weight of the distributed ions. $M_{molecular}$ is the total mass of the molecular ion.

Second, compared to monomer ion implantation, multiple atoms bonded in a molecular ion can be transported at once. An improvement in throughput can be expected when considering productivity. Third, if an ion source is composed of multi-element atoms, it is possible to implant multiple types of elements simultaneously, so that a highly flexible ion source can be designed. The biggest feature of a hydrocarbon molecular ion implanted silicon wafer is that the amount of damage to the silicon single crystal is small because the implantation energy is low acceleration energy. Thus, a epitaxial growth is possible without recovery annealing. In addition, secondary defects due to ion implantation extended defects generated is not formed in the implanted region of hydrocarbon molecular ion. Consequently, it is possible to form a gettering sink by the implanted region of hydrocarbon molecular ion beneath the epitaxial layer. Figure 1.11 shows the fabrication process of the hydrocarbon molecular ion implanted epitaxial wafer.

The novel hydrocarbon molecular ion implanted silicon epitaxial wafer has three unique characteristics. The first is the high gettering ability for heavy metal impurities due to the implanted region of hydrocarbon molecular ion formed beneath the epitaxial layer [30–35]. Second, oxygen out-diffused from the silicon substrate to epitaxial layer is trapped in the implanted region of hydrocarbon molecular ion [30, 32]. Third, a termination effect on interface state is expected owing to the hydrogen in the hydrocarbon molecular ions trapped in the implanted region during the device fabrication process [36]. In addition, the implanted region of hydrocarbon molecular ion traps hydrogen after epitaxial growth, and the dissociation behavior upon subsequent annealing has been demonstrated. The above hydrogen diffusion behavior has not been reported in previous studies regarding IG wafers [37]. Figure 1.12 shows the concept of the hydrocarbon molecular ion implanted epitaxial wafer. In particular, the gettering ability of the novel silicon wafer have been investigated

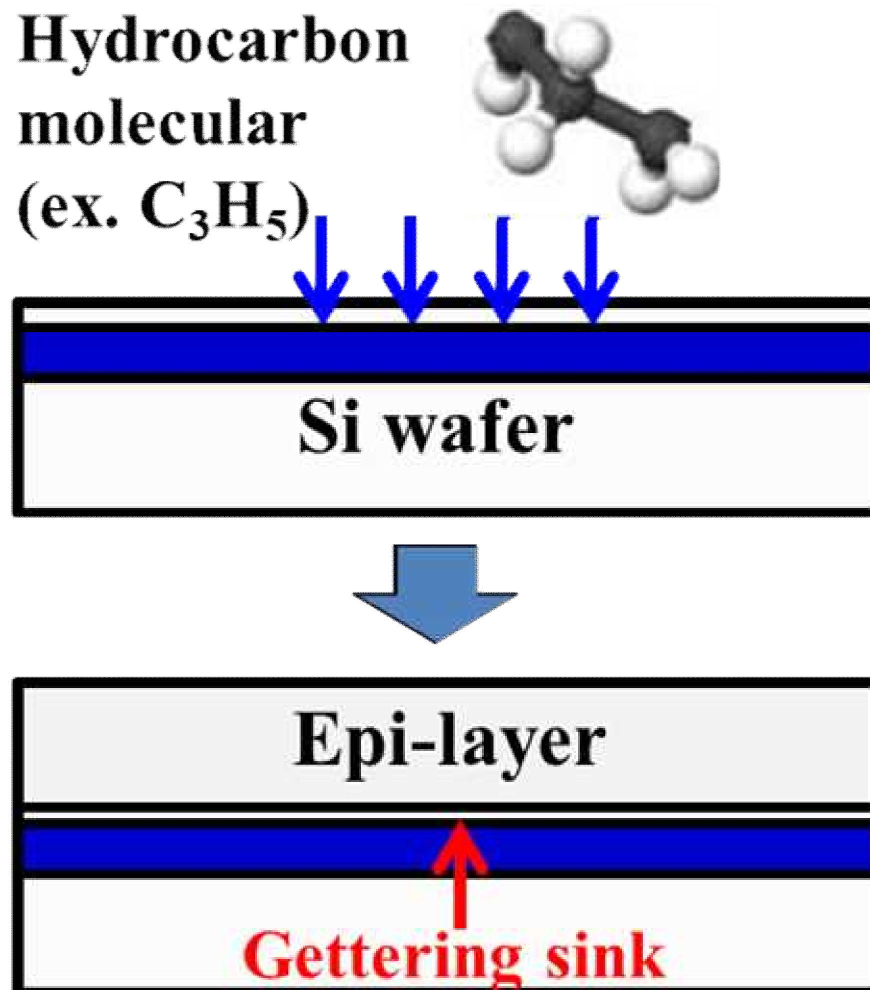

Figure 1.11: Fabrication process of the hydrocarbon molecular ion implanted epitaxial wafer.

in previous studies [30–35]. Those studies have reported that the carbon complexes is formed in hydrocarbon-molecular-ion implanted region [30, 34]. The carbon complexes have the gettering ability for metal impurities and oxygen. In addition, it has been reported that oxygen affects metal gettering, and it is known that the lower the oxygen gettering concentration in the carbon complexes, the higher the gettering ability for metal impurities [34, 35, 38]. Previous studies have already reported this novel silicon wafer improved of CMOS device key parameter such as dark current and white spot defect using CMOS image sensor manufacturing line [31, 39]. The white-spots of sensors with hydrocarbon molecular implantation were substantially fewer than those of the sensor fabricated without the implantation, as shown in Figure 1.13. Here, there is a concern that the shallow level formed by the gettered metal impurities may affect the substrate electrically [40]. However, since the concentration of the gettered metal is about one order of magnitude lower than the concentration of the dopant in the silicon wafer, it is considered that there is no influence of the gettered metal impurities.

Furthermore, Yamaguchi demonstrated that these novel silicon epitaxial wafers reduce the dark current due to the interface state defects at the SiO_2/Si interface [41]. Figure 1.14 shows the interface state related white spots defects of CMOS image sensors. The interface state related white spots defect of IG wafer did not decrease, but that of hydrocarbon-molecular-ion implanted epitaxial wafer was decreased. This phenomenon is considered to be due to the hydrogen termination effect of hydrocarbon-molecular-ion implanted epitaxial wafers. Gettering capabilities for metals and oxygen have been analyzed in previous studies [30, 31, 33–35]. However, the dissociation and diffusion behavior of hydrogen in the novel wafers have not been clarified in detail. In addition, they do not clearly show that hydrogen termination mechanism of SiO_2/Si interface after isochronal annealing.

It is extremely important to clarify the mechanism of the hydrogen termination effect of the novel wafer for improving the electrical performance of advanced CMOS image sensors. The hydrogen diffusion behavior in an implanted region of hydrocarbon-molecular-ion, which has never been reported in the past, is also an important both applied and fundamental material science.

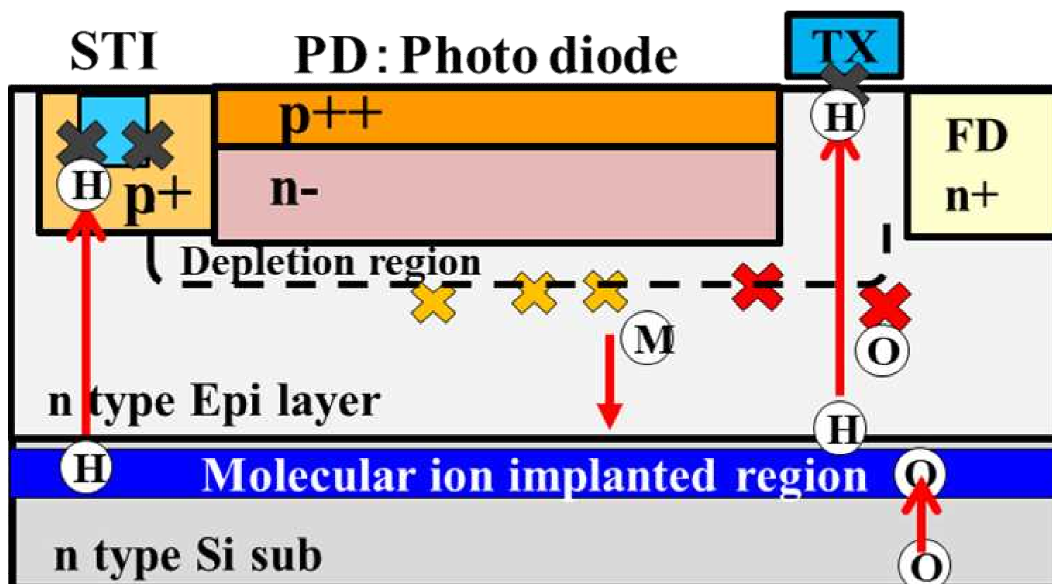

Figure 1.12: Concept of the hydrocarbon molecular ion implanted wafer.

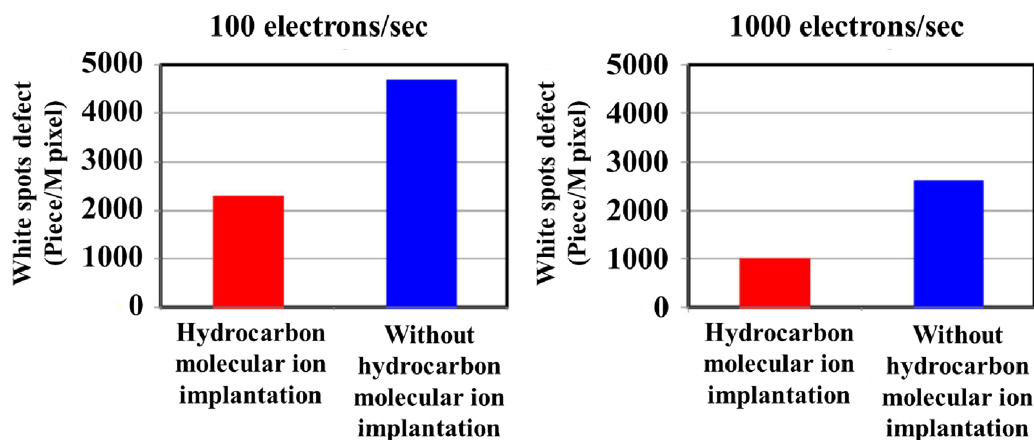

Figure 1.13: Histogram of white-spots-counts after CMOS image sensor fabrication process on wafers with and without hydrocarbon-molecular-ion implantation.

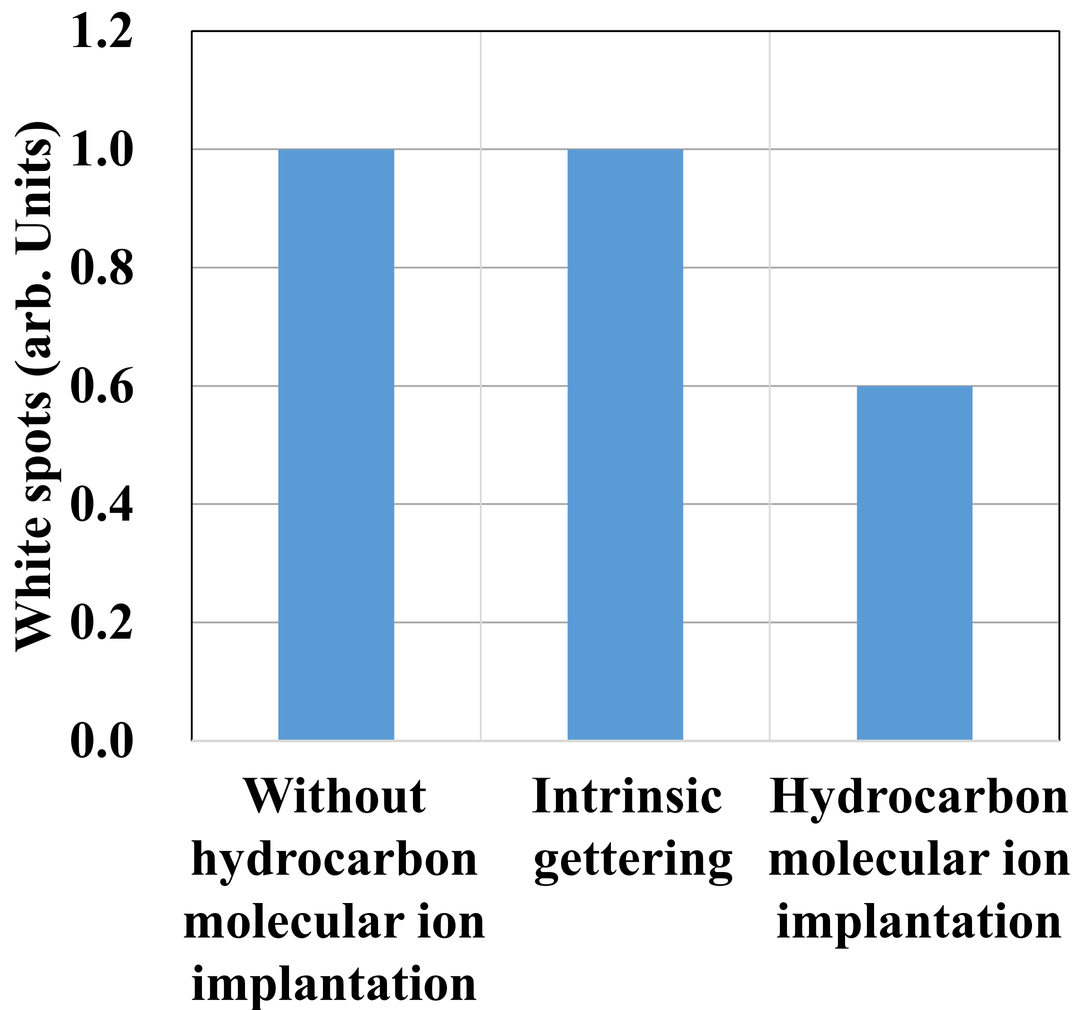

Figure 1.14: Histogram of white-spots-counts after CMOS image sensor fabrication process on wafers with and without hydrocarbon-molecular-ion implantation.

1.4 Thesis Focus and Organization

As mentioned in the previous section, improving noise in recent CMOS image sensors is an important technical issue. Therefore, I have developed alternative solution for technical issue of CMOS image sensor fabrication using hydrocarbon molecular ion implantation. The novel silicon wafer has three unique silicon wafer characteristics such as high gettering capability for metallic impurity, oxygen out-diffusion barrier effect and hydrogen storage effect of hydrocarbon implanted region. This wafer has already been reported to use CMOS image sensor manufacturing lines to dramatically improve key characteristics of CMOS image sensors, such as dark current and white spot defects. Furthermore, it has been reported that the white spot defect caused by the interface state of a CMOS image sensor can be reduced by the hydrogen storage effect, which is the most unique characteristic of a hydrocarbon molecular ion implanted silicon wafer. This is an important characteristic that greatly contributes to solving the technical issues of CMOS image sensors caused by the SiO_2/Si interface state. Further, it is known that hydrogen in a silicon wafer is easily diffused at a low temperature. There has been no report of a diffusion behavior in which hydrogen is once captured like a hydrocarbon ion implantation region and then out-diffused by additional annealing.

However, the mechanism of hydrogen termination by a hydrocarbon molecular ion implanted wafer has not been clarified. There are no reports of direct observation of the reduction of the interface state density. It is important to clarify and understand the mechanism of these hydrogen storage effects and hydrogen termination effects in improving the performance of CMOS image sensors that will be applied to various applications in the future. It is also important research for industrial application and basic studies. Figure 1.15 shows this thesis structure.

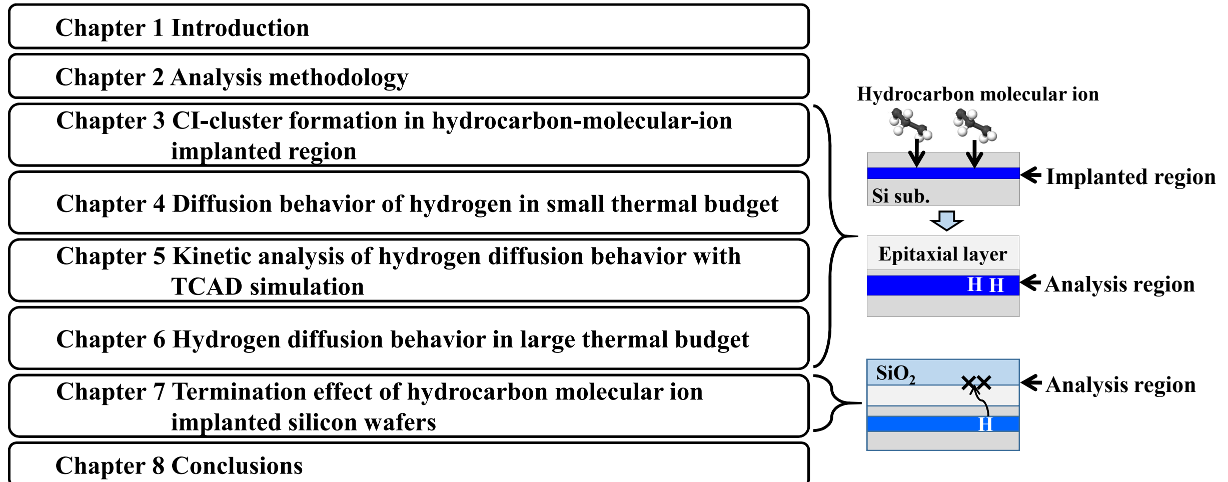

Figure 1.15: Thesis structure.

The purpose of this study was to clarify the hydrogen adsorption/desorption behavior and its hydrogen termination effect on hydrocarbon molecular ion implanted epitaxial wafers. First, the defects of the hydrocarbon molecular ion implanted region was observed. Next, an experiment and a kinetic analysis of the diffusion behavior of hydrogen in the implantation region during low-temperature short-time heat treatment were performed. In addition, the binding state of hydrogen in the implantation region was examined from theoretical analysis using TCAD simulation. Furthermore, from the experiments on hydrogen diffusion behavior at high temperature and long time, the bonding state of hydrogen was examined by kinetic analysis. Finally, in order to confirm the effect of reducing the SiO_2/Si interface state density, a MOS device was fabricated and the hydrogen termination effect on the interface state was studied using C-V measurement and electron spin resonance.

Chapter 2

Analysis methodology

2.1 Experimental procedure

In this study, I first evaluated the crystal defects formed by molecular ion implantation. In addition, the defect morphology after implantation and epitaxial growth were evaluated by Transmission Electron Microscopy (TEM). Further, it was clarified that the crystal defects formed by molecular ion implantation was larger than that of monomer carbon implantation. Then, the hydrogen concentration in the implanted region of hydrocarbon molecular ions after the annealing was analyzed by Secondary Ion Mass Spectrometry (SIMS) in order to clarify the hydrogen storage effect in the implanted region of hydrocarbon molecular ions. Then, the annealing time dependency of the hydrogen concentration in the implanted region of hydrocarbon molecular ions after the annealing was evaluated by SIMS. The dissociation activation energy from the implanted region of hydrocarbon molecular ions was calculated by using the reaction kinetics. Furthermore, a reaction model of the hydrogen dissociation reaction was assumed by the activation energy obtained from the experiment. In addition, I use TCAD in order to analyze the reaction model of the hydrogen diffusion behavior in the implanted region of hydrocarbon molecular ions. Finally, in order to clarify the reduction of the interface state due to molecular ion implanted wafers, the SiO_2/Si interface state was evaluated using Capacitance Voltage (CV) and Electron Spin Resonance (ESR) measurement. Figure 2.1 shows Analysis flow and schematic diagram. Details on the above SIMS, TEM, TCAD, CV, ESR analysis methods are described in the next section.

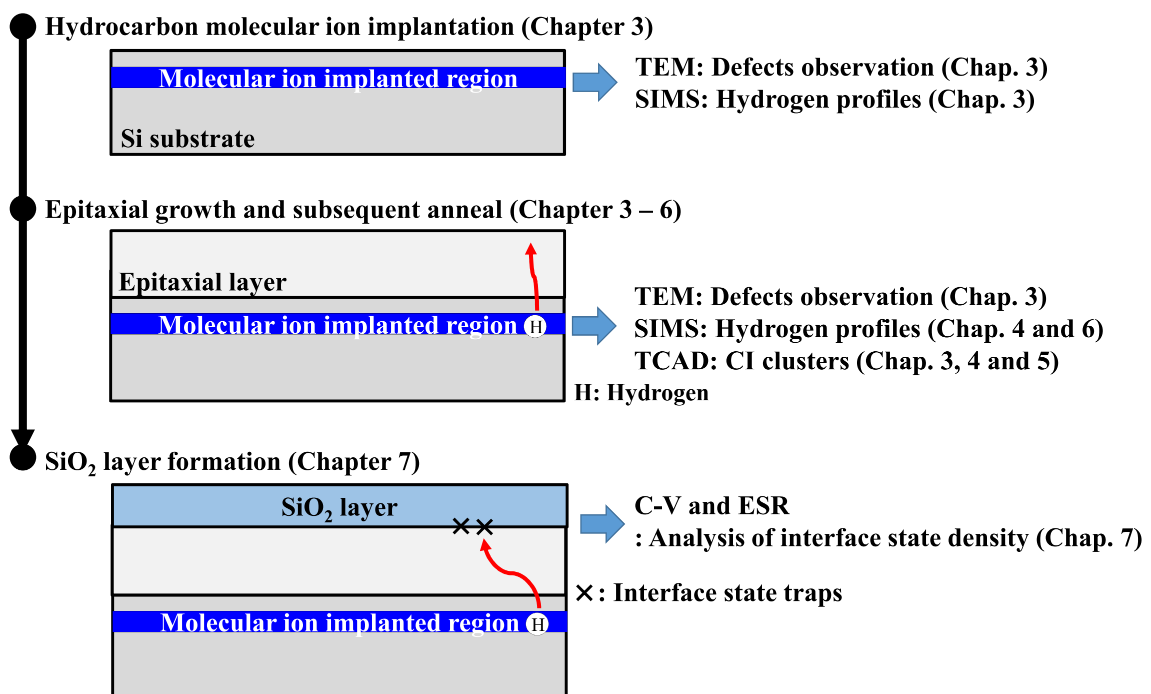

Figure 2.1: Schematic diagram of analysis flow.

2.2 Analysis methods

2.2.1 Secondary ion mass spectrometry (SIMS)

In this study, I used the distributions of the hydrocarbon molecular ions implanted carbon, hydrogen and monomer-ion-implanted carbon were analyzed using secondary ion mass spectrometry (SIMS; CAMECA IMS7f). SIMS as material characteristics technique is based on the information brought by the atomic or molecular secondary ions ejected from any surface under a primary ion bombardment [45]. SIMS analysis use primary ions such as O^- or C_s^+ [46, 47]. Primary ions are generated using an ionization system such as a surface ionization ion source. Primary ions are purified in a separator and focused by a condenser and objective lens. The sample is irradiated with the primary ion beam. Figure 2.2 shows a schematic diagram of secondary ion generation in SIMS analysis. The sample is sputtered by the primary ion beam bombardment and secondary ions are emitted from the sample surface. Intensity of the secondary ion signals depends on the concentration and ionization efficiency of the target element or molecule. If the ionization efficiency is constant, the depth profile of hydrogen concentration is measured by the sputtering rate of the silicon wafer using the primary ion and the intensity of secondary ion signals. The ionization efficiency of secondary ions is depended on the primary ions [46, 47]. Therefore, the primary ion needs to be selected according to the kind of atom analyzed. In general, C_s^+ is used for the analysis of atoms that easily form negative ions, and O^- are used for the analysis of metals that easily form positive ions. This type of SIMS analysis method is called dynamic SIMS analysis. There are two types of mass spectrometry (MS) methods for dynamic SIMS: magnetic and quadruple. Magnetic MS uses a mass separation method utilizing an electric and magnetic field. The accelerated ions are separated by the difference in the orbit radius depending on the strength of the magnetic and electric field on m/z where m is the mass of the ionized atom, and z is the charge of the ion. The magnetic MS measures with high resolution and high sensitivity. On the other hand, quadruple MS (QMS) uses four cylindrical electrodes. A high-frequency electric field is formed by applying a DC voltage and an AC voltage to each pair of QMS electrodes. Mass separation is performed by the difference in the m/z that can pass through this high-frequency electric field. QMS has the advantage of analysis capability near the surface of samples and high depth resolution. However, this method has the disadvantage of low mass resolution. For example, QMS cannot separate between $^{28}Si^{2+}$ and $^{14}N^+$ [46]. In this study, I used QMS for the analysis of the concentration depth profile after ion implantation because of the high resolution near the surface region. Magnetic MS was used for mass analysis to analyze the depth profile of

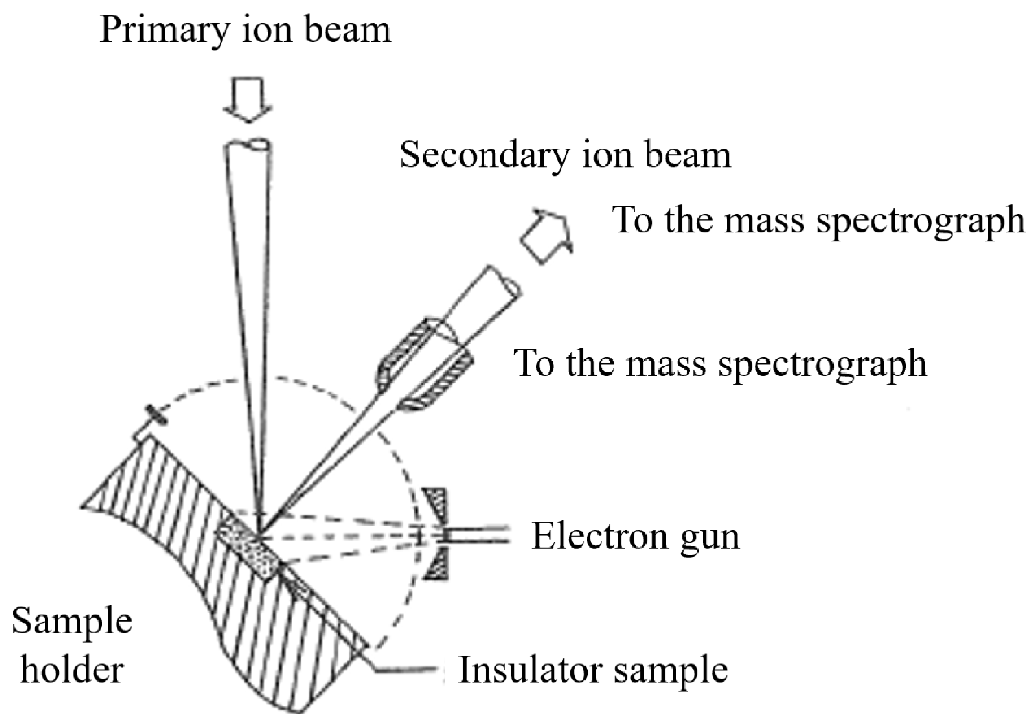

Figure 2.2: Schematic diagram of secondary ion generation in SIMS instrument.

carbon and hydrogen after epitaxial growth.

2.2.2 Transmission electron microscopy (TEM)

I used High resolution TEM (HRTEM) and nano electron diffraction (nano-ED) pattern to observe implantation defects in the projection region of hydrocarbon molecular ions [48, 49]. Figure 2.3 shows the schematic diagram of the TEM instrument. TEM observes crystal defects in nano scale regions. The TEM instrument consists of an electron source, a condenser lens, an objective lens, an intermediate lens, a projector lens, and the screen. Electrons emitted from the hot filament are converged by the condenser lens and form the electron beam. Then, the electron beam is irradiated onto the sample. The electrons transmitted through the sample are scattered due to the interaction with the sample. The contrast resulting from this scattering phenomenon is called scattering contrast. In areas where scattering is strong, transmitted electrons decrease and appear darker, which makes it possible to distinguish them from the surroundings. Also, some of the scattered electrons are observed as a diffraction pattern determined by the crystal structure. Information about the crystal structure, such as the regularity of the atomic arrangement, periodicity, symmetry, and disorder from the integrity of the crystal lattice can be obtained. If the sample is amorphous, the distance and number of neighboring atoms can be known. Since electron beams can be narrower than X-rays, diffraction patterns can be obtained from nano scale areas [49]. In this study, the defect morphology in the implanted region of hydrocarbon molecular ion after ion implantation and epitaxial growth was observed by HRTEM. In addition, the defect structure was analyzed by nano-ED.

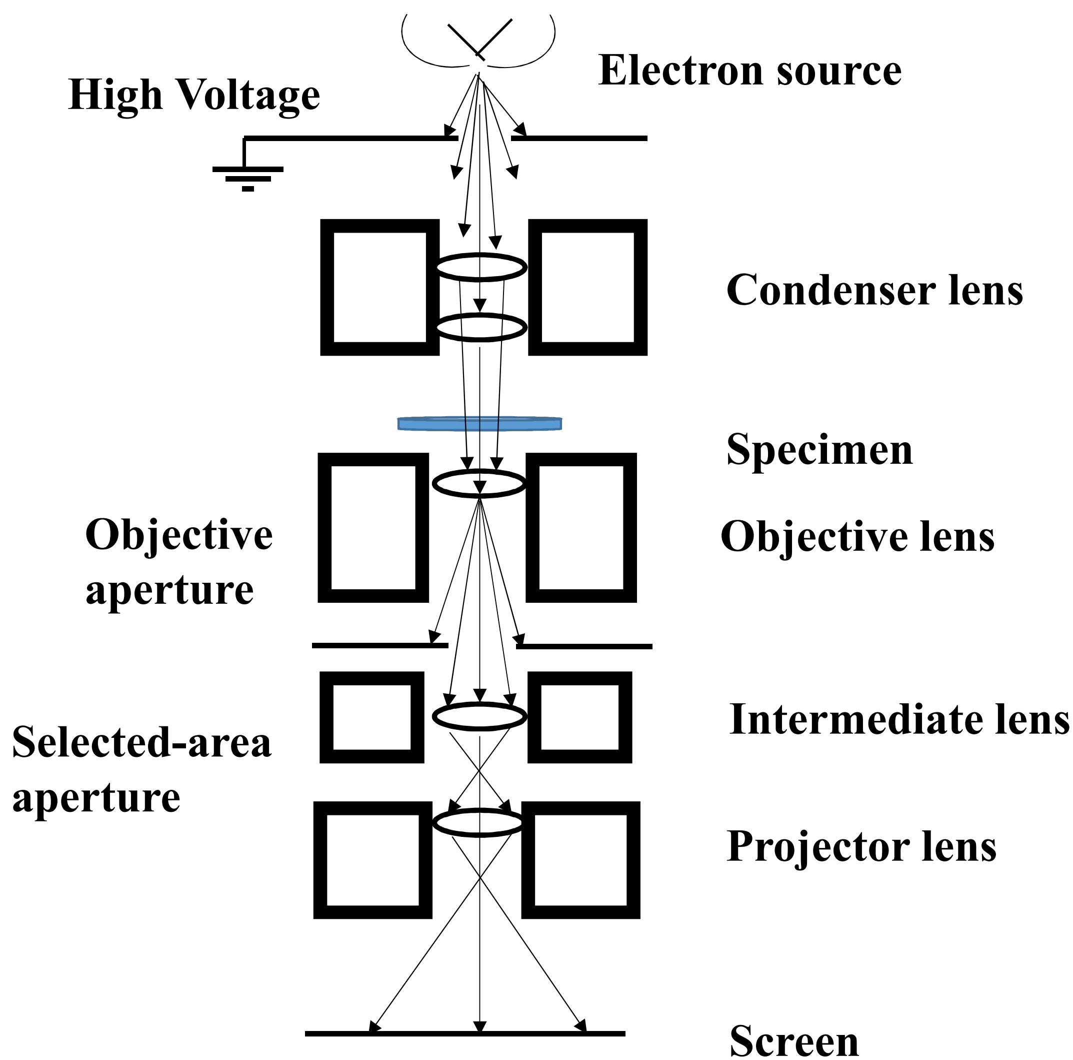

Figure 2.3: Schematic diagram of TEM.

2.2.3 Technology computer aided design (TCAD)

Technology Computer Aided design (TCAD) is a branch of electronic design automation that models semiconductor fabrication and semiconductor device operation [50]. TCAD is a combination of process simulator, device simulator and circuit simulator. The modeling of the fabrication is termed process simulator, while the modeling of the device operation is termed Device simulator. Process steps (such as diffusion and ion implantation) and device doping profiles are modeled based on basic physics. This is a technology that simulates a semiconductor process that normally takes 10 days to several months on a computer, and optimizes the structure of a semiconductor device showing desired conditions and the conditions for producing the same. In this study, I have used the TCAD Sentaurus process from Synopsys Inc. [51]. Sentaurus process simulates all standard process simulation steps, diffusion, analytic implantation, Monte Carlo implantation, oxidation, etching, deposition, and silicidation. In addition, Sentaurus process uses the Alagator scripting language that allows users to solve their own diffusion equations [51]. Alagator can be used to solve any diffusion equation including dopant, defect, impurity, and oxidant diffusion equations. I used this Alagator script to model the hydrogen adsorption and desorption behavior of a hydrocarbon molecular ion implanted region. In particular, the complexes of carbon and silicon interstitial (CI cluster) can be formed in the implanted region of hydrocarbon molecular ions [53].

Carbon is present in silicon as a substitutionally dissolved isovalent impurity, introduced during crystal growth and occupies substitutional sites (C_s). It appears in high concentrations, ranging from 10^{15} to 10^{18} cm^{-3}, well above its solubility at the usual annealing temperatures. However, it is established that most of the silicon interstitial (I) are readily trapped by C_s, which are pushed to interstitial sites according to the displacement reaction $C_s + I \rightarrow C_i$. In addition, I is generated by hydrocarbon molecular ion implantation. The substitutional carbon cannot directly trap self-interstitials, but self-interstitials trapped by carbon generate highly mobile carbon interstitials. The immobilizing reaction could then be the following:

$$C_i + C_s = (C_i C_s) \tag{2.1}$$

where C_s is a substitutional carbon atom, C_i a highly mobile interstitial carbon atom, and $(C_s C_i)$ an immobile carbon complex consisting of one C_s and one C_i atoms.

Figure 2.4 shows the structures of C_i and $C_i C_s$. Furthermore, these small clusters can grow by trapping either I or C_i that are rapidly diffusing across the material. The reactions that govern the growth/dissolution of these clusters are:

$$C_nI_m + C_i = C_{n+1}I_{m+1} \tag{2.2}$$

(trapping/emission of a C_i),

$$C_nI_m + I = C_nI_{m+1} \tag{2.3}$$

(trapping/emission of an I).

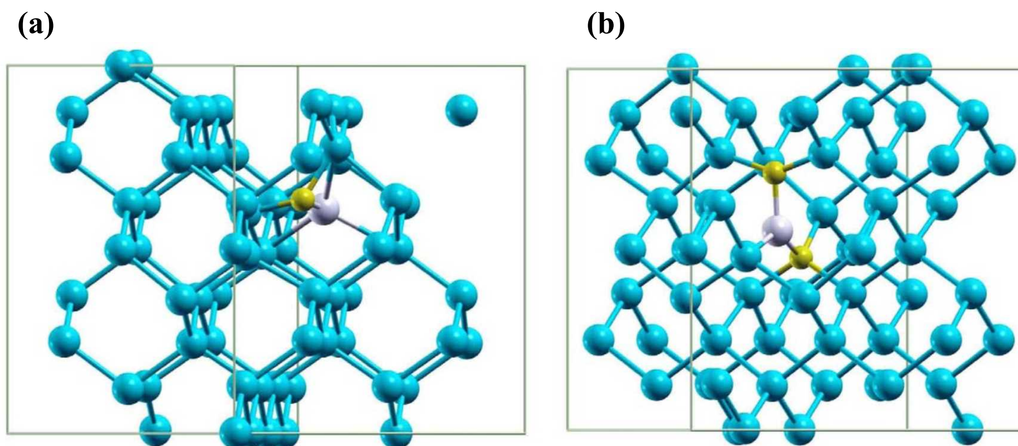

Figure 2.4: Structures of (a) C_i and (b) C_iC_s [53].

Table 2.1 shows three CI cluster complexes that can be calculated from Sentaurus process.

Table 2.1: CI cluster complexes for Sentaurus process simulator.

Symbol	Description
C	Carbon
CI	Carbon interstitial
C_2	Two-carbon cluster
C_2I	Two-carbon and silicon interstitial cluster
C_3I_2	Three-carbon and two-silicon interstitial cluster
C_3I_3	Three-carbon and Three-silicon interstitial cluster

Furthermore, Sentaurus process has Kinetic Monte Carlo (KMC) code. In the continuum diffusion model, this requires the use of one equation per each dopant-defect configuration, which leads to a multitude of equations to be solved. The trend of reducing device sizes results in a small number of impurity atoms that determine the threshold voltage of a transistor. It is likely that a limit soon will be reached where small discretized distribution can no longer be accurately modeled with a continuum description. A Monte Carlo (MC) based diffusion simulation provides a valuable alternative to the continuum approach. Computational resources required for MC diffusion simulation are decreasing with device dimension because they are proportional to the number of dopants and defects in the device. On the other hand, resources for continuum simulations increase as modeling of ever more complex non-equilibrium phenomena are required. This trend has already gone a long way towards making the KMC diffusion method competitive with the most detailed continuum diffusion methods today in terms of the required computational resources. Unlike the continuum approach, the large number of different dopant-defect configurations does not present a problem for the MC approach, which simply needs to introduce the probabilities for the additional reactions. These probabilities are calculated based on the binding energies that can be plugged in directly from experiments, molecular dynamics, or ab initio calculations. Sentaurus process Kinetic Monte Carlo (Sentaurus process KMC) considers only defects and impurities, and ignores the lattice. This drastically reduces memory requirements compared to molecular dynamics or lattice KMC techniques and allows you to investigate simulation domains that are large enough to contain deep-submicron devices [52]. As Sentaurus process KMC tracks the diffusion and interaction of defects, the fastest process is the jumping of a point defect with a period of approximately 10^{-9} sec. When there are no mobile point defects in the structure, the time step is increased automatically to an emission of mobile particles from the surface or from an extended defect, which has a period of approximately 10^{-3} sec. In this thesis, I simulated the complex formed by carbon and interstitial silicon in the implanted region of hydrocarbon molecule ions using Sentaurus process KMC [52]. Table 2.2 shows the carbon complexes calculated by Sentaurus process KMC.

Table 2.2: Carbon cluster complexes calculated by Sentaurus process KMC.

Symbol	Description
C	Carbon, substitutional, at interfaces
CV	Neutral-paired defect of carbon and a vacancy
Ci	Neutral-paired defect of carbon and an interstitial
$CTotal$	Total carbon ($C + CV + Ci$)

2.2.4 Quasi-static capacitance voltage (CV) measurement

The low frequency Capacitance-voltage measurement maintains thermal equilibrium at all times. This capacitance is the ratio of the change in charge to the change in gate voltage, measured while the capacitor is in equilibrium. C-V measurements are generally made using an Alternating Current (AC) measurement technique. However, some capacitance measurement applications require a Direct Current (DC) measurement technique [54]. These are called quasi static C-V (or QSCV) measurements because they are performed at a very low test frequency, that is, almost DC [55]. These measurements usually involve stepping a DC voltage and measuring the resulting current or charge. Some of the techniques used for quasi-static C-V measurements include the feedback charge method and the linear ramp method [55]. A typical measurement is performed with an electrometer, which measures the charge added per unit time as one slowly varies the applied gate voltage. The quasi-static method is a common interface trapped charge measurement method. It provides information only on the interface trapped charge density, but not on their capture cross-sections. The basic theory of the quasi-static method was developed by Berglund [54]. The method compares a low-frequency (lf) C-V curve with one free of interface traps. The latter can be a theoretical curve, but is usually a high-frequency (hf) C-V curve determined at a frequency where interface traps are assumed not to respond. “Low frequency” means that interface traps and minority carrier inversion charges must be able to respond to the measurement ac probe frequency. The interface trap response has similar limitations. Fortunately, the limitations are usually less severe than for minority carrier response and frequencies low enough for inversion layer response are generally low enough for interface trap response. Figure 2.5 shows the equivalent circuit of the MOS structure for low-frequency C-V measurement and high-frequency C-V measurement. C_{ox} is the gate oxide film capacitance, C_{it} is the interface state capacitance, and C_s is the capacitance of the silicon substrate, which is the sum of the depletion layer capacitance and the inversion layer capacitance. From this equivalent circuit, the minimum capacitance C_{lf} of the MOS capacitor when measuring low-frequency CV is expressed by the following equation.

$$C_{lf} = \frac{1}{\frac{1}{C_{ox}} + \frac{1}{(C_s+C_{it})}}, \tag{2.4}$$

C_S is the semiconductor capacitance, C_{it} is related to the interface trap density D_{it} by $D_{it} = C_{it}/q$.

$$D_{it} = \frac{1}{q}(\frac{C_{ox}C_{lf}}{C_{ox} - C_{lf}} - C_s). \tag{2.5}$$

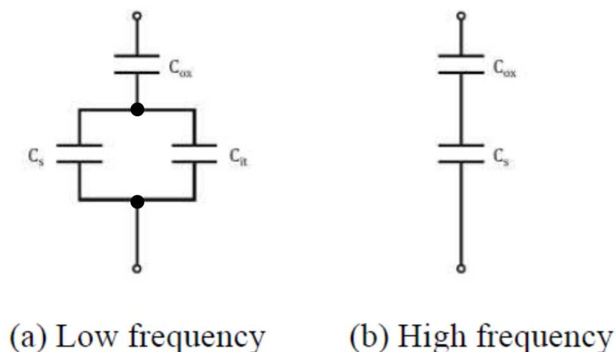

Figure 2.5: Schematic diagram of (a) low and (b) high frequency CV measurement.

Equation 2.5 is suitable for interface trap density determination over the entire band gap. $C_{ox}C_{lf}/(C_{ox} - C_{lf})$ in Equation. 2.5 is the substrate capacity obtained by measurement. The substrate capacitance C_s of the ideal MOS structure can be obtained from theoretical calculation or from high frequency CV measurement. In this paper, C_s was calculated using theoretical calculation.

2.2.5 Electron spin resonance (ESR)

Electron Spin Resonance (ESR) is a powerful analytical method to detect, analyze and determine the characteristics of unpaired electrons in a material [56–59]. It is clear that the state of electrons in a substance have a strong influence on its characteristics and functionality. Thus, ESR analysis is extremely important. Many types of material, from electronic materials to catalysts, biological samples, can be studied regardless of whether they are solid, liquid, or gas. A wide range of ESR techniques are possible using suitable attachments together with the basic instrument. Generally, stable molecules have the property that two electrons enter orbit as a pair. On the other hand, lattice defects in solids and transition metals with a specific valence are known to have unpaired electrons. Materials with unpaired electrons are called paramagnetic, and those without them are called diamagnetic. Most natural materials (water, alcohol, etc.) are diamagnetic. Electrons are known to have magnet-like properties (spin). One molecular orbital (s, p, d, f, etc.) stores up to two electrons. However, at this time, the electron spins are arranged in opposite directions (Pauli's principle). As a result, the paired electrons cancel each other's magnetic field and the properties of the magnet disappear (diamagnetic). On the other hand, in a paramagnetic material having unpaired electrons, one electron enters the orbit without forming a pair, and the magnetism inherent to the electron remains. ESR observes the magnetism caused by this electron. Electron spins point in random directions when no magnetic field is present. However, when they are placed in a magnetic field, they are oriented parallel (β spin) or antiparallel (α spin) to the magnetic field. α spin and β spin have equal energy at zero magnetic field. In the presence of a magnetic field, the α spin destabilizes while the β spin stabilizes. As shown in Figure 2.6, this is called the Zeeman effect. The energy difference between the two directions increases in proportion to the magnetic field strength. When the energy difference $\varDelta E$) matches the microwave energy, the electron spin absorbs the microwave and transitions to the upper level. This is observed as an ESR signal. The resonance condition at this time is given by the following equation 2.6;

$$\varDelta E = h\nu = g\mu B. \tag{2.6}$$

The μ is the Bohr magnetron (basic unit indicating the size of an electron as a magnet: $9.274078 \times 10^{-24} JT^{-1}$), and The h is the Planck constant ($6.626176 \times 10^{-34} Js$), which is a natural constant. The ν is the resonance frequency (Hz) and B is the strength of the magnetic field (mT), both of which are experimental values. The g value is a material-specific value determined by the environment of the electron spin. Once ν and B are determined experimentally, the g value can be determined.

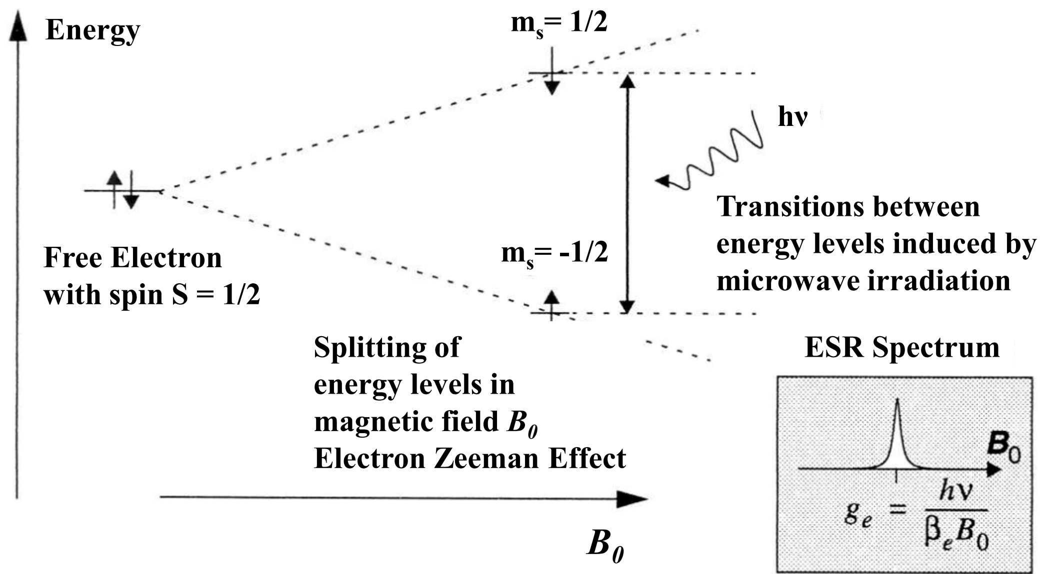

Figure 2.6: Schematic diagram of the Zeeman effect.

In this study, dangling bonds existing at the SiO_2/Si interface were evaluated by ESR to compare with D_{it} calculated from CV measurement. As an analysis method using the ESR of the SiO_2/Si interface, first, the ESR measurement of the SiO_2/Si sample was performed [56,57]. Thereafter, SiO_2 was removed with hydrofluoric acid, and an ESR spectrum was obtained again. Defects caused by dangling bonds at the SiO_2/Si interface were analyzed from the difference spectra of ESR before and after SiO_2 removal. Figure 2.7 shows the schematic diagram of ESR analysis in this study.

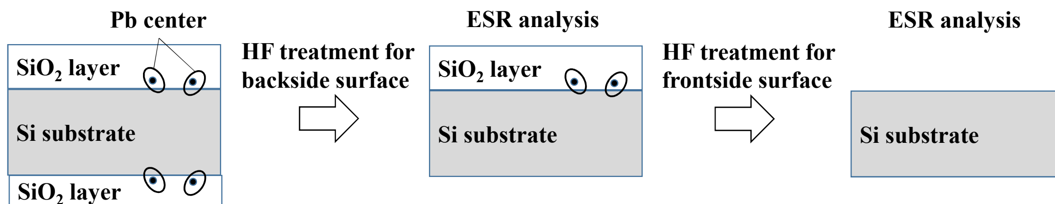

Figure 2.7: Schematic diagram of ESR analysis in this study.

Chapter 3

CI-cluster formation in hydrocarbon-molecular-ion implanted region

3.1 Introduction

As shown in above chapters, CMOS image sensor manufactures strongly require reduction in dark current and white-spot defects for high sensitivity performance [24]. The dark current and white-spot defects are caused by deep energy levels in the silicon band gap formed by metallic impurities contamination in the space-charge region during the device fabrication processs [26, 66–69]. Therefore, an important requirement is that metallic impurity is eliminated from the device-active region. Gettering techniques, such as intrinsic gettering (IG) and extrinsic gettering (EG), are necessary to address these issues [21, 22, 70–73]. However, device annealing process is tending toward short times and low temperatures [74]. Thus, metallic impurity contamination is difficult to diffuse to the gettering sink in the silicon bulk. Furthermore, it is difficult for IG sinks to grow oxygen-precipitate in the silicon bulk during the low-temperature-device annealing processes. Therefore, a proximity gettering technique is needed for CMOS image sensors. This technique forms the highest gettering capability sink under the epitaxial layer and substrate interface.

I previously developed a proximity gettering technique by using hydrocarbon-molecular-ion-implanted silicon wafers [30, 32, 36]. Hydrocarbon-molecular-ions can be obtained by the decomposition of the source gas containing carbon and hydrogen. For example, I can use C_5H_5 and C_3H_5. The implantation energy is very low because molecular ions distribute implantation energy [75]. I can use very low energy implantation and form the implanted region near

the top silicon wafer surface. Furthermore, previous studies demonstrated that hydrocarbon-molecular-ion implanted epitaxial wafers have three characteristics for obtaining high-performance advanced CMOS image sensors [30, 32, 36]. First, the implanted region has a high gettering capability for metallic impurities [30, 32, 36]. Second, this implanted region also has a barrier effect on oxygen impurities out-diffusing from the Si wafer bulk [30, 32]. Third, a passivation effect on SiO_2/Si interface state is expected owing to the hydrogen in the hydrocarbon-molecular-ions trapped in the implanted region during the device process [36]. However, the formation behavior of the implantation defect considered to be the gettering sink in the hydrocarbon-molecular-ion implanted region is not clear. Previous studies have reported using a monomer ion implantation technique for gettering [27, 76–82]. However, monomer-ion implantation usually requires high energy beyond 100 keV, and the implanted region of a monomer ion is deep in the silicon substrate surface. Even if a monomer ion can be implanted with low energy, it is difficult to control the implanted region because of the channeling effect. In addition, the previous gettering techniques by monomer ion implantation have mostly revealed that implantation defects such as dislocation loops are the gettering sink because high energy implantation occeurred [83–85]. However, it is not preferable for defects such as dislocation loops to be formed under the interface of the epitaxial layer and substrate for proximity gettering.

Therefore, the main intention of this section was to demonstrate the structure of hydrocarbon-molecular-ion implantation defects in silicon bulk. Several studies on hydrocarbon-molecular-ion implantation have been [83–86]. However, there have been few reporting the effects on defect formation of hydrocarbon molecular size and dose amount and on the comparison with monomer implantation. Furthermore, it is not clear what kind of defect is formed after epitaxial growth. Therefore, understanding the properties of hydrocarbon-molecular-ion implantation defects is important to both applied and fundamental material science. In this section, I compared the defect morphology after hydrocarbon-molecular-ion implantation and carbon-monomer implantation. I also investigated the dependence of hydrocarbon-molecular-ion size and dose amount on defect formation. I observed the hydrocarbon-molecular-ion implanted region after epitaxial growth by high-resolution cross sectional TEM.

3.2 Experiments

After a standard RCA cleaning process, 12 inch n-type Si (100) wafers were implanted with C_3H_5 and C_2H_5 hydrocarbon-molecular-ions at room temperature.

The condition of the tilt was 0°, and all the other experiments were performed under the tilt 0°. The C_3H_5 dose amounts converted into carbon were 1.0×10^{15}, 2.0×10^{15}, and 3.0×10^{15} carbon atoms/cm^2. The wafers were implanted with C_2H_5 of 2.0×10^{15} carbon atoms/cm^2 for comparison. The implantation energy was 80 keV/molecular ion. For a carbon atom, C_3H_5 was 23.4 keV and C_2H_5 was 33.1 keV. The C_3H_5 beam current was 800 μA (this means a factor of 3 to achieve an equivalent current per atom, i.e., 2400 μA/carbon atom) and the C_2H_5 beam current was 400 μA. Samples were prepared after implantation and after epitaxial silicon growth. The epitaxial silicon layers of 8.0 μm thickness were grown using a Si_3HCl gas source at 1100°C. The epitaxial growth rate was 1.0 μm/min. The monomer-carbon-implantation samples were also prepared with the same carbon dose amount and energy as the C_3H_5-cluster-ion condition. Hydrocarbon-molecular-ion implantation and monomer-carbon ion-implantation were conducted in CLARIS and EXCEED of Nissin Ion Equipment, respectively.

Figure 3.1 shows the process and analysis flow diagram of this study. Cross-sectional TEM (XTEM) imaging was done to study the evolution of hydrocarbon-molecular-ion implantation and monomer-carbon-ion implantation damage. Selected-area electron diffraction (SAED) analysis was conducted after sample implantation to evaluate the amorphous layer. The distribution of the hydrocarbon-molecular-ions, implanted carbon, and monomer-ion-implanted carbon were analyzed using secondary ion mass spectrometry (SIMS). High-resolution XTEM (HR-XTEM) and nano-beam electron diffraction (n-ED) were used for observing the ion-implantation defects in the hydrocarbon-molecular-ion implanted region after epitaxial growth.

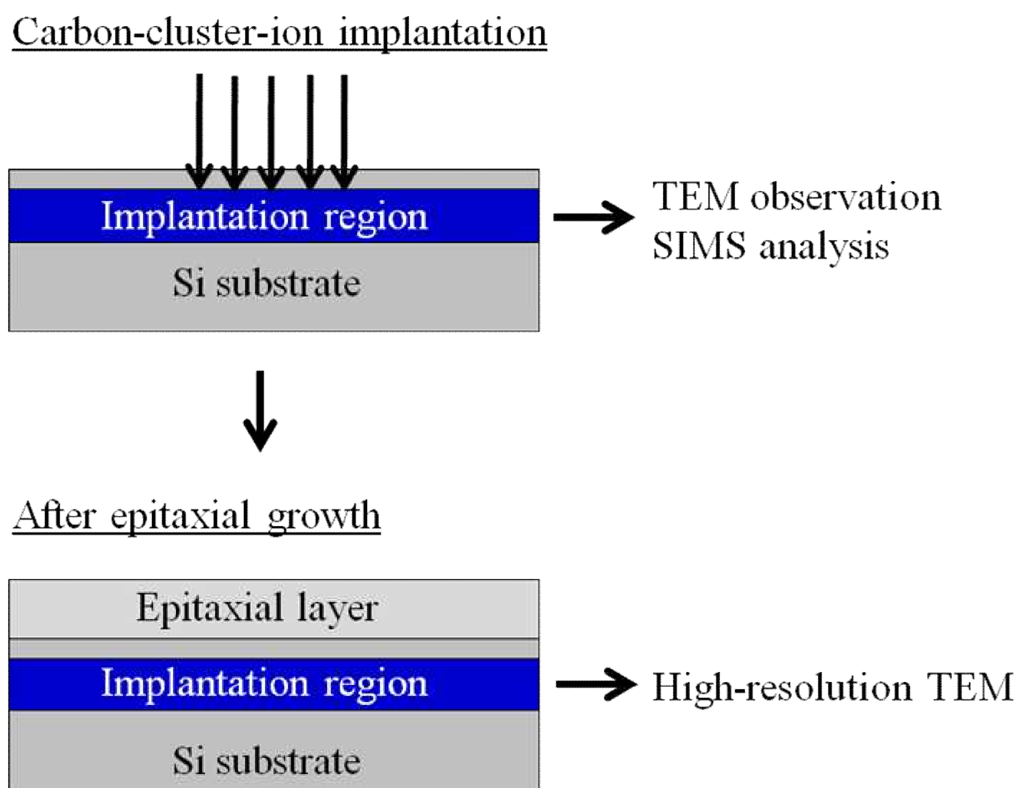

Figure 3.1: Process and analysis flow diagram of this study.

3.3 Defect formation behavior in the hydrocarbon-molecular-ion implanted region

Figures 3.2 (a), (b), and (c) show XTEM images of the C_3H_5-molecular-ion implanted samples with doses of (a) 1.0×10^{15} carbon atoms/cm^2, (b) 2.0×10^{15} carbon atoms/cm^2, and (c) 3.0×10^{15} carbon atoms/cm^2. The different contrast region at a depth of approximately 60 nm is the damage region, as shown in Figure 3.2 (a). The glue is on the silicon surface. As the dose amount increased, the damage region changed to an amorphous structure, as shown in Figures 3.2 (b) and (c). The amorphous region was confirmed by SAED. The amorphous region was not formed from the silicon surface, and it was observed in the silicon being formed inside. N. G. Rudawski *et al.* demonstrate that the formation of the amorphous region by the C_7H_7 molecular is caused by the silicon surface [86]. It was revealed that the formation process of amorphous regions varied in accordance with a difference in hydrocarbon-molecular-ion size. In addition, the top of silicon surface seems to be rough depending on the dose of hydrocarbon-molecular-ion implantation. This is considered to be because the amorphous layer is formed inside, so that the amorphous layer is also formed on the silicon surface, and the silicon surface roughness is increased.

Figure 3.3 shows the SIMS profile of the C_3H_5-molecular-implanted (solid line) and monomer-carbon-implanted (dashed line) samples for a dose amount 2.0×10^{15} carbon atoms/cm^2. The projected range of the C_3H_5-implantation carbon was approximately 80 nm. In spite of the same implanted energy of a carbon atom, the projected range of the monomer carbon was approximately 100 nm, as shown in Figure 3.3. As a result, the projected range of the C_3H_5-implantation carbon was shallower than that of the monomer carbon. In addition, the depth of the C_3H_5-implanted damage region differed by approximately 20 nm. The formation depth of the amorphous region was shallower than the projected range of the C_3H_5-implantation carbon.

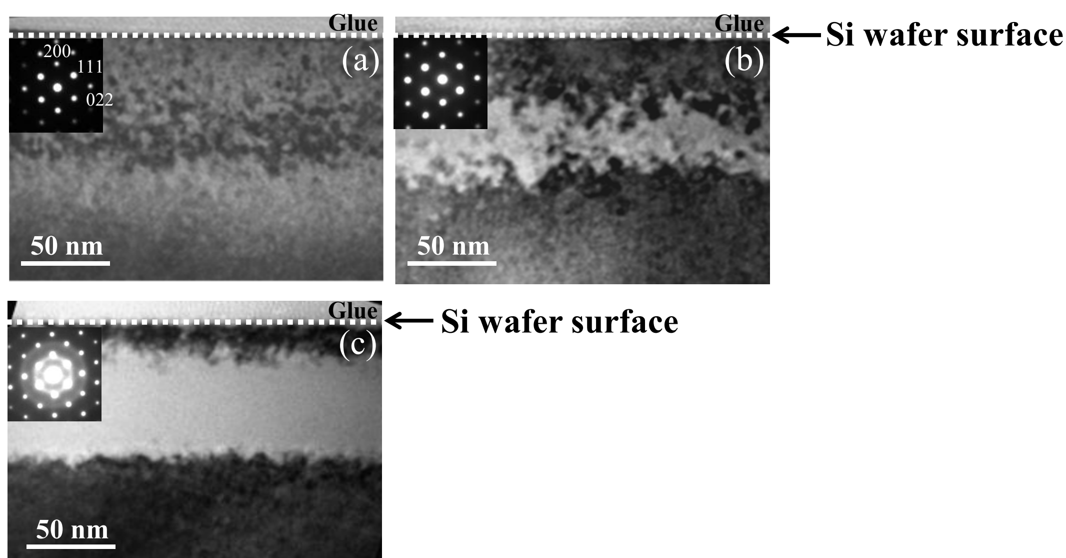

Figure 3.2: XTEM images of C_3H_5-cluster-ion-implanted Si wafers with carbon doses of (a) 1.0×10^{15}, (b) 2.0×10^{15}, and (c) 3.0×10^{15} carbon atoms/cm^2.

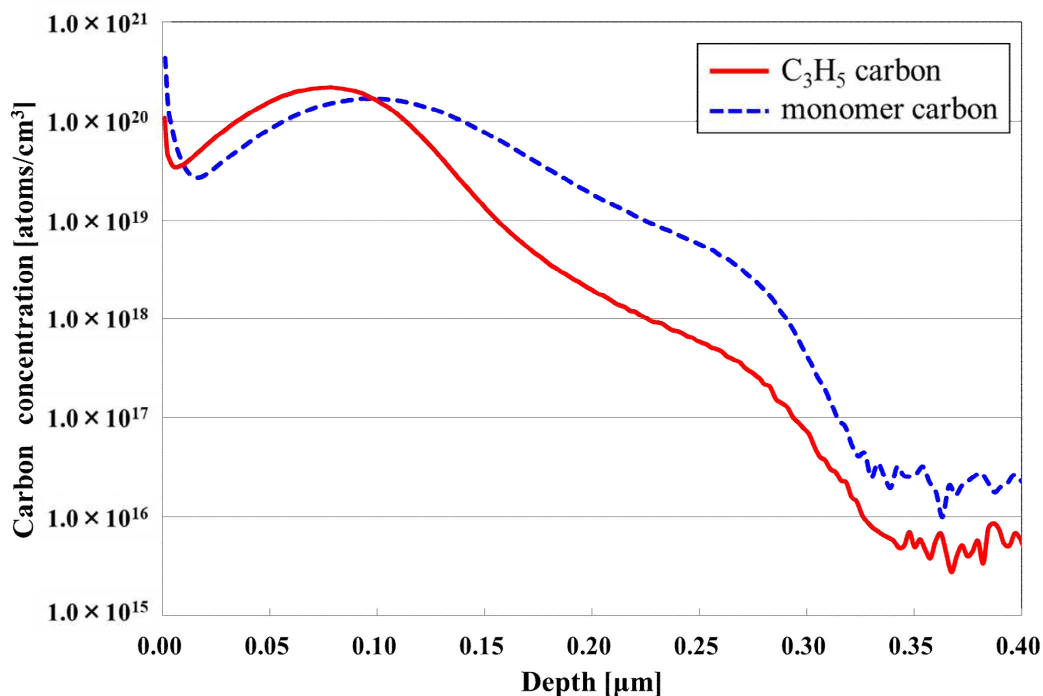

Figure 3.3: SIMS profile of C_3H_5-cluster-implanted and monomer-carbon-implanted samples for carbon dose of 2.0×10^{15} carbon atoms/cm^2.

Figures 3.4 (a), (b), and (c) show XTEM images of the carbon-monomer-implanted samples with doses of (a) 1.0×10^{15}, (b) 2.0×10^{15}, and (c) 3.0×10^{15} carbon atoms/cm^2. The amorphous region could not be observed regarding monomer implantation, even when the dose amount was 3.0×10^{15} carbon atoms/cm^2. The depth of the monomer-implanted damage region was approximately 80 nm. As show in the SIMS profile, the depth of the hydrocarbon-molecular-ion implantation damage region was also shallower than that of carbon monomers. These results indicate that a hydrocarbon-molecular-ion implantation has a de-channeling effect and that the damage of hydrocarbon-molecular-ion to the silicon wafer is larger than that of carbon-monomer ion. Furthermore, in previous studies, amorphization occurred from the silicon wafer surface [86]. However, in this study, the C_3H_5-cluster ions formed an amorphous region inside the silicon wafer. Amorphization occurred from the C_3H_5-molecular-implanted region. This result suggests that epitaxial growth is possible after a C_3H_5-molecular-implantation.

Figures 3.5 (a), (b), and (c) show XTEM images of the C_3H_5-molecular-ion implanted samples after epitaxial growth with doses of (a) 1.0×10^{15}, (b) 2.0×10^{15}, and (c) 3.0×10^{15} carbon atoms/cm^2, and Figure 5 (d) shows XTEM images of the C_2H_5-molecular-ion implanted samples after epitaxial growth with (d) 2.0×10^{15} carbon atoms/cm^2. As shown in Figure 3.5 (a), the hydrocarbon-molecular-ion implanted region was observed after epitaxial growth. Figures 3.5 (b) and (c) show a large defect on the implantation region with the increase in the dose amount. I call them black-point defects since they look like black points. The size of a large black-point defect is approximately 30 nm. This large defect was observed only when an amorphous region was observed before epitaxial growth. However, large black-point defects were not observed on the implantation region after epitaxial growth in Figure 3.5 (d). The amorphous region was not observed in the implanted region of the C_2H_5-molecular-ion implantation. These results clearly indicate that the damage of a hydrocarbon-molecular-ion depends on the size and dose amount. In addition, epitaxial defects, such as stacking faults, were not observed in the epitaxial layer.

Figures 3.6 (a) and (b) show high-magnification XTEM images of 1.0×10^{15} and 3.0×10^{15} carbon atoms/cm^2 samples after epitaxial growth, respectively. As shown in Figure 6 (a), a hydrocarbon-molecular-ion implantation defect due to aggregation of small-black point defects was observed at low magnification. On the one hand, this small black-point defect size was approximately 5 nm. On the other hand, the 3.0×10^{15} carbon atoms/cm^2 samples were observed to have small and large black-point defects. Depending on the dose amount, the density of the small black-point defects increased. For the 1.0×10^{15} and 3.0×10^{15} carbon atoms/cm^2 samples, the density of the small black-point defects was 6.3×10^{16} /cm^3 and 1.2×10^{17} /cm^3, respectively.

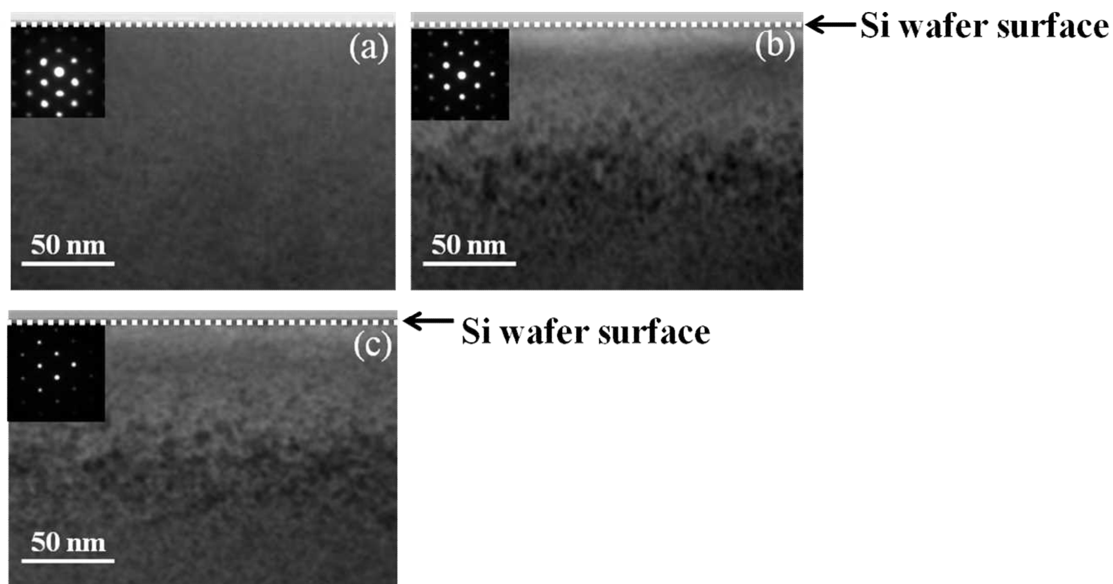

Figure 3.4: XTEM images of carbon-monomer-ion-implanted Si wafers with carbon doses of (a) 1.0×10^{15}, (b) 2.0×10^{15}, and (c) 3.0×10^{15} carbon atoms/cm^2.

Large black point defects formed in an approximately 40 nm region above the small black-point defects. This result suggests that the large black-point defects form the re-crystallization region of the amorphous region.

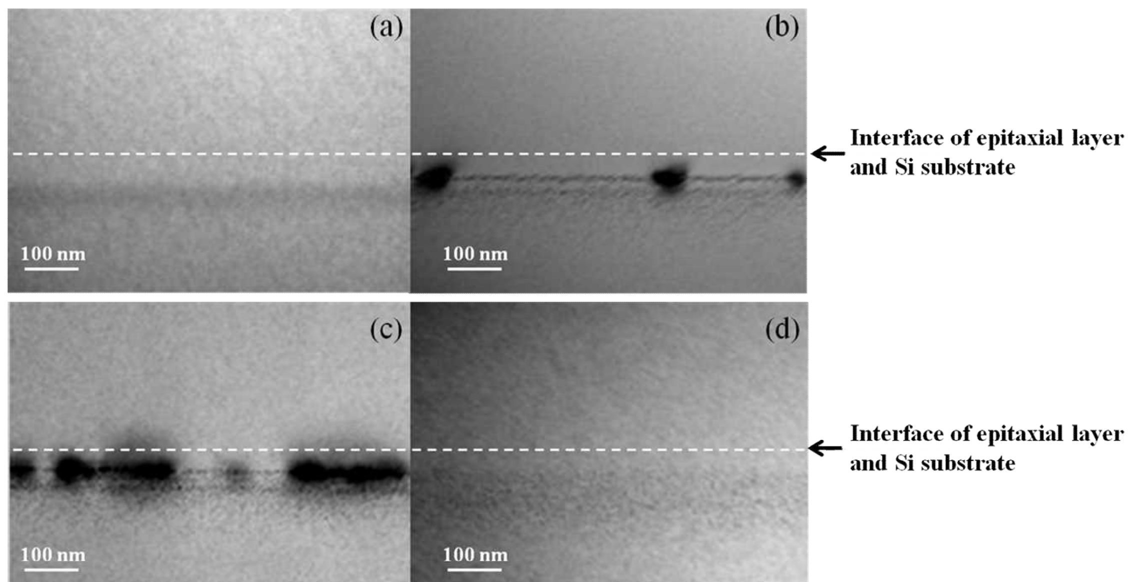

Figure 3.5: XTEM images of after epitaxial growth with carbon doses of (a) 1.0×10^{15}, (b) 2.0×10^{15}, and (c) 3.0×10^{15} carbon atoms/cm^2. (a) - (c) using C_3H_5 cluster size, (d) 2.0×10^{15} carbon atoms/cm^2 using C_2H_5 cluster size.

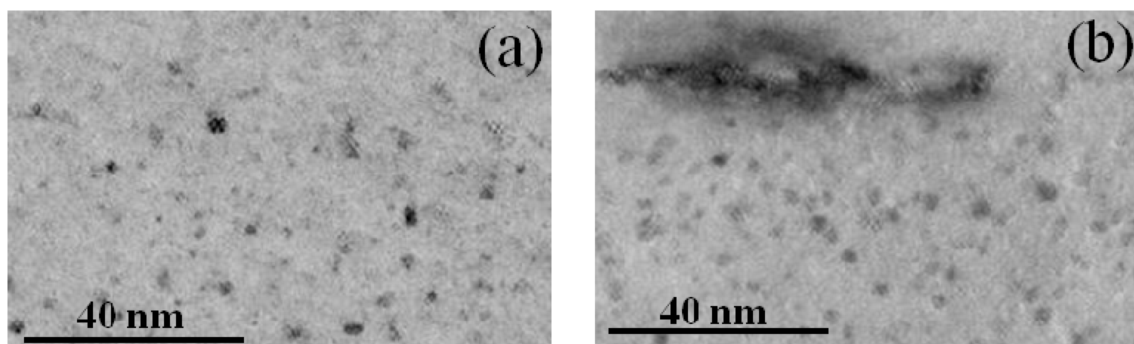

Figure 3.6: High-magnification XTEM images of carbon doses of (a) 1.0×10^{15} and (b) 3.0×10^{15} carbon atoms/cm^2 for after-epitaxial-growth samples.

3.4 Mechanism of defect formation behavior in the implanted region of the hydrocarbon molecular ion

I observed the hydrocarbon-molecular-ion implanted region on the basis of detailed analysis of small and large black-point defects by HR-XTEM and n-ED. Figure 3.7 shows the HR-XTEM and n-ED observation results. The lattice constant did not change by HR-XTEM. In addition, I found that small and large black-point defects were electron diffraction patterns of silicon single crystalline by n-ED. Other defects such as secondary extended dislocation defects or stacking faults were not observed. Small black-point defects were observed from the 1.0×10^{15} carbon atoms/cm^2 dose condition in which the amorphous layer is not formed. In contrast, large black-point defects were observed only on the dose condition in which the amorphous layer is formed. Consequently, I assume that small black-point defects are carbon related defects and the large black-point defects are the effects of an amorphous region. Similar small black-point defects were reported from observing the formation of silicon-carbide (SiC) structures as in previous studies on monomer-carbon implantation [70, 87]. Thus, SiC precipitates formed as a result of high-temperature annealing. In this study, annealing of 1100°C was carried out for several minutes on an after-epitaxial-growth sample. However, small black-point defects were observed as an electron diffraction pattern of a silicon single crystal. Additionally, the lattice constant of the small black-point defects did not change with those of the silicon substrate. Because the dose amount in this study was smaller than that of previous studies, I considered that a SiC structure did not form.

Consequently, I assume that small black-point defects are formed by a complex of carbon. Pinacho *et al.* reported that the behavior of carbon impurities in Si bulk demonstrates that carbon and Si self-interstitial (CI) clusters are formed in carbon-rich Si [61]. As shown in Figures 3.2, 3.3, and 3.4, implantation damage and the de-channeling effect of hydrocarbon-molecular-ion implantation are larger than those of monomer implantation. These results indicate that many vacancy and Si self-interstitial point defects may be generated after hydrocarbon-molecular-ion implantation. I consider that implanted carbon and Si self-interstitial generated by hydrocarbon-molecular-ion implantation can form a CI cluster of carbon and Si self-interstitial. I assume that these CI clusters were observed as a contrast of the HR-XTEM. Therefore, I simulated the hydrocarbon-molecular-ion implanted silicon epitaxial wafer fabrication process by using the kinetic monte carlo (KMC) code in technology computer aided design (TCAD) Sentaurus process from Synopsys Inc.

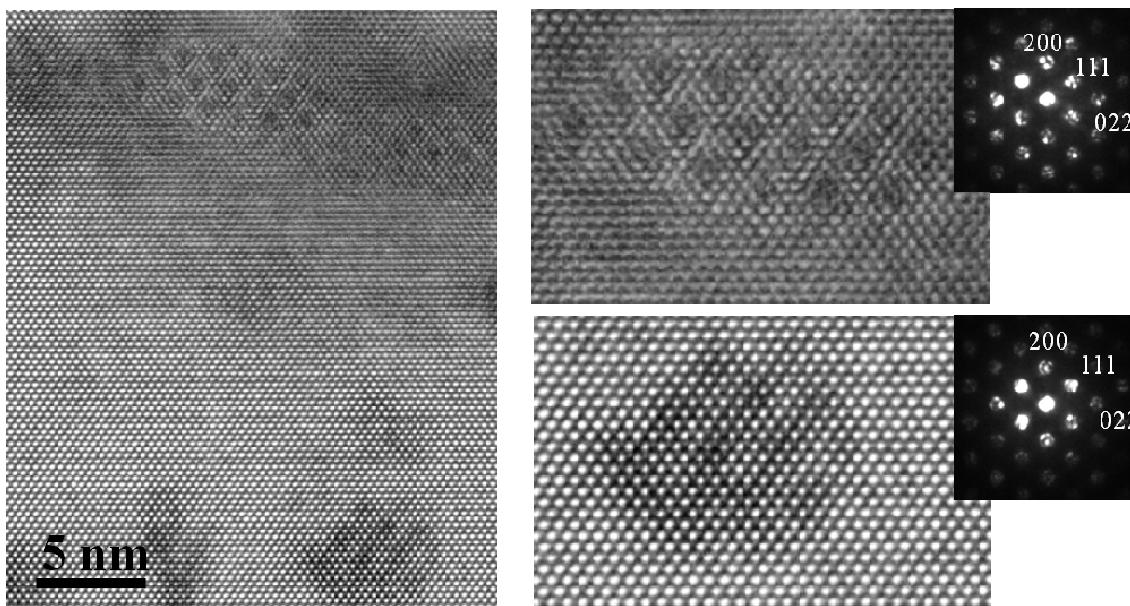

Figure 3.7: HR-XTEM image and electron diffraction pattern from n-ED observation with carbon dose of 3.0×10^{15} carbon atoms/cm^2 for after-epitaxial-growth sample.

owing to confirmation of the formation of a CI cluster [51]. Furthermore, the model for the formation of a CI cluster is incorporated in the TCAD Sentaurus process [51, 61]. Figure 3.8 shows the distribution for carbon (black) and Si self-interstitial (red) simulated by using KMC code of TCAD in the hydrocarbon-molecular-ion implanted region after epitaxial growth annealing. The formation of CI clusters was confirmed in the hydrocarbon-molecular-ion implanted region by TCAD simulation. Consequently, I suggest that small black-point defects are formed by the aggregation of CI clusters. In addition, the size of CI clusters was approximately 5 nm. Larger sizes are expected to increase strain stress on the crystal lattice. Therefore, it is considered that the critical size is approximately 5 nm so that the strain stress does not increase. It is also considered that the crystal structure was a silicon single crystal structure.

On the other hand, the presence of large black-point defects was confirmed only in the condition in which the amorphous region was observed. Moreover, large black-point defects formed in approximately the 40 nm region above the small black-point defects. This region is in agreement with the amorphous region. Therefore, I assume that large black-point defects are the re-crystallization of the amorphous region. These results suggest that small and large black-point defects contribute to gettering capability for the metallic impurities of the hydrocarbon-molecular-ion implanted silicon epitaxial wafer.

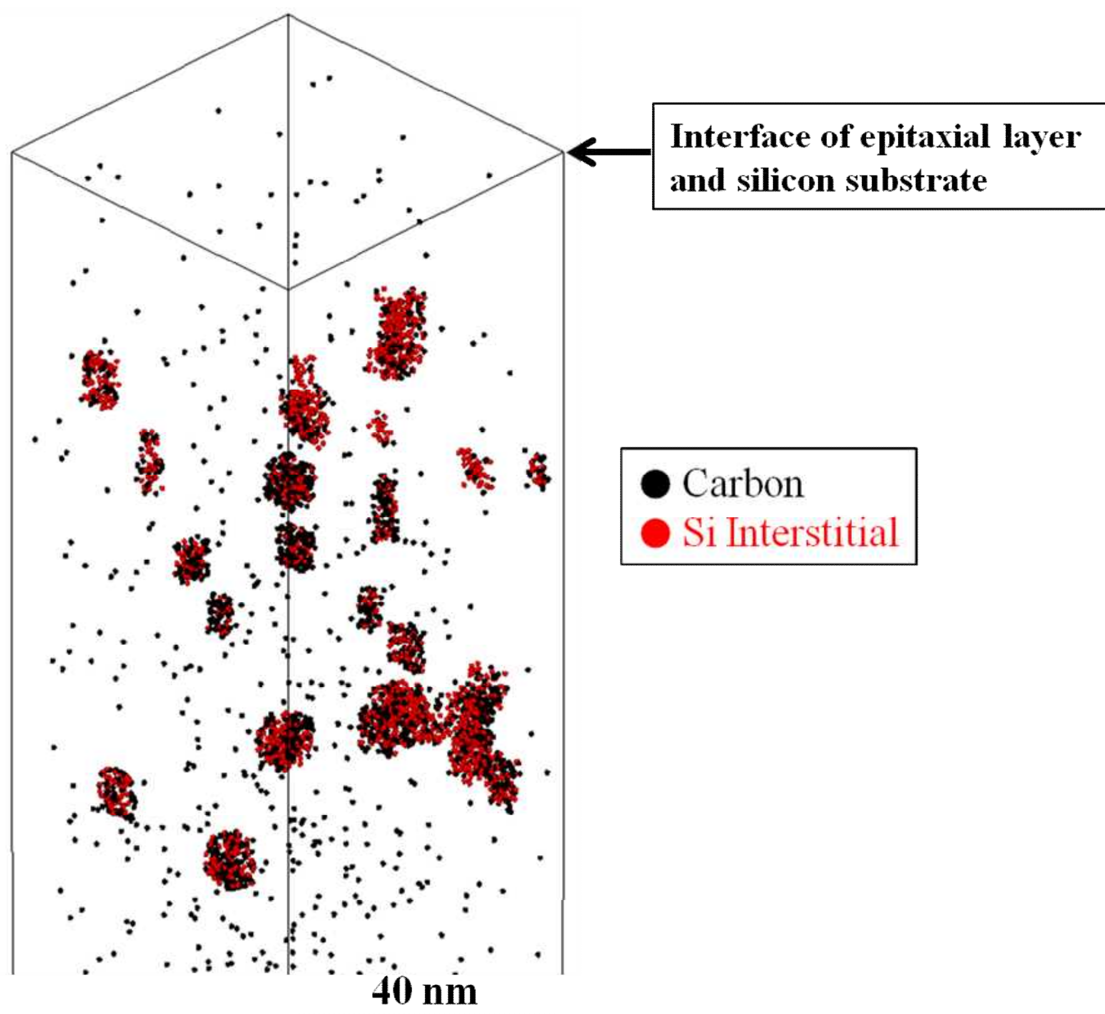

Figure 3.8: TCAD result by using KMC code of distribution for carbon (black) and Si self-interstitial (red) in implanted region of carbon cluster after epitaxial growth.

3.5 Summary

After hydrocarbon-molecular-ion implantation, I confirmed that hydrocarbon-molecular-ion implantation damage is larger than that of monomer implantation. This result means that hydrocarbon-molecular-ions exhibit de-channeling effects and cause damage depending on the hydrocarbon-molecular-ion size. I also analyzed samples after epitaxial growth, on which previous studies have not been reported. I observed that two types of defects are formed at the hydrocarbon-molecular-ion implantation region in silicon bulk. These defects are single-silicon electron-diffraction patterns. In addition, the structures of these defects do not form SiC structures. Therefore, I assume that these defects are CI cluster related and amorphous-related defects. Amorphous-related defects also formed under high dose conditions. I believe that these types of defects have powerful gettering capability for our proximity gettering technique.

Chapter 4

Diffusion behavior of hydrogen in small thermal budget

4.1 Introduction

Above section shows the defect morphology in the implanted region of hydrocarbon molecular ion. In this section, I have revealed the diffusion behavior of hydrogen in the implanted region of hydrocarbon molecular ion by SIMS and reaction kinetic analysis. In previous studies, it was found that a hydrocarbon-molecular-ion implanted epitaxial silicon wafer exhibited three characteristics suitable for obtaining high-performance advanced CMOS image sensors. First, the implanted region of a hydrocarbon-molecular-ion has a high gettering capability regarding metallic impurities [30,32,36]. Second, this implanted region also has a barrier effect on oxygen impurities diffusing out from the silicon wafer [30,32]. Third, a passivation effect on process-induced defects (PIDs) is expected owing to the hydrogen in the hydrocarbon-molecular-ion trapped in the implanted region diffusing during the device process [30, 36]. In particular, I indicated the first gettering capability and the second barrier effect of oxygen diffusion. The hydrocarbon-molecular-ion is ionized by hydrocarbon source gases by the electron impact method. Thus, the hydrocarbon-molecular-ion is contained in not only carbon but also hydrogen (*e.g.*, C_3H_5 and C_5H_5).

I also reported that hydrogen after hydrocarbon-molecular-ion implantation is trapped after epitaxial growth in the implanted region [36]. Such a hydrogen diffusion behavior after epitaxial growth has not been reported because the diffusion velocity of hydrogen in a silicon wafer is extremely high at high temperatures [88]. Furthermore, if hydrogen remains in the implanted region after epitaxial growth, I assume that hydrogen out-diffusing from the hydrocarbon-molecular-ion implanted region during the device fabrication process can passivate the interface

state density of the isolation region and PIDs. It was also reported that the vacancy (V) and hydrogen complex are related to the gettering capability of hydrocarbon-molecular-ion implantation [44]. Thus, it is expected that the hydrogen in the hydrocarbon-molecular-ion implanted region contributes to the gettering capability and passivation. However, the diffusion behavior of hydrogen trapped in the hydrocarbon-molecular-ion implanted region after annealing is unclear.

Conventionally, it is well known that hydrogen has various effects on semiconductor materials [89, 90]. Previous studies were focused on the annealing diffusion behavior of hydrogen in semiconductors from both experimental and theoretical viewpoints. For example, hydrogen terminates a dangling bond of silicon, reduces the SiO_2/Si interface state density, electrically inactivates the semiconductor donor and acceptor, {111} platelets, and metastable diatomic hydrogen complexes, stabilizes the hydrogen molecule in crystalline silicon, and passivates the deep-level defect of transition metals [91–106]. In other studies, the hydrogen high-dose implantation condition enhances the formation of hydrogen-induced platelet defects used in the smart-cut process through the use of bubbles filled with hydrogen molecules [107–110]. In particular, hydrogen atoms easily form complexes such as impurities and defects because the diffusion velocity of hydrogen in silicon bulk is extremely high [89, 90]. The formation of hydrogen complexes in silicon has been studied extensively since Pankov *et al.* observed the passivation of boron with hydrogen [95]. In p-type B-doped silicon, the hydrogen atom is located at the bond-centered (BC) site between silicon and boron and forms the H-B passivation center. On the other hand, in n-type P-doped silicon, hydrogen is more stable in the tetrahedral interstitial (T_d) site than in the BC site [89, 90, 111, 112]. It has been reported that the hydrogen atom is located at the antibonding (AB) site in the P-Si bond of the P-H complex [89, 90]. Concerning other hydrogen complex formations in the silicon bulk, Murakami *et al.* identified the state of three types of hydrogen molecules in the Si bulk [99]. In addition, Fukata and co-workers reported that hydrogen is trapped in a Si-H bond in {111} platelets in silicon during P implantation and hydrogen froming gas anneal (FGA) [100–103]. They also found that vacancy forms complexes via the dissociation behavior upon annealing in hydrocarbon-molecular-ion implanted silicon after hydrogen FGA [113–115]. In previous papers, for a high dose of hydrogen introduced into silicon, the analytical results of the binding state and diffusion behavior after annealing below 700°C have been reported.

Therefore, our main intention in this section was to demonstrate the diffusion behavior of hydrogen after small thermal budget annealing and the dissociation activation energy from the hydrocarbon-molecular-ion implanted region. I discussed the binding state of hydrogen in the hydrocarbon-molecular-ion implanted region by

calculating the dissociation activation energy. Understanding the properties of the hydrogen behavior in the hydrocarbon-molecular-ion implanted region is important to both applied and fundamental material science.

4.2 Experimental methods

In this section, n-type Si (100) wafers were implanted with C_3H_5 molecular ions at room temperature. The C_3H_5 molecular ion dose was 1.67×10^{14} - 3.33×10^{15} molecular ions/cm^2. The C_3H_5 dose converted into the amount of carbon was 5.00×10^{14} - 1.00×10^{16} atoms/cm^2 and that converted to the amount of hydrogen was 8.35×10^{14} - 1.67×10^{16} atoms/cm^2. The implantation energy was 80 keV/cluster. The implantation energy of hydrogen was extremely low at 1.95 keV because the molecular ion distributed the implantation energy. The C_3H_5 beam current was 800 μA. The epitaxial growth of the samples was conducted after hydrocarbon-molecular-ion implantation. The epitaxial layer thickness was 5.0 μm. Furthermore, the samples were annealed from 300 to 900°C for annealing times from 5 to 360 min to evaluate the diffusion behavior of the hydrogen in the hydrocarbon-molecular-ion implantation implanted region. Figure 4.1 shows the process and analysis flow in this section. The distribution of hydrogen in the hydrocarbon-molecular-ion implanted region was analyzed by secondary ion mass spectrometry (SIMS).

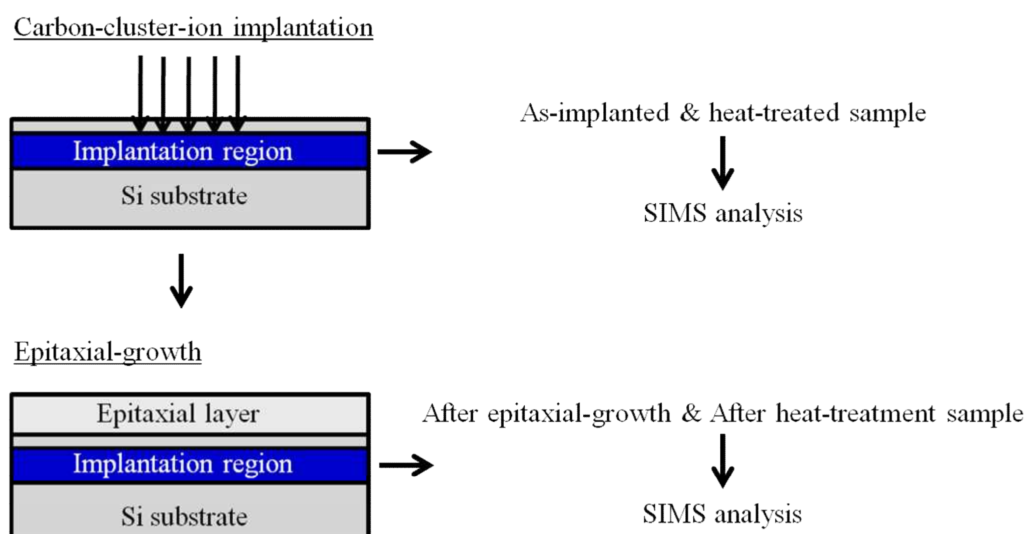

Figure 4.1: Process and analysis flow diagram of this study.

4.3 Hydrogen diffusion behavior in hydrocarbon-molecular-ion implanted region

The depth distributions of hydrogen and carbon obtained by SIMS analysis for the as-implanted (solid lines) and annealed (dashed lines) samples with a C_3H_5 dose of 3.3×10^{15} molecular ions/cm^2 are given in Figure 4.2. The hydrogen of the C_3H_5 formed a shallow implanted region near the top of the silicon wafer surface. For the implantation energy used in this study, hydrogen had 40 nm peaks from the silicon wafer surface. The decrease in hydrogen concentration owing to out-diffusion is considered to depend on the annealing condition. Although the diffusion velocity of hydrogen is markedly high in a silicon wafer, a hydrogen peak was observed in the hydrocarbon-molecular-ion implanted region after annealing at 900°C. The carbon profile was also observed in the hydrocarbon-molecular-ion implanted region after implantation and annealing.

Figure 4.3 shows the SIMS profiles of the as-implanted sample and after the 600°C annealing of a sample with monomer hydrogen implantation for comparison. The monomer hydrogen out-diffused to less than the detection limit of SIMS analysis upon annealing at 600°C. In monomer implantation, no hydrogen peak was observed in the implanted region after annealing. However, the hydrogen of the C_3H_5 was trapped in the implanted region. The hydrogen and carbon peaks after annealing were observed 60 nm from the silicon wafer surface. The hydrogen and carbon peaks of the annealed sample were different from those of the as-implanted sample. In addition, under the conditions of this study, the implanted region of the carbon peak was approximately 80 nm. I previously reported that the formation depth of an amorphous region was smaller than the implanted region of the carbon of implanted C_3H_5. These results indicate that the hydrogen peak after annealing is related to the amount of implantation damage. Therefore, I conducted a simulation of the amount of damage with respect to the hydrocarbon-molecular-ion implanted region by using the technology computer-aided design (TCAD) simulator Sentaurus process from Synopsys Inc. [52].

Figure 4.4 shows the damage (solid line), carbon (dotted line), and hydrogen (dashed line) profiles after C_3H_5 implantation. The peak of damage due to C_3H_5 implantation was approximately 60 nm. The concentration of damage by the TCAD simulation represents the concentration of vacancy formed by implantation. The depth of this peak of damage corresponds to the hydrogen peak after annealing. Therefore, I assumed that the damage region of the implanted region is the trapped hydrogen after annealing.

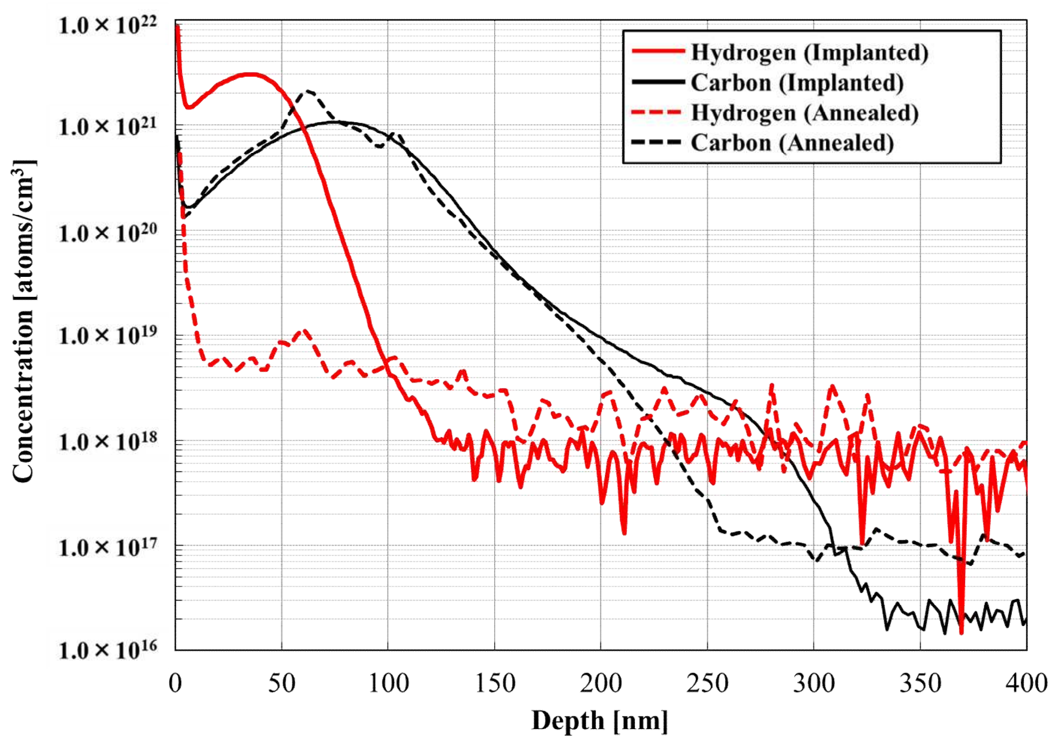

Figure 4.2: SIMS profile of hydrogen and carbon of as-implanted (solid lines) and annealed (dashed lines) samples with C_3H_5 dose of 3.3×10^{15} atoms/cm^2.

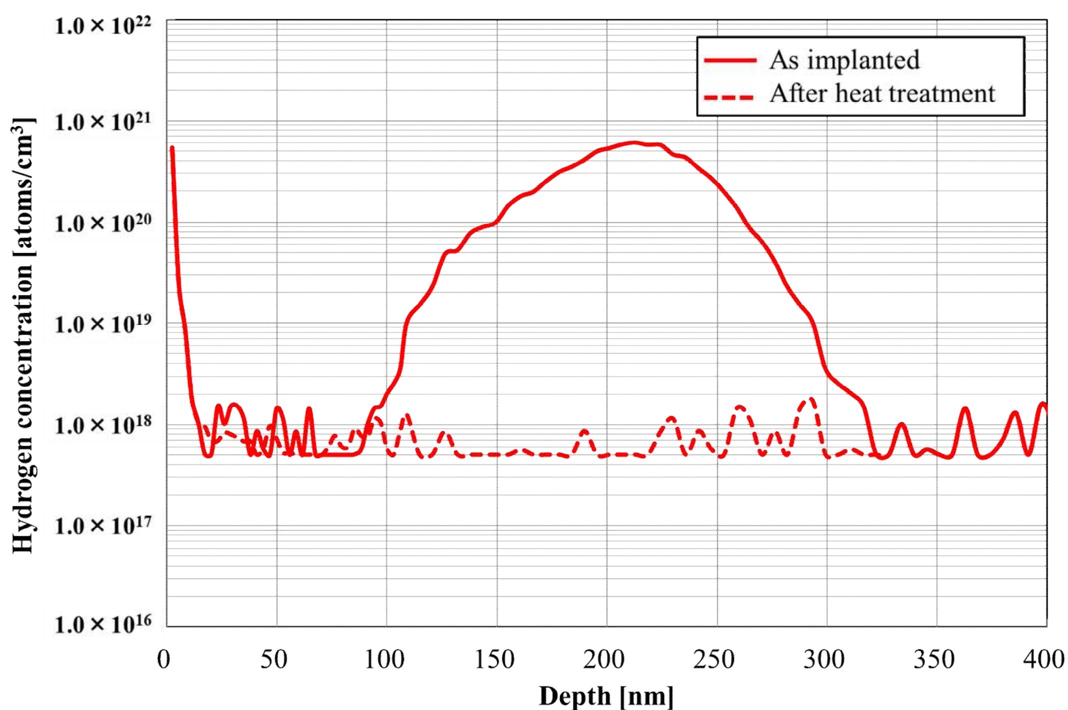

Figure 4.3: SIMS profiles of as-implanted sample and after 600°C annealing of sample with monomer hydrogen implantation.

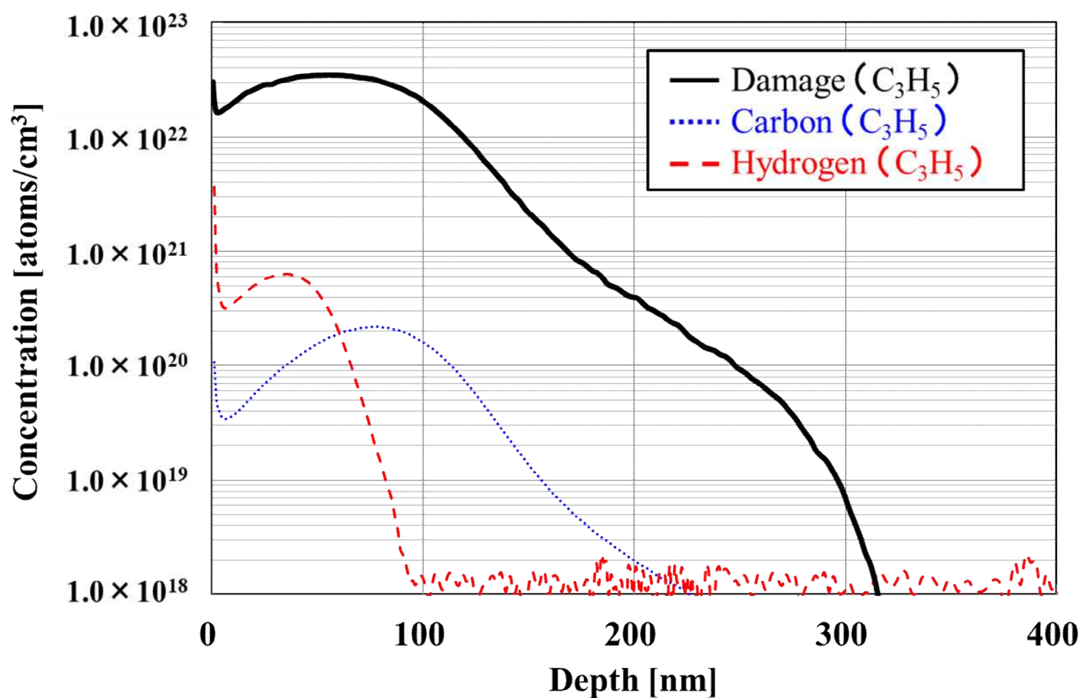

Figure 4.4: Simulated damage profiles of C_3H_5 and monomer carbon implantation by TCAD simulator sentaurus process and SIMS profiles of carbon and carbon with hydrocarbon-molecular-ion.

Next, I investigated the hydrogen diffusion behavior after epitaxial growth. Figure 4.5 shows the SIMS profile of the after-epitaxial-growth sample with a C_3H_5 dose of 3.3×10^{14} molecular ions/cm^2. A hydrogen peak was confirmed in the implanted region. The hydrogen peak concentration was 1.2×10^{18} atoms/cm^3, and the epitaxial growth temperature was high, approximately 1100°C. However, hydrogen was observed after epitaxial growth.

Figure 4.6 shows that the hydrogen-peak concentration after epitaxial growth depends on the C_3H_5 dose. The hydrogen-peak concentration increased along with the C_3H_5 dose because the peak of damage of C_3H_5 implantation and carbon concentration depends on the C_3H_5 dose. Therefore, the hydrogen concentration in the implanted region increased depending on the C_3H_5 dose. I then evaluated the diffusion behavior of hydrogen after the annealing of the epitaxially grown sample. Figure 4.7 shows the SIMS profile of hydrogen after annealing for 30 min at temperatures from 300 to 900°C at 200°C intervals. No change in hydrogen peak concentration was observed after annealing at 300°C. I confirmed that the decrease in hydrogen-peak concentration depended on temperature. However, hydrogen remained after the 900°C annealing. Such a hydrogen-diffusion behavior has not been reported. The hydrogen diffusion velocity in silicon is extremely high. Thus, I found that the hydrocarbon-molecular-ion implanted region exhibits a high trapping capability for hydrogen.

Figure 4.8 shows a plot of integral values in a 1.0 μm region around the hydrogen peak after annealing from 600 to 900°C for 30 min. From these results, I calculated the diffused hydrogen density to compare the interface state density. The finite difference in out-diffused hydrogen density before and after annealing was calculated. The out-diffused hydrogen density after annealing at 600 to 900°C were approximately from 1.0×10^{12} to 9.0×10^{12} atoms/cm^2. In contrast, the SiO_2/Si interface state density was approximately from 1.0×10^{10} to 1.0×10^{11} atoms/cm^2. As a result, the out-diffused hydrogen density was higher than the interface state density. I assumed that the out-diffused hydrogen density is sufficient for the passivation of the interface state density.

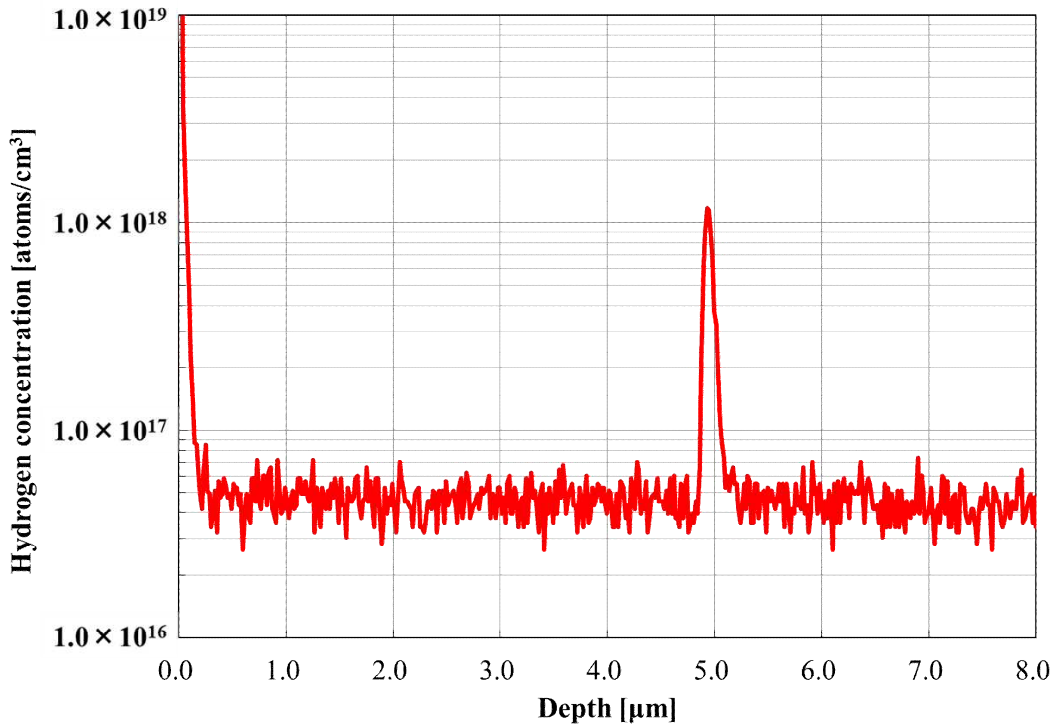

Figure 4.5: SIMS profile of hydrogen after epitaxial growth with C_3H_5 dose of 3.3×10^{14} atoms/cm^2.

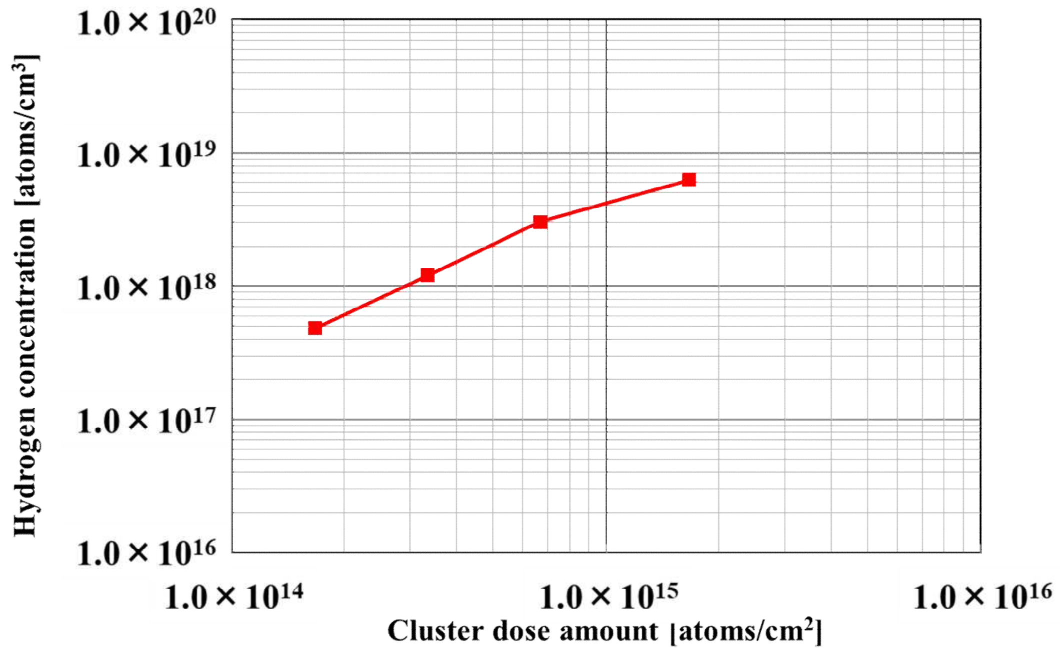

Figure 4.6: Dependence of hydrogen-peak concentration after epitaxial growth on C_3H_5 dosage.

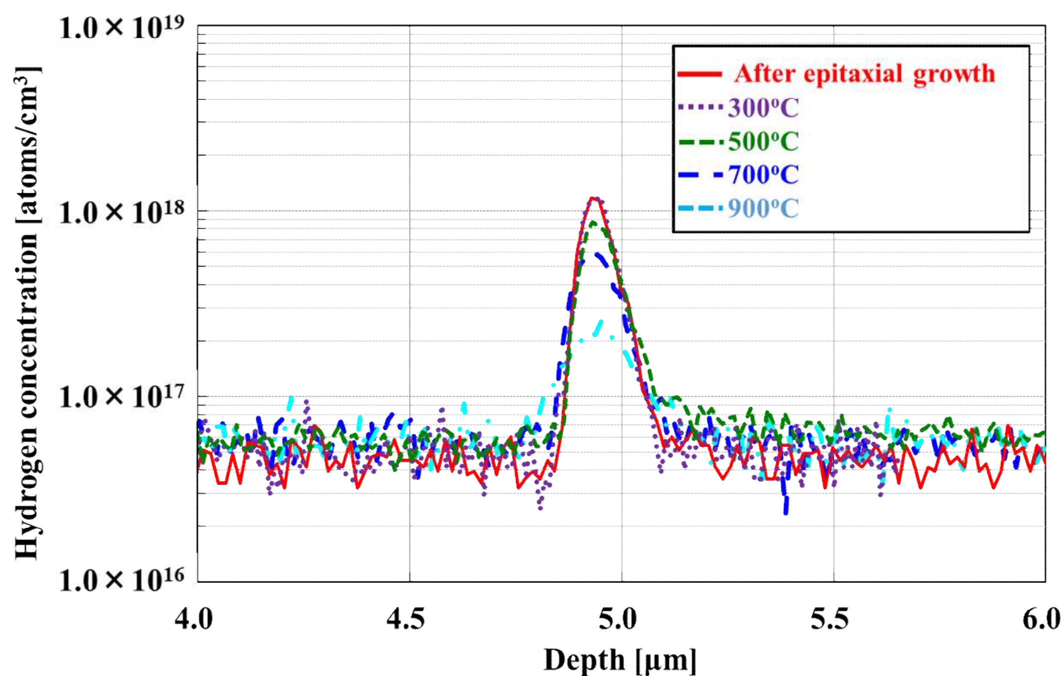

Figure 4.7: SIMS profile of hydrogen after annealing at 300 to 900°C for 30 min at 200°C intervals.

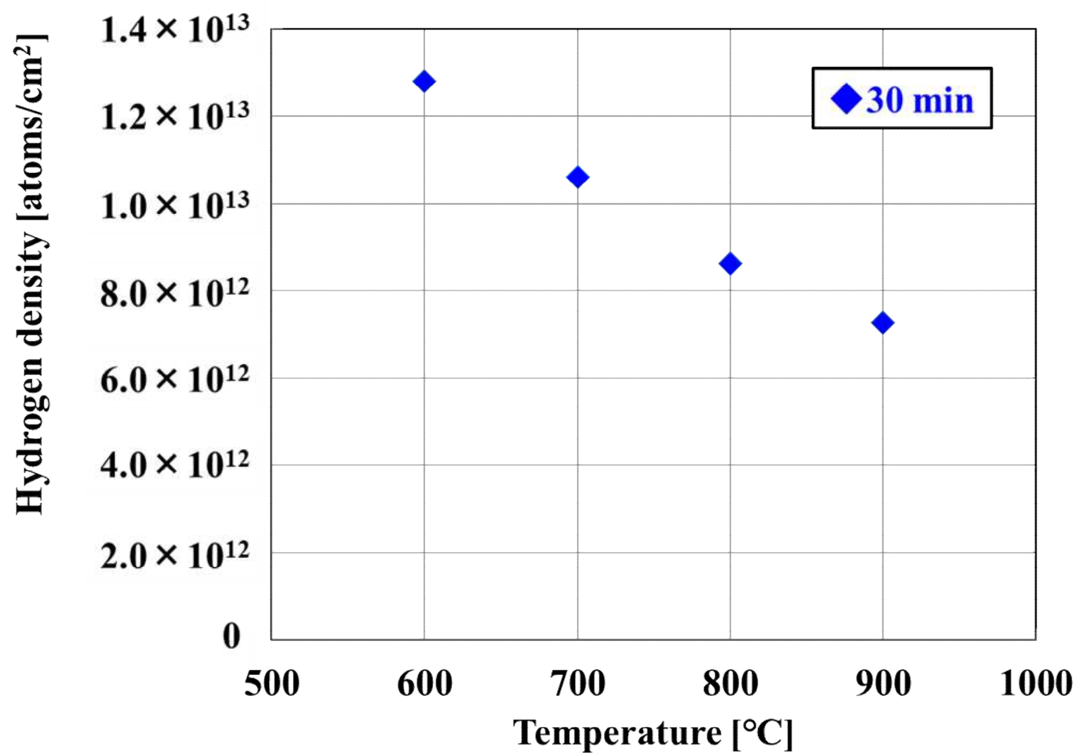

Figure 4.8: Plot of integral values in 1.0 μm region around hydrogen peak after annealing from 600 to 900°C for 30 min.

I inferred that the hydrocarbon-molecular-ion implanted region comprises carbon, hydrogen, oxygen, and vacancy. Thus, I assume that these complexes form a potential barrier to hydrogen dissociation in the implanted region. Therefore, I calculated the dissociation activation energy of hydrogen from the implantation defect. I calculated the dissociation activation energy assuming only a dissociation reaction. For the reaction of hydrogen from an implantation defect (D in the equations below) to be a dissociation reaction and ignoring the inverse reaction, the density of dissociated hydrogen can be expressed by the following reaction and kinetic equations:

$$HD \rightarrow H + D, \tag{4.1}$$

$$\frac{dD_{HD}}{dt} = -kD_{HD}, \tag{4.2}$$

where D_{HD} is the density of H and defect complexes in the implantation region. Thus, D_{HD} is the H density obtained by SIMS analysis. The hydrogen density after annealing at each temperature is expressed as

$$lnD(t) = lnD(0) - kt, \tag{4.3}$$

where $D(t)$ is the hydrogen density after annealing and (0) is the initial hydrogen density. The annealing time is t and k is the reaction rate constant.

Figure 4.9 shows semilogarithmic plots for annealing at 500 to 900°C at 100°C intervals with the logarithm of hydrogen density on the vertical axis and annealing time on the horizontal axis. The error bars in Figure 4.9 show the minimum and maximum measured hydrogen density. The time dependence of the hydrogen diffusion behavior is linear. This demonstrates that the hydrogen diffusion behavior can be expressed using the reaction model only for dissociation. In accordance with Figure 4.9, the reaction rate constant k was calculated. The error bar of the reaction rate constant was 5% at most.

Figure 4.10 shows an Arrhenius plot of the reaction rate constants obtained from Figure 4.9. The dissociation activation energy was estimated to be about 0.76 ± 0.04 eV. I assumed a simple reaction model on the basis of the dissociation behavior from a defect formed in the implanted region, and the result of the dissociation behavior indicated good agreement with equation 4.3. I discuss the dissociation activation energy and binding state of trapped hydrogen in the next section.

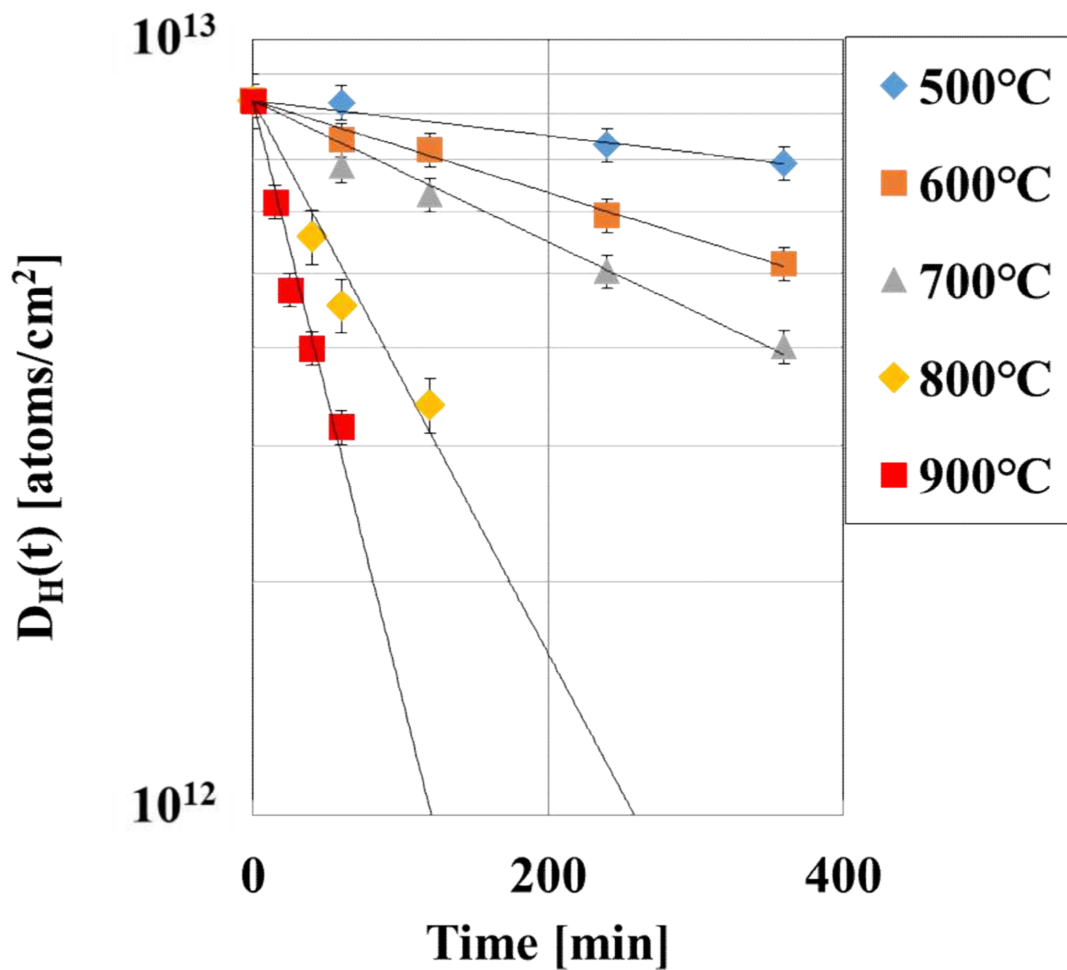

Figure 4.9: Plots of logarithm of hydrogen concentration on vertical axis and annealing time on horizontal axis.

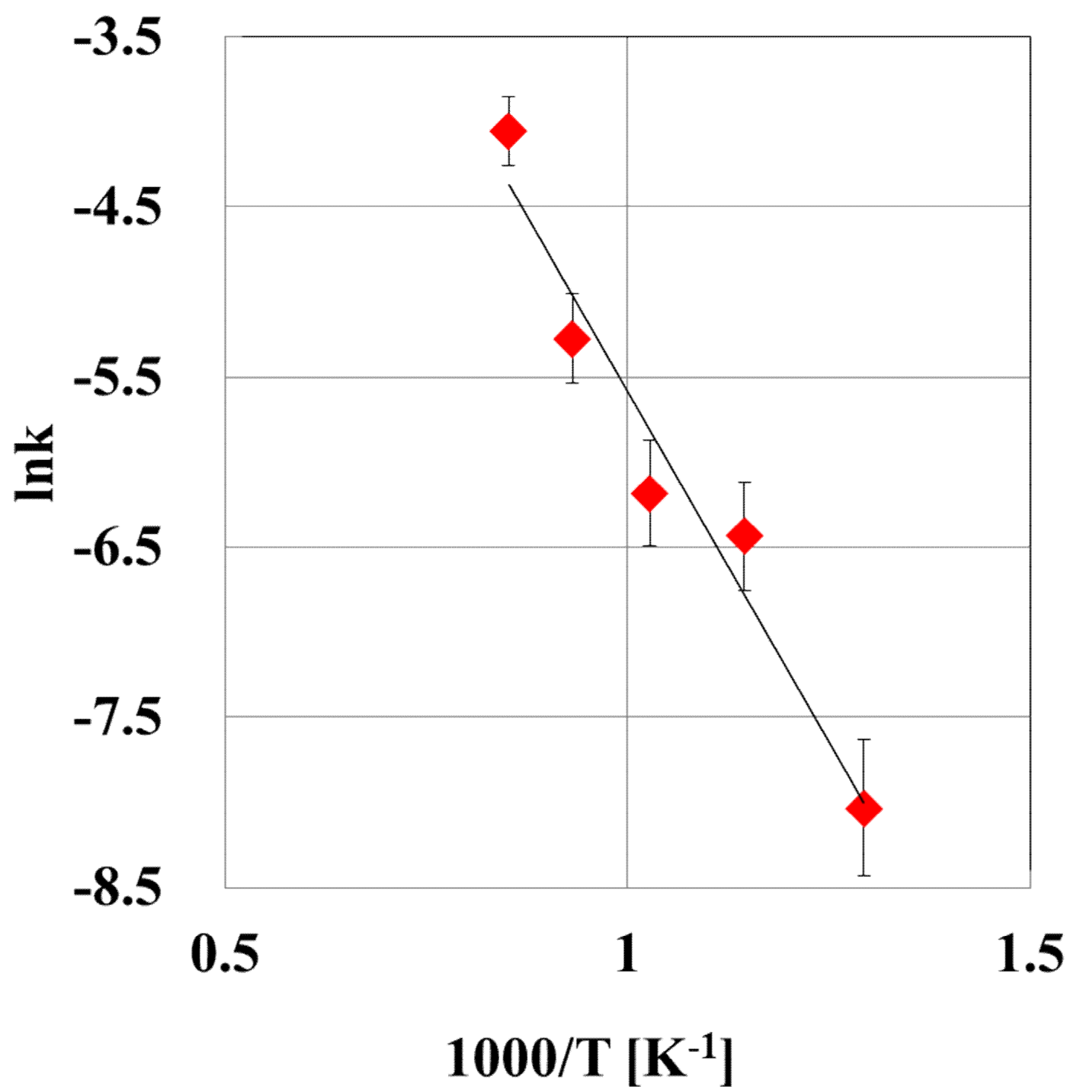

Figure 4.10: Arrhenius plot of reaction rate constant k.

4.4 Mechanism of hydrogen out-diffusion behavior in small thermal budget

Previous studies have revealed the binding states and diffusion behavior of hydrogen in silicon [99–105]. In particular, the low-temperature annealing behavior and binding state of hydrogen from 100 to 700°C have been investigated [113–115]. Fukata and Suezawa demonstrated that vacancy and void defects form complexes and binding states with hydrogen in C-doped silicon after hydrogen FGA [113]. Previous studies indicated that hydrogen in complexes with vacancy (*e.g.*, VH_4 and V_2H_6) was dissociated after annealing at less than 600°C. On the other hand, the Si-H binding state of hydrogen trapped in voids has been reported for annealing at 700°C. For implantation defect analysis, I observed, through high-resolution cross-sectional transmission electron microscopy (HR-XTEM), that voids or platelet defects were formed in the hydrocarbon-molecular-ion implanted region.

Figure 4.11 shows the HR-XTEM image and nanobeam electron diffraction (n-ED) pattern of the after-epitaxial-growth sample. The hydrocarbon-molecular-ion implantation defects were observed in the implanted region, as shown in Figure 4.11(a). As shown Figure 4.11(b), a defect of approximately 5 nm was found to have been formed in the implanted region. It was also revealed that these defects were the electron diffraction patterns of a silicon single crystal by n-ED in Figure 4.11 (c). I assumed that the defect of approximately 5 nm was due to the substitution and interstitial carbon clustering in the hydrocarbon-molecular-ion implanted region. Voids or platelet defects were not observed in the hydrocarbon-molecular-ion implanted region. Consequently, hydrogen detected in the hydrocarbon-molecular-ion implanted region of was not the binding state trapped by voids and platelet defects. For V-H complexes, vacancy formed by hydrocarbon-molecular-ion implantation may possibly result in hydrogen trapping. However, dissociation did not progress at low temperatures in our study, as shown in Figure 4.7. Therefore, I assumed that the binding state of hydrogen trapped in the hydrocarbon-molecular-ion implanted region is different from that found in previous studies. I give two possibilities for the binding state of hydrogen in the hydrocarbon-molecular-ion implanted region. One is a binding state in which hydrogen is trapped by the carbon impurities in the hydrocarbon-molecular-ion implanted region. The formation of a hydrogen pair (H_2) trapped by carbon impurities in C-rich silicon was observed by Hourahine et al [62]. They also reported that the binding energy of a hydrogen molecule to a carbon impurity in the C-H_2 defect is 0.8 eV. Therefore, the C-H binding state is suggested by the dissociation activation energy. However, this result was also investigated in terms of the hydrogen

diffusion behavior after low-temperature annealing up to 400°C. Regarding the complex in the hydrocarbon-molecular-ion implanted region, I assumed that the binding state of hydrogen is complex in this study because hydrogen trapped in the implanted region begins to diffuse after annealing above 500°C. It is believed that the complex carbon impurities in the implanted region participate in the behavior of hydrogen diffusion at high temperatures. Regarding the behavior of carbon impurities in silicon bulk, Pinacho *et al.* demonstrated that carbon and silicon self-interstitial (CI) clusters are formed in C-rich silicon [61]. I assumed that these CI clusters are formed in the hydrocarbon-molecular-ion implanted region because the implanted region of carbon is extremely shallow and at high concentrations. As shown Figure 4.2, a carbon peak shift was confirmed after annealing and is in accordance with a hydrogen peak. Therefore, I hypothesize that the hydrogen in the hydrocarbon-molecular-ion implanted region forms a binding state with the CI cluster. The other binding state of hydrogen is considered to be the hydrogen molecule state. Markevich and Suezawa demonstrated that the activation energy for the diffusion of hydrogen molecules located at the T_d site is 0.78 eV [63]. In addition, it has been reported that the activation energy is estimated to be 0.7 eV when hydrogen molecules dissociate from multivacancies [64, 65, 116–118]. The activation energy of these hydrogen molecules is extremely close to what I calculated.

Figures 4.12 (a) and (b) show a schematic of a hydrogen molecule at the T_d site of a unit cell of a silicon crystal and the dissociation of a hydrogen molecule trapped at a multivacancy, respectively. Therefore, I assume that the hydrogen in the hydrocarbon-molecular-ion implanted region diffuses in the hydrogen as the above molecule state. As shown in Figures 4.2 and 4.4, the hydrogen in the molecular ion implanted region is trapped in the vacancy peaks formed by hydrocarbon-molecular-ion implantation.

I infer that complexes related to CI clustering and vacancy in the hydrocarbon-molecular-ion implanted region form a potential barrier to hydrogen dissociation. In these complexes, it is considered that hydrogen diffusing from the implanted region is attributed to the C-H_2 binding state in C clustering and the hydrogen molecules trapped in the vacancy formed by C-cluster ion implantation and is located at the T_d site.

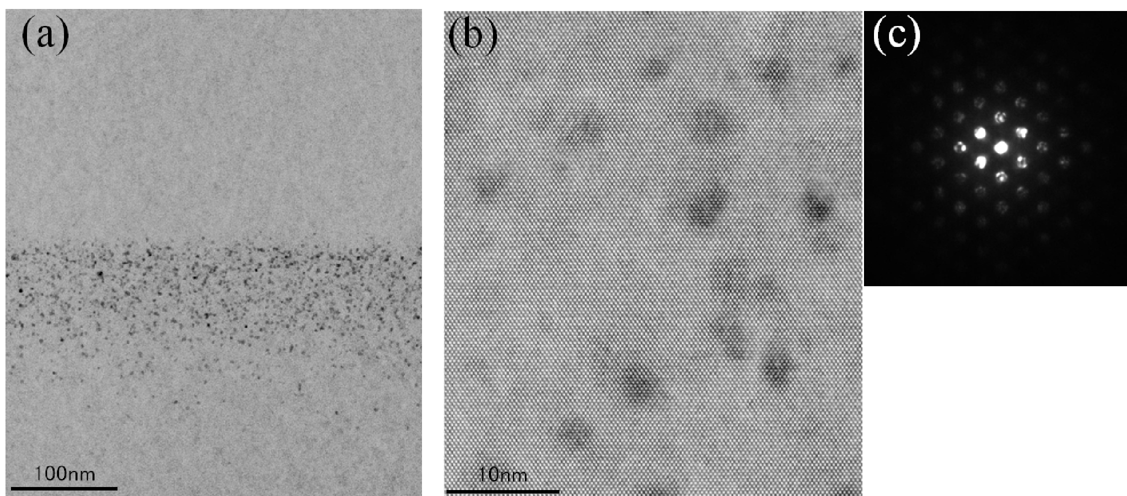

Figure 4.11: HR-XTEM images of (a) low, (b) high magnification and (c) Electron diffraction pattern from n-ED observation with carbon dose of 1.0×10^{15} carbon atoms/cm^2 for after-epitaxial-growth sample.

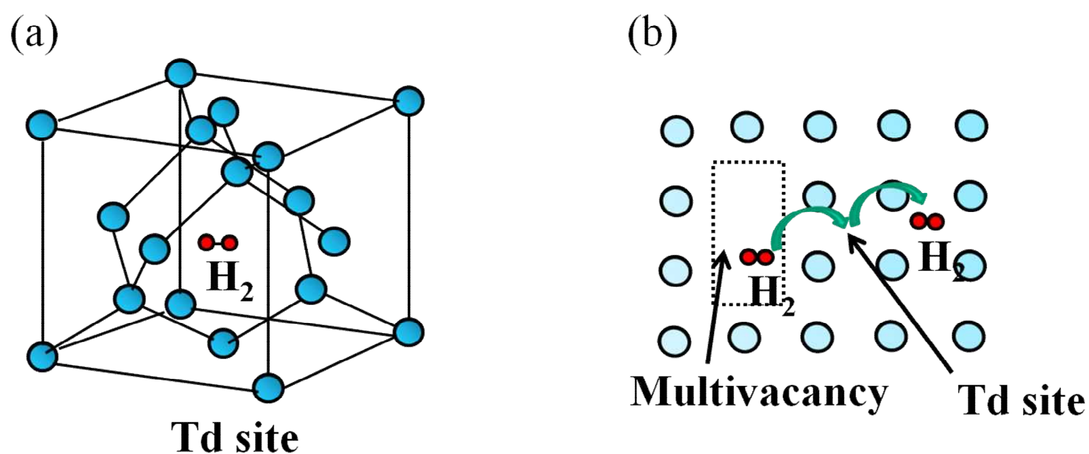

Figure 4.12: Schematic of (a) hydrogen molecule at T_d site of unit cell of silicon crystal and (b) dissociation process of hydrogen molecule trapped at multi-vacancy.

4.5 Summary

I used a hydrocarbon-molecular-ion containing hydrogen (C_3H_5). After hydrocarbon-molecular-ion implantation to a silicon wafer, I confirmed that not only the carbon profile but also the hydrogen profile could be obtained through SIMS analysis. Additionally, after 900°C annealing, I observed that the implanted region had a hydrogen peak. The depths of the carbon and hydrogen peaks after annealing were the same as that of the vacancy peak just after implantation through TCAD simulation. On the other hand, monomer-implanted hydrogen diffused out below the detection limit after 600 °C annealing. Hydrogen was also confirmed after epitaxial growth, although the diffusion velocity of hydrogen was extremely high in the silicon wafer. The hydrogen peak concentration increased depending on the dose after epitaxial growth, but decreased depending on temperature after diffusion annealing. The out-diffused hydrogen density from 600 to 900°C was approximately from 1.0×10^{12} to 9.0×10^{12} atoms/cm^2. I assumed that the out-diffused hydrogen density sufficiently represents interface state density because the SiO_2/Si interface state density is approximately from 1.0×10^{10} to 1.0×10^{11} atoms/cm^2. I also derived the dissociation activation energy assuming only a dissociation reaction. The activation energy of hydrogen dissociation from the hydrocarbon-molecular-ion implanted region was calculated to be 0.76 ± 0.04 eV. This activation energy is extremely close to the binding energy of the CH_2 defect and the activation energies for the diffusion of hydrogen molecules located at the T_d site and hydrogen molecules from multi-vacancies. In summary, I inferred that trapped hydrogen in the hydrocarbon-molecular-ion implanted region forms complexes comprising the C-H binding state and hydrogen molecules.

Chapter 5

Kinetic analysis of hydrogen diffusion behavior with TCAD simulation

5.1 Introduction

Previous chapter demonstrated that hydrocarbon-molecular-ion implanted silicon epitaxial wafers have hydrogen dissociation behavior for high-performance CMOS image sensors. A hydrogen in the implanted region of a hydrocarbon-molecular-ion is trapped after epitaxial growth and out-diffused in accordance with the subsequent annealing temperature. Consequently, I assume that hydrogen out-diffusing from the implanted region during the device fabrication process can passivate the interface state density of the isolation region and process-induced defects. Therefore, the hydrogen diffusion behavior can contribute to the high performance of CMOS image sensors by lowering photo-diode junction leakage current and fixed-pattern noise [24,36]. Conventionally, hydrogen diffusion velocity is extremely high in bulk silicon at high temperature [66, 89, 90]. Thus, only monomer-implanted hydrogen diffused to below the detection limit of secondary ion mass spectrometry (SIMS) analysis after low-temperature annealing at 600°C [32]. However, hydrocarbon-molecular-ion implanted hydrogen remains in the implanted region after annealing at 900°C. Such hydrogen diffusion behavior has not been reported in any other previous study. In addition, above section demonstrated that the dissociation activation energy of hydrogen to dissociate from the implanted region of a hydrocarbon-molecular-ion is 0.76 ± 0.04 eV. This activation energy is extremely close to the binding energy of the C-H_2 defect and the activation energy for the diffusion of hydrogen molecules from tetrahedral interstitial sites and multi-vacancy [64, 65, 88, 116, 117]. The C-H binding state in silicon has also been reported in some previous studies [62, 118–

120]. However, previous studies have reported the analytical results of binding state and diffusion behavior after annealing below 700°C [113, 114, 121]. In our previous study, I performed epitaxial growth at approximately 1100°C and found that a hydrogen was trapped in the implanted region of a hydrocarbon-molecular-ion to900 °C after the subsequent annealing. Therefore, the hydrogen binding state in the implanted region of a hydrocarbon-molecular-ion is presumed to differ from the C-H binding state reported conventionally [64, 65, 116, 117]. Regarding the carbon behavior in silicon, Pinacho *et al.* indicated that carbon and silicon self-interstitial (I) formed a C_mI_n (*e.g.*, C_3I_3 and C_3I_2) cluster (CI cluster) in C-rich silicon [61]. The carbon peaks in the hydrocarbon-molecular-ion implanted region are either extremely shallow or high. In addition, I is considered to be formed by hydrocarbon-molecular-ion implantation. Consequently, results of above section suggest that a CI cluster can be formed in the implanted region of a hydrocarbon-molecular-ion. Furthermore, other studies have indicated that the complexes of hydrogen, vacancy (V), and I in the implanted region have gettering capability for metallic impurities [44]. Therefore, the trapping and diffusion behavior of hydrogen in the implanted region must be analyzed to understand the gettering mechanism and passivation effect behind hydrocarbon-molecular-ion implanted epitaxial wafers. In this section, I examine trapping and diffusion behavior for hydrogen by means of a technology computer aided design (TCAD) simulation assuming a reaction model in which a CI-cluster binds to hydrogen [52].

5.2 Theoretical and experimental methods

For our calculations, I have used the TCAD Sentaurus process from Synopsys Inc. [52]. The TCAD Sentaurus process is easily extendable due to its modelling capabilities and broad database. Furthermore, the model for the formation of a C_mI_n (CI) cluster is incorporated in the TCAD Sentaurus process [52, 61]. Therefore, I simulated the hydrocarbon-molecular-ion implanted silicon epitaxial wafer fabrication process by using TCAD Sentaurus process due to confirmation the formation of a CI cluster. Figure 5.1 shows the profile of carbon total (dotted line), C_3I_3 (solid line), C_3I_2 (solid line), and interstitial carbon (Ci) (dashed line) after epitaxial growth with C_3H_5 dose of 1.6×10^{14} molecular ions/cm^2 by using TCAD simulation. Epitaxial silicon layers of 4.0 μm thickness were grown at 1100°C. The epitaxial growth rate was 1.0 μm/min. These results indicate that the peak of carbon in the hydrocarbon-molecular-ion implanted region is mainly formed by C_3I_3 and C_3I_2. In particular, C_3I_3 concentration is the highest in the implanted region from TCAD simulation. Consequently, I define a reaction model in which hydrogen binds to a C_3I_3 cluster for TCAD simulation. The reaction of hydrogen and C_3I_3 can be expressed by the following simple reaction and kinetic equations,

$$H - C_3I_3 \rightarrow H + C_3I_3, \tag{5.1}$$

$$\frac{dC_{H-C_3I_3}}{dt} = k_1 C_H C_{C_3I_3} - k_2 C_{H-C_3I_3}, \tag{5.2}$$

$$\frac{dC_H}{dt} = D_H grad(H) - k_1 C_H C_{C_3I_3} + k_2 C_{H-C_3I_3}, \tag{5.3}$$

$$D_H = 9.4 \times 10^{-3} exp(-\frac{0.48[eV]}{k_B T})\ [cm^2/s], \tag{5.4}$$

where C_H-C_3I_3, C_H, and C_{C3I3} are the concentration of H-C_3I_3, hydrogen, and C_3I_3 in the hydrocarbon-molecular-ion implanted region, respectively. The t is annealing time. D_H is the diffusion coefficient of hydrogen [66, 89, 90]. The k_B is Boltzmann constant ant T is annealing temperature. k_1 and k_2 are the reaction rate constant of the order and inverse reaction, respectively. The reaction rate constant k_n (n = 1 or 2) can be expressed by the following equation,

$$k_n = A_n exp(-\frac{E_n}{k_B T})\ (n = 1\ or\ 2) \tag{5.5}$$

The $A_1 = 1.2 \times 10^{-14}$ cm^3/s, E_1=0.12 eV, A_2=72 s^{-1}, and E_2=0.76 eV are used for the frequency factor and the activation energy derived in the previous

study [36]. The actual activation energy of E_1 for the inverse reaction in equation (1) is estimated to be calibrated by using the experimental data of hydrogen diffusion at high temperature. The activation energy of E_1 is lower than the hydrogen diffusion activation energy of 0.48 eV. Consequently, I consider that the attraction reaction between hydrogen and C_3I_3 progressed during high temperature epitaxial growth. In addition, the initial conditions of the simulation are CH : hydrogen concentration after hydrocarbon-molecular-ion implantation, $CC_3I_3 = 0$, and $CH\text{-}C_3I_3 = 0$. I assumed that a formation of C_3I_3 cluster and formation reaction of H-C_3I_3 progressed at the same time during epitaxial growth. Furthermore, hydrogen does not diffuse in a silicon wafer from an atmosphere during epitaxial growth in this TCAD simulation. Consequently, I simulated only diffusion behavior of hydrocarbon-molecular-ion implanted hydrogen. In this study, Si (100) n-type wafers were implanted with C_3H_5 cluster ions at room temperature. The C_3H_5 cluster dose was $1.6 \times 10^{14} - 6.6 \times 10^{14}$ molecular ions/cm^2. The implantation energy was 80 keV/molecular ion. After hydrocarbon-molecular-ion implantation, epitaxial silicon layers of 4.0 μm thickness were grown using a Si_3HCl gas source at 1100°C. The epitaxial growth rate was 1.0 μm/min. The samples were then annealed at 900°C for 60 min in a nitrogen atmosphere. The annealing temperature and time conditions are the same as those of the TCAD simulation and experiment. The distribution of hydrogen in the hydrocarbon-molecular-ion implanted region was analyzed by TCAD simulation and SIMS.

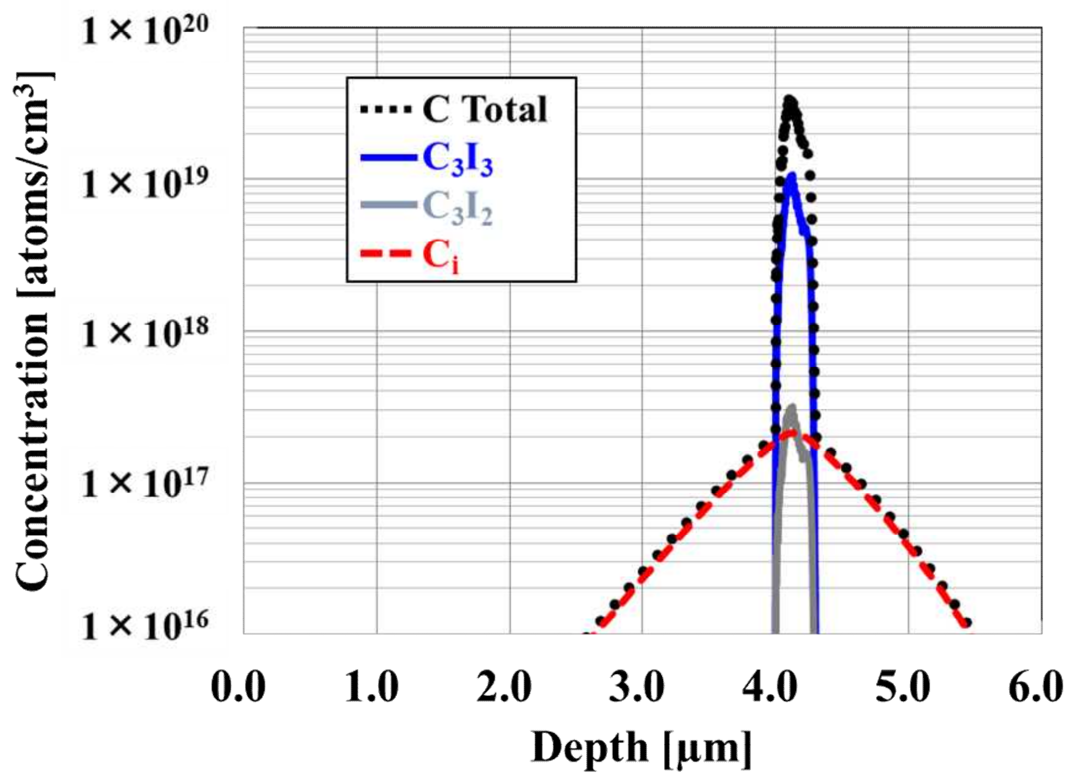

Figure 5.1: The profile of carbon total (dotted line), C_3I_3 cluster (solid line), C_3I_2 cluster (solid line), and Ci (dashed line) after epitaxial silicon growth at 1100°C with C_3H_5 dose of 1.6×10^{14} molecular ions/cm^2 by TCAD simulation.

5.3 Trapping and diffusion behavior of hydrogen simulated by TCAD

Figure 5.2 shows the depth profiles of hydrogen after epitaxial silicon growth at 1100°C with a C_3H_5 dose of 3.3×10^{14} molecular ions/cm^2 by the TCAD simulation (solid line) and SIMS analysis (dotted line). The TCAD profile clearly agrees with the SIMS profile after epitaxial growth. Furthermore, Figure 5.3 shows the hydrogen profiles after 900°C, 60-min annealing in a nitrogen atmosphere with a C_3H_5 dose of 3.3×10^{14} molecular ions/cm^2. I calculated the dissociation behavior of hydrogen after 900°C, 60-min annealing by the reaction model of hydrogen and C_3I_3 and found that the CI-cluster contributes to trapping and diffusion behavior of hydrogen in the implanted region of the hydrocarbon-molecular ion ion-implantation. The epitaxial growth temperature is 1100°C at high temperature. Furthermore, the CI-cluster in the implanted region of the hydrocarbon-molecular ion is stable after 900°C, 60-min annealing.

Figure 5.4 shows dependence on the C_3H_5 dose of the hydrogen peak concentration with TCAD after epitaxial silicon growth at 1100°C and after annealing at 900°. These investigation results demonstrate that trapping and diffusion behavior of hydrogen is simulated by the reaction model in which hydrogen was assumed to be bound to a CI-cluster. As shown in Figures 5.2 and 5.3, the calculation results for the TCAD simulation provide the same hydrogen concentration profile as results for the SIMS analysis after epitaxial growth and annealing. Furthermore, the hydrogen peak concentration in the implanted region of the hydrocarbon-molecular ion depends on the C_3H_5 dose after annealing at 900°C for 60 min in a nitrogen atmosphere. Consequently, C_3I_3 is presumed to be thermally stable. I define C_3I_3 as a CI-cluster in this study. Therefore, these results revealed that thermal stability of the CI-cluster contributes to the trapping and diffusion behavior of hydrogen.

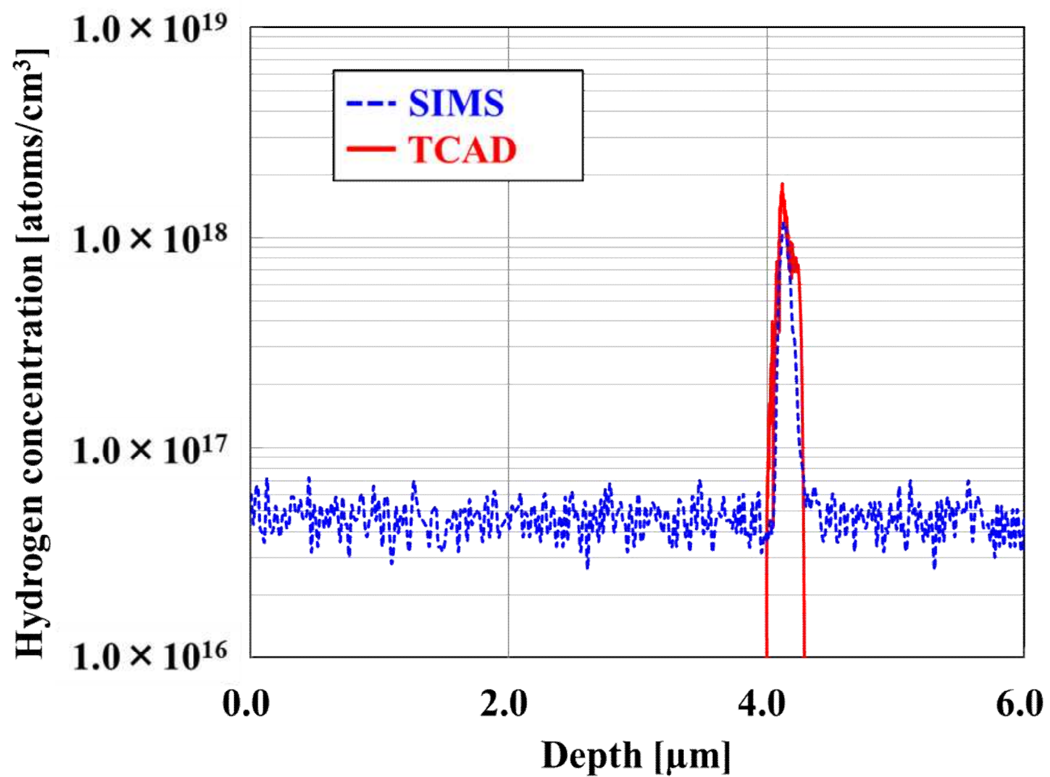

Figure 5.2: Depth profile of hydrogen after epitaxial silicon growth at 1100°C with SIMS analysis and TCAD simulation with C_3H_5 dose of 3.3×10^{14} molecular ions/cm^2.

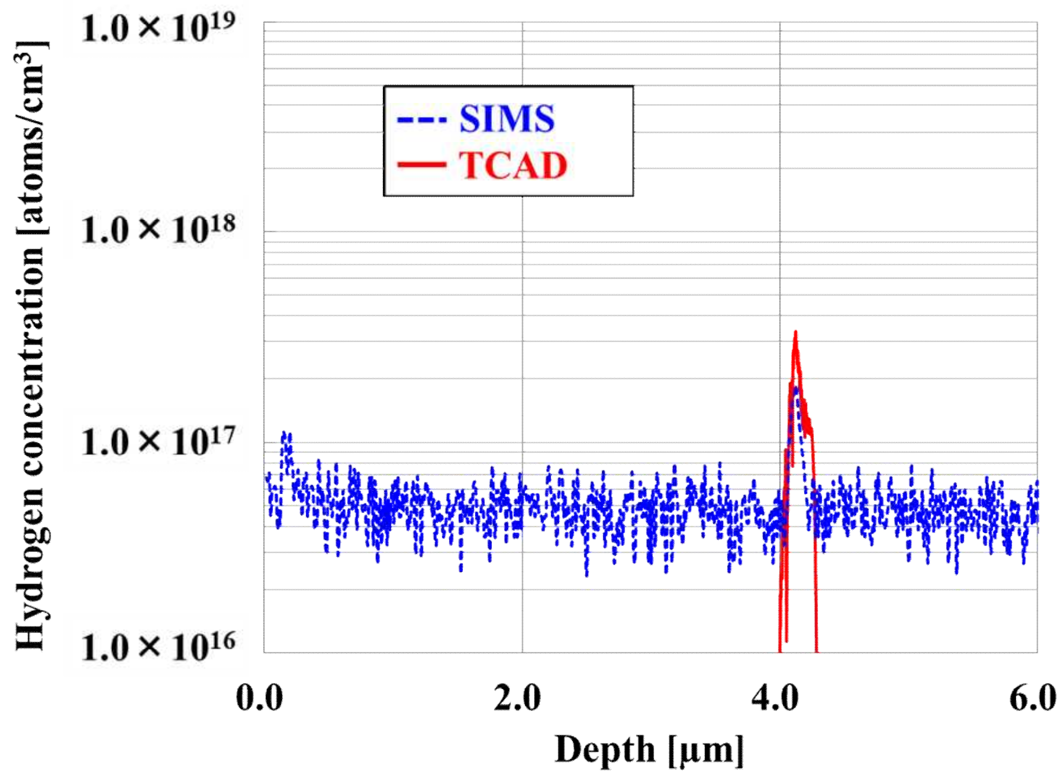

Figure 5.3: Depth profile of hydrogen after 900°C, 60-min annealing in a nitrogen atmosphere with SIMS analysis and TCAD simulation with C_3H_5 dose of 3.3×10^{14} molecular ions/cm^2.

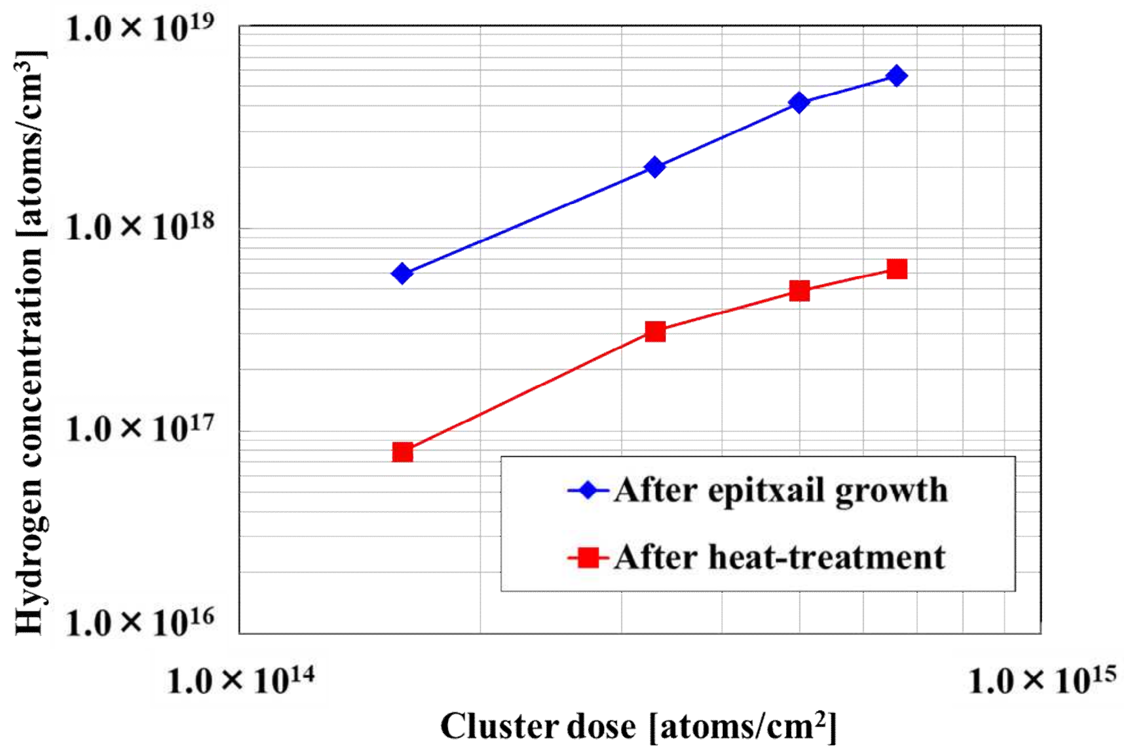

Figure 5.4: Dependence of hydrogen-peak concentration after epitaxial silicon growth at 1100°C and after annealing at 900°C for 60 min in a nitrogen atmosphere with TCAD simulation on C_3H_5 dose.

5.4 Mechanism of hydrogen trapping and diffusion behavior

Previous studies have demonstrated the binding state and diffusion behavior of hydrogen in bulk Si [99–105]. They reported the analytical results of the binding state and diffusion behavior after annealing below 700°C. Other studies have reported the C-H binding state in Si bulk [62, 64, 119, 120]. They also analyzed the C-H binding state after low-temperature annealing below 700°C. Hydrogen diffuses easily at annealing above 700°C [66, 89, 90]. However, I revealed that hydrogen is trapped in the implanted region of a hydrocarbon-molecular ion after epitaxial growth. In addition, I found that hydrogen in the implanted region of a hydrocarbon-molecular ion gradually diffused after the subsequent annealing at high temperature [36]. The carbon in the implanted region of the hydrocarbon-molecular ion has extremely high or shallow peaks because a hydrocarbon-molecular ion implantation is very low energy and can implant many carbon atoms simultaneously. Thus, it seems likely that carbon in the implanted region of a hydrocarbon-molecular ion contributes to the C-H binding formation. However, I speculate that the C-H binding state in the implanted region is not simple during the high-temperature annealing. Consequently, I suggest that the trapping and diffusion behavior of hydrogen is caused by CI-cluster formation in the implanted region of the hydrocarbon-molecular ion. As a result, SIMS analysis results agree with the TCAD simulation results after epitaxial growth and annealing at high temperature, as shown in Figures 5.2 and 5.3.

Therefore, I hypothesize that formation of a CI-cluster in the implanted region strongly cause trapping and diffusion behavior of hydrogen. I used TCAD to simulate the carbon (C), hydrogen (H), and Si-interstitial (I) profiles to confirm the formation of a CI-cluster in the hydrocarbon-molecular ion implanted region. Figure 5.5 shows the C, H, and I profiles after C_3H_5 implantation with a dose of 1.67×10^{14} (dashed line) and 3.3×10^{14} (solid line) molecular ions/cm^2. The I concentration is higher than C and H concentrations in the implanted region of the hydrocarbon-molecular ion. Furthermore, I concentration peaked approximately 60 nm from surface, where its dependence on the C_3H_5 dose notably increased. Previous section shows that the 60-nm-deep Si-interstitial peak corresponds to the carbon and hydrogen peaks after annealing.

Consequently, I assumed that a CI-cluster is formed by carbon and silicon interstitial due to hydrocarbon-molecular ion implantation in the implanted region and binds to hydrogen implanted with a hydrocarbon-molecular ion during epitaxial growth annealing. On the other hand, another possibility is that carbon and

vacancy (V) form a complex in the implanted region of a hydrocarbon-molecular ion. However, Shirasawa *et al.* used density functional theory (DFT) calculations to demonstrate that a C-V complex is not a possible candidate for gettering sinks [44]. In contrast, they reported interstitial carbon and silicon interstitial complexes to be effective gettering sinks.

In addition, it is reported that hydrogen is trapped in voids or {111} platelet defects formed by phosphorus implantation [100, 121]. Therefore, I observed the implanted region of the sample after annealing at 900°C for 60 min for implantation defect analysis by high-resolution transmission cross-sectional transmission electron microscopy (HR-XTEM). Figure 5.6 (a) and (b) show HR-XTEM images of low magnification and high magnification. Voids and platelet defects were not observed in the implanted region, but a defect of approximately 5 nm was. I define C_3I_3 as a CI-cluster. However, it seems likely that other CI-clusters are also formed in the hydrocarbon-molecular-ion implanted region. Therefore, I inferred that the defects observed in Figure 5.6 are an aggregate of a CI-cluster. Furthermore, the defects were found to be stable after high-temperature annealing.

Consequently, if a larger CI-cluster is formed in the implanted region, I assume that it will be more stable after annealing at high temperature. This suggests that a stable trapping site with a CI-cluster contributes to trapping capability for the hydrogen of the hydrocarbon-molecular-ion implanted silicon epitaxial wafer.

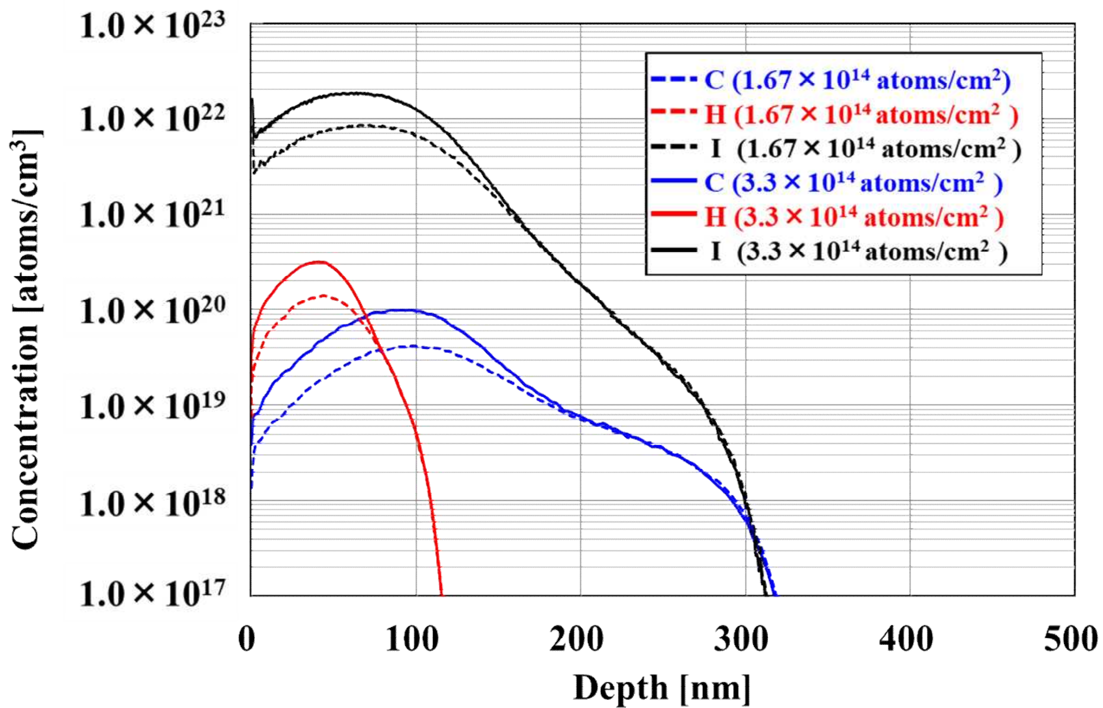

Figure 5.5: Simulated carbon (C), hydrogen (H), and silicon interstitial (I) profiles of C_3H_5-molecular ion implantation by TCAD simulation.

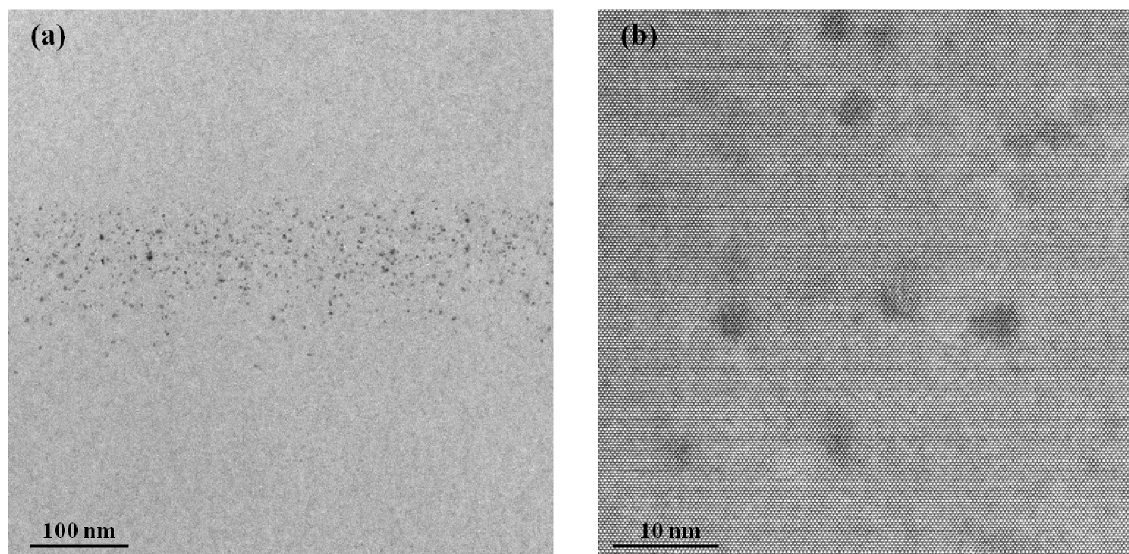

Figure 5.6: HR-XTEM images of (a) low and (b) high magnification with carbon dose of 3.3×10^{14} atoms/cm^2 after epitaxial growth and annealing at 900°C for 60 min sample.

5.5 Summary

I demonstrated that the trapping behavior of hydrogen in the implanted region of a hydrocarbon-molecular-ion after epitaxial growth can be calculated by technology computer aided design (TCAD) with a reaction model in which hydrogen binds to a carbon and Si self-interstitial (CI)-cluster. The diffusion behavior of hydrogen was also demonstrated after annealing using the same re-action model of hydrogen and CI-cluster binding. This indicates that the CI-cluster in the implanted region of the hydrocarbon-molecular ion significantly contributes to the trapping behavior of hydrogen. The results after high-temperature annealing indicate that hydrogen in the implanted region of a hydrocarbon-molecular ion must gradually be diffusing out to the device active region during a device process. Consequently, interface state density is seemingly passivated by hydrogen diffused from the implanted region of the hydrocarbon-molecular ion. Such trapping and diffusion behavior of hydrogen has not been reported in previous studies. I conclude that hydrogen diffusion behavior in the implanted region of a hydrocarbon-molecular ion can contribute to the fabrication process of CMOS image sensors to achieve high electrical performance.

Chapter 6

Hydrogen diffusion behavior in large thermal budget

6.1 Introduction

Previous chapter demonstrated the hydrogen diffusion behavior and the defects morphology at small thermal budget in the hydrocarbon-molecular-ion implanted region. In addition, the dissociation activation energy 0.76 eV of hydrogen out-diffused from the hydrocarbon-molecular-ion implanted region was estimated by reaction kinetic analysis. However, technical issues of CMOS image sensors, including dark current, image lag and random telegraph signal (RTS) noise, should be solved to achieve high electrical device performance [15, 24, 66, 92, 122–130]. The cause of dark current is the generation-recombination centers induced by deep energy level defects in a silicon bandgap owing to metallic impurities generated during various semiconductor fabrication processes [24,66,122–124]. Another source of dark current is the junction leakage current components attributable to the interface state defects at the SiO_2/Si interface in isolation regions such as the deep-trench isolation (DTI) region [15, 92, 127–129]. The image lag is caused by carriers trapped in potential pockets owing to oxygen out-diffusing from the Si substrate to a device active region [122, 123]. In addition, RTS noise is described as a fluctuation in the current of a MOSFET that is randomly generated by the trapping and emission of carriers in the MOSFET channel at the traps of silicon and gate oxide-silicon interface defects [130, 131]. In recent years, the reduction of dark current and RTS noise is particularly required for low-luminance imaging with CMOS image sensors in, for example, automotive applications [14, 132, 133]. Therefore, the reduction in the density of interface state defects at the SiO_2/Si interface in the isolation region or transistor gate oxide is necessary for improving the dark current and RTS noise characteristics of advance CMOS image sensors.

Thus, the gettering technology that can solve the above technical issues of CMOS image sensors must be developed. Previous chapter demonstrated that hydrogen is trapped in the implanted region of a hydrocarbon molecular ion after epitaxial growth [36]. This is an interesting diffusion behavior, because hydrogen after monomer ion implantation has been conventionally considered to out-diffuse owing to the high diffusion velocity of hydrogen in bulk silicon. Furthermore, the hydrogen in the implanted region of a hydrocarbon molecular ion is released depending on the subsequent annealing conditions. In addition, the molecular hydrogen diffusion from the hydrocarbon-molecular-ion implanted regions has been studied on the basis of the dissociation activation energy estimated by reaction kinetic analysis, as shown in above section. Conventionally, low-temperature molecular hydrogen forming gas annealing (FGA) after a CMOS device fabrication process electrically inactivates and reduces the density of interface state defects by hydrogen passivation to terminate the dangling bonds of silicon at the SiO_2/Si interfaces [89,90,129,130,136]. However, CMOS image sensors have been fabricated by forming multiple dielectric layers on the silicon surface by chemical vapor deposition or atomic layer deposition before low-temperature molecular hydrogen FGA [127, 128]. Thus, most of the molecular hydrogen are trapped in these multiple dielectric layers during the low-temperature molecular hydrogen FGA and they cannot diffuse into the active region of CMOS image sensors [127, 128]. Therefore, this molecular hydrogen diffusion behavior of the novel silicon epitaxial wafers can contribute to the effective reduction in the density of interface state defects at the SiO_2/Si interface. On the other hand, interface state defects are generated by the dangling bonds of silicon at the SiO_2/Si interface [89, 90, 129, 130, 136]. However, since the dissociation reaction of molecular hydrogen is necessary, two reactions, namely, $Si + H_2 \rightarrow Si + H + H$ and $Si + H + H \rightarrow Si - H + H$ are required in order to terminate a dangling bond of silicon at the SiO_2/Si interface [129]. In contrast, atomic hydrogen can terminate a dangling bond of silicon via the reaction $Si + H \rightarrow Si - H$. Actually, regarding the passivation effect of molecular and atomic hydrogen annealing for the reduction of interface state defects at the gate oxide-silicon of transistors, a previous study have shown that atomic hydrogen annealing is more effective than molecular hydrogen FGA [129]. Thus, atomic hydrogen also diffusing from the hydrocarbon-molecular-ion implanted regions indicates a more effective passivation effect, thereby reducing the density of interface state defects at the SiO_2/Si interface. Above section has shown the possibility of molecular hydrogen diffusion in the hydrocarbon-molecular-ion implanted regions. However, no hydrogen diffusion has been observed after a long high-temperature annealing. In addition, to the best of our knowledge, the possibility of atomic hydrogen diffusion has never been reported. Therefore, in this section, I investigated the hydrogen diffusion behavior

in the hydrocarbon-molecular-ion implanted regions after large thermal budget of a long high-temperature annealing. I found the possibility of both molecular and atomic hydrogen diffusing from the hydrocarbon-molecular-ion implanted regions. In this chapter, first, I describe the hydrogen diffusion behavior after a long high-temperature annealing. Then, I present two dissociation activation energies determined by reaction kinetic analysis using the results on the time dependence of hydrogen diffusion. Finally, I discuss the mechanism of molecular and atomic hydrogen diffusion on the basis of these dissociation activation energies estimated by reaction kinetic analysis. I believe that molecular and atomic hydrogen diffusion contributes to the high performance of CMOS image sensors by decreasing the photodiode junction leakage current and RTS noise.

6.2 Experiments and analysis methods

In this section, n-type Si (100) wafers were implanted with C_3H_5 at room temperature. The C_3H_5 doses were 1.6×10^{14} - 6.6×10^{14} molecular ions/cm^2. The C_3H_5 doses converted into the amounts of carbon were 5.0×10^{14} - 2.0×10^{15} atoms/cm^2 and those converted to the amounts of hydrogen were 8.3×10^{14} - 3.3×10^{15} atoms/cm^2. The implantation energy was 80 keV/molecular ion. The implantation energy of hydrogen was extremely low at 1.95 keV because the molecular ions distributed the implantation energy. The C_3H_5 beam current was 800 μA. The samples were epitaxially grown after molecular ion implantation. The epitaxial layer thickness was 5.0 μm. The epitaxial growth temperature and growth rate were approximately 1100°C and 1.0 μm/min, respectively. Furthermore, the samples were annealed from 600 to 1100°C for 5 to 360 min to evaluate the diffusion behavior of hydrogen in the C_3H_5-implanted region.

The distribution of hydrogen in the C_3H_5-implanted region was analyzed by secondary ion mass spectrometry (SIMS) using an IMS7f model from CAMECA, France. Cross-sectional transmission electron microscopy (XTEM) was used in order to observe the implantation defects in the C_3H_5-implanted region after epitaxial growth. Furthermore, the damage in the C_3H_5-implanted region was analyzed using a technology computer-aided design (TCAD) with the TCAD Sentaurus process simulator from Synopsys Inc. [51].

6.3 Hydrogen diffusion behavior in hydrocarbon-molecular-ion implanted regions after high-temperature annealing

Figure 6.1 shows the depth profiles of carbon and hydrogen obtained by SIMS analysis after (a) ion implantation and (b) 30 min annealing at 600°C at the C_3H_5 dose of 6.6×10^{14} molecular ions/cm^2. The hydrogen profile of C_3H_5 shows a narrow projected range near the Si wafer surface. At the implantation energy used in this study, the hydrogen implanted region was 40 nm in depth from the Si wafer surface. Then, after annealing at 600°C, the hydrogen peak concentration decreased owing to out-diffusion during annealing. Although the diffusion velocity of hydrogen is markedly high in a Si wafer, the hydrogen peak concentration was observed in the implanted region of C_3H_5 after annealing at 600°C. Above section study has shown that the implanted monomer hydrogen ions diffused, resulting in a hydrogen concentration that is below the detection limit of SIMS analysis upon annealing at 600°C. However, silicon epitaxial growth is performed using high-temperature processes ($>$ 1000°C). Therefore, I conducted SIMS analysis of the hydrogen concentration in the C_3H_5 implanted wafer after epitaxial growth.

Figure 6.2 shows the depth profiles of hydrogen after epitaxial growth at C_3H_5 doses of 1.6×10^{14} (dotted line) and 3.3×10^{14} (solid line) molecular ions/cm^2. A hydrogen peak was confirmed in the C_3H_5 implanted region. The hydrogen peak concentrations of 1.6×10^{14} (dotted line) and 3.3×10^{14} (solid line) molecular ions/cm^2 were 5.2×10^{17} and 1.2×10^{18} atoms/cm^3, respectively. The epitaxial growth was performed at a high temperature of 1100°C. However, hydrogen was observed in the implanted region of C_3H_5 after the epitaxial growth. Figure 6.3 shows the dependence of hydrogen peak concentration after epitaxial growth on the C_3H_5 dose. The hydrogen peak concentration increased linearly. Since the carbon concentration also increases depending on the C_3H_5 dose, I consider that carbon is related to the hydrogen trapping behavior.

I then evaluated the hydrogen diffusion behavior after the annealing of the C_3H_5 implanted epitaxial wafer. Figure 6.4 shows the SIMS profiles of hydrogen after epitaxial growth (solid line) and subsequent annealing for 30 min at 900°C (dashed line) and 1100°C (dotted line) at the C_3H_5 dose of 3.3×10^{14} molecular ions/cm^2. As shown in Figure 6.4, the hydrogen concentration decreased depending on the temperature. However, hydrogen remained in the C_3H_5 implanted region after the annealing at 1100°C. This unique hydrogen diffusion behavior has never been reported. The hydrogen diffusion velocity is extremely high in bulk silicon. I found that the hydrocarbon molecular ions in their implanted region exhibit a high

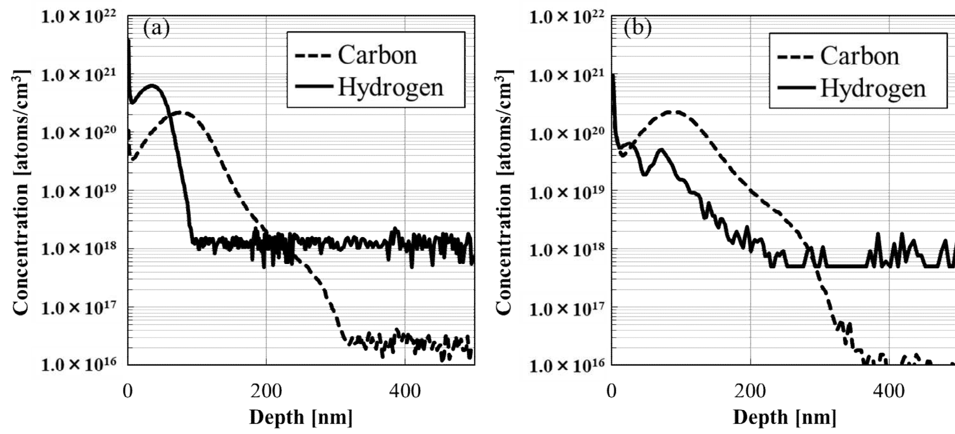

Figure 6.1: Depth profiles of carbon and hydrogen by SIMS analysis after (a) ion implantation and (b) 30 min annealing at 600°C at the C_3H_5 dose of 6.6×10^{14} cluster atoms/cm^2.

gettering capability for hydrogen.

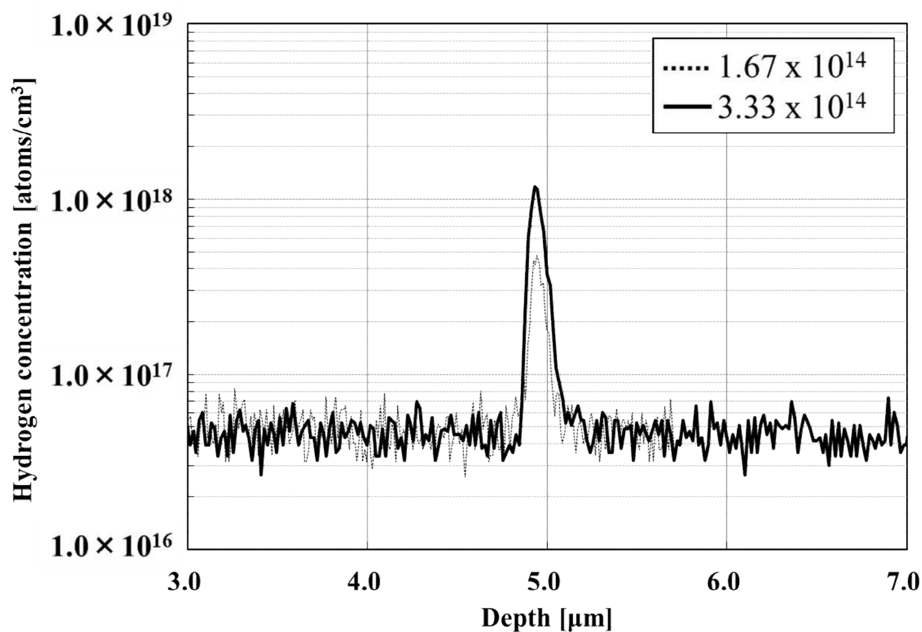

Figure 6.2: Depth profiles of hydrogen after epitaxial growth at C_3H_5 doses of 1.6×10^{14} (dotted line) and 3.3×10^{14} (solid line) cluster atoms/cm^2.

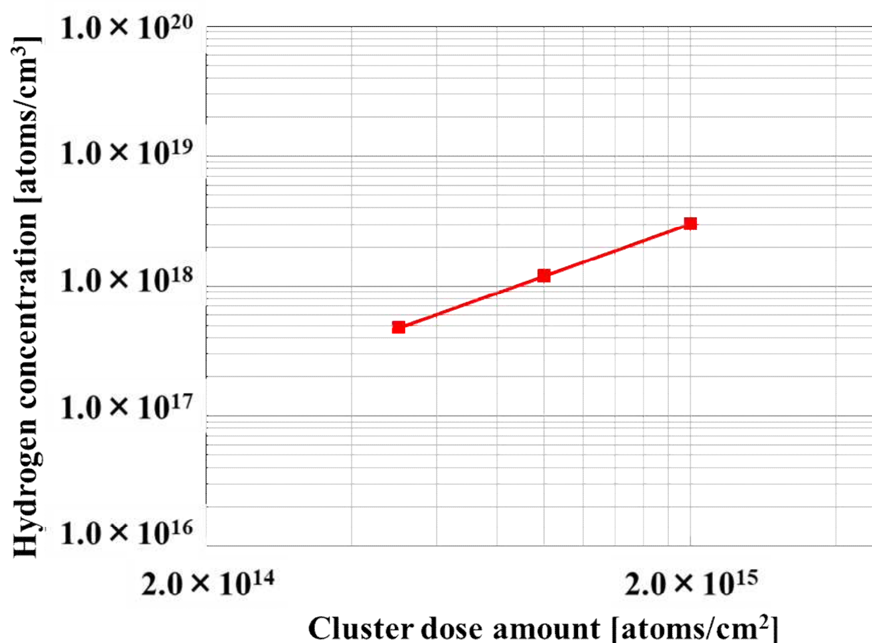

Figure 6.3: Dependence of hydrogen peak concentration after epitaxial growth on C_3H_5 dosage.

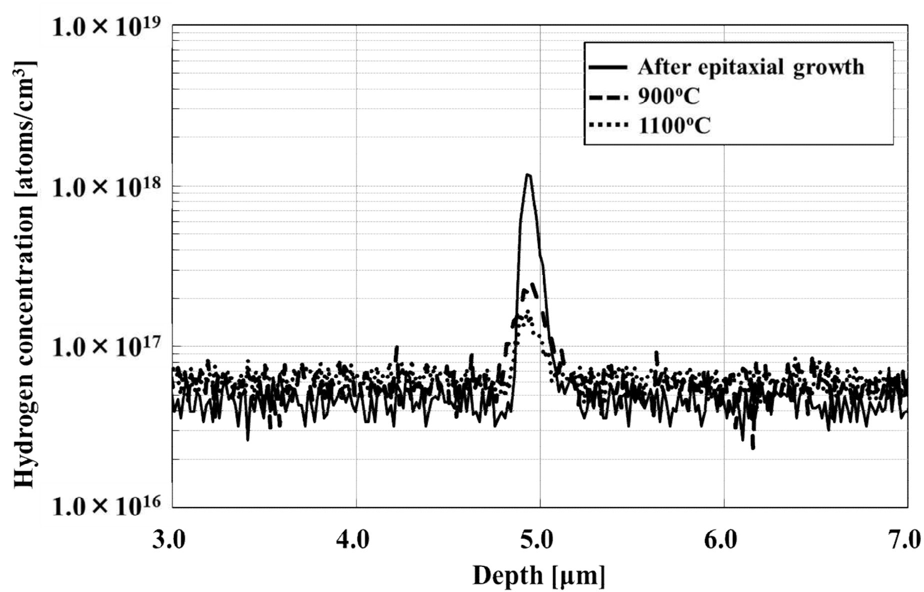

Figure 6.4: SIMS profiles of hydrogen peak after epitaxial growth (solid line) and subsequent annealing for 30 min at temperatures 900°C (dashed line) and 1100°C (dotted line) at C_3H_5 dose of 3.3×10^{14} cluster atoms/cm^2.

Figure 6.5 shows the density of hydrogen that out-diffused from C_3H_5 implanted region after the annealing. I calculated the out-diffused hydrogen density from the finite difference in integral values in a 1.0 μm region around the hydrogen peak concentration before and after the annealing from 600 to 1100°C for 30 min. The out-diffused hydrogen densities after annealing at 600 to 1100°C were approximately from 1.0×10^{12} to 1.0×10^{13} atoms/cm^2. It is known that the Si(100)/SiO_2 interface state defect density is approximately from 1.0×10^{10} to 1.0×10^{11} atoms/cm^2. From the results, the out-diffused hydrogen density was higher than the interface state density. I assumed that the out-diffused hydrogen density is sufficient for the passivation of interface state defects after a long high-temperature annealing. Then, the time dependence of hydrogen diffusion was analyzed after a long high-temperature annealing.

Figure 6.6 shows plots of hydrogen density in the C_3H_5 implanted region after the annealing at 800 to 1100°C with the annealing time on the horizontal axis and the logarithm of hydrogen concentration on the vertical axis. Hydrogen concentration decreased linearly. In addition, the result indicated a change in the slope at which the hydrogen density gradually decreased with annealing time from approximately 100 min. If the reduction resulting in hydrogen dissociation from the C_3H_5 implanted region is reversible reaction, the hydrogen density should reach equilibrium after a long time of annealing. However, the hydrogen density decreased linearly even after a long time of annealing. Hence, this result suggests that the dissociation of hydrogen involves two reactions in the C_3H_5 implanted region.

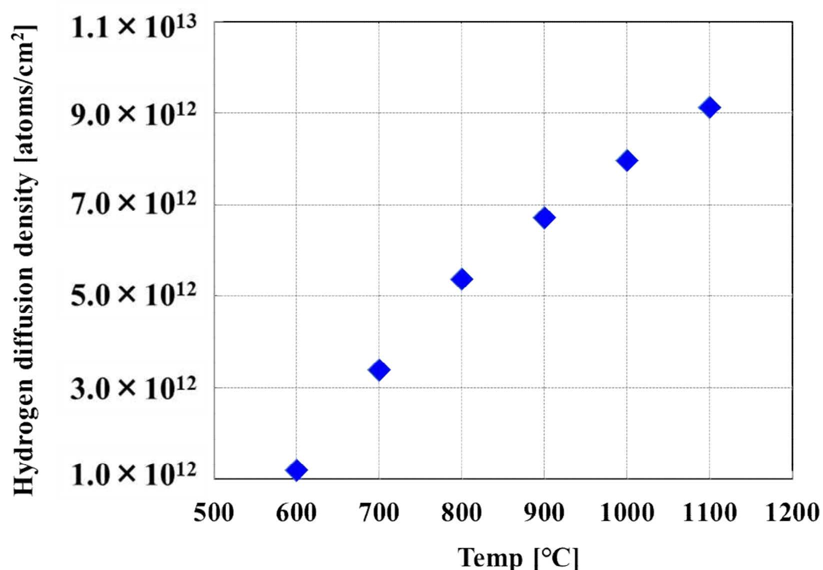

Figure 6.5: Plots of hydrogen density that out-diffused obtained by the finite difference in integral values in a 1.0 μm region around the hydrogen peak concentration before and after annealing from 600 to 1100°C for 30 min.

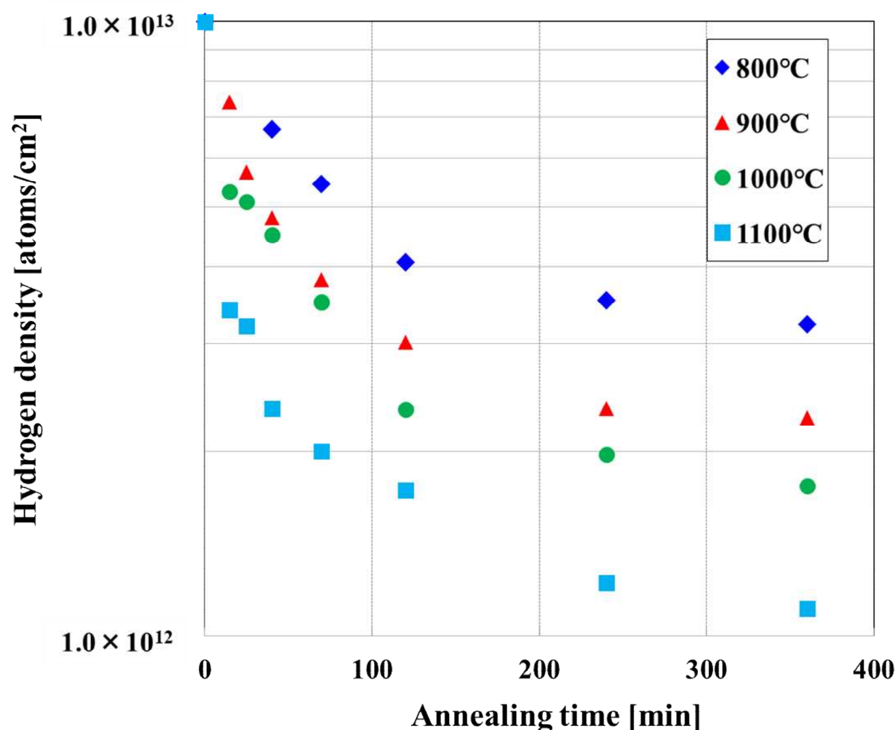

Figure 6.6: Plots of hydrogen density in C_3H_5 implanted region after heat treatments at 800 to 1100 °C with heat treatment time on the horizontal axis and logarithm of hydrogen density on the vertical axis.

6.4 Model of hydrogen diffusion by reaction kinetic analysis

I inferred that the implanted region of C_3H_5 is related to two hydrogen dissociation reactions, as shown in Figure 6.6. I assumed only a dissociation reaction, because the density of hydrogen did not reach equilibrium even after a long high-temperature annealing. Also, since the hydrogen diffusion velocity in bulk silicon is extremely high, the possibility of reversible reaction is low. Thus, I calculated the dissociation activation energy by reaction kinetic analysis assuming two dissociation reactions. The hydrogen dissociation reactions can be expressed as

$$H_1 \rightarrow \dot{H}_1, \tag{6.1}$$

$$H_2 \rightarrow \dot{H}_2. \tag{6.2}$$

It was assumed that the H_1 reaction occurred primarily during a short (<100 min) annealing and H_2 reaction occurred during a long (>100 min) annealing, as shown in Figure 6.6. Assuming that only reactions 6.1 and 6.2 are involved in the dissociation, the following reaction formula can be obtained:

$$\frac{dD_{Hn}}{dt} = -k_n D_{Hn} \ (n = 1 \ or \ 2), \tag{6.3}$$

$$D_{Hn} = D_{0n} exp(-k_n t) \ (n = 1 \ or \ 2), \tag{6.4}$$

where D_{0n} and D_{Hn} are the density of hydrogen trapped in the C_3H_5 implanted region before and after the annealing, respectively. The annealing time is t. The reaction rate constant is k_n. Thus, the hydrogen density is shown in Figure 6.6 as the sum of reactions 6.1 and 6.2. Consequently, assuming that the total hydrogen density is D_H and the initial concentration is D_0, the ratio of D_H to D_0 is expressed as

$$D_H = D_{H1} + D_{H2}, \tag{6.5}$$

$$\frac{D_H}{D_0} = \alpha exp(-k_1 t) + \beta exp(-k_2 t), \tag{6.6}$$

where α and β are the ratios of initial density for each annealing condition of H_1 and H_2, respectively. β was derived from the intercept of the slope for the long annealing and the vertical axis in Figure 6.6. Then, α was calculated as $1 - \beta$. The curve fitting of equation 6.6 and Figure 6.6 was performed using k_1 and k_2. Figure 6.7 shows the fitting results for the ratio of D_0 to D_H at 800 to 1100°C. The

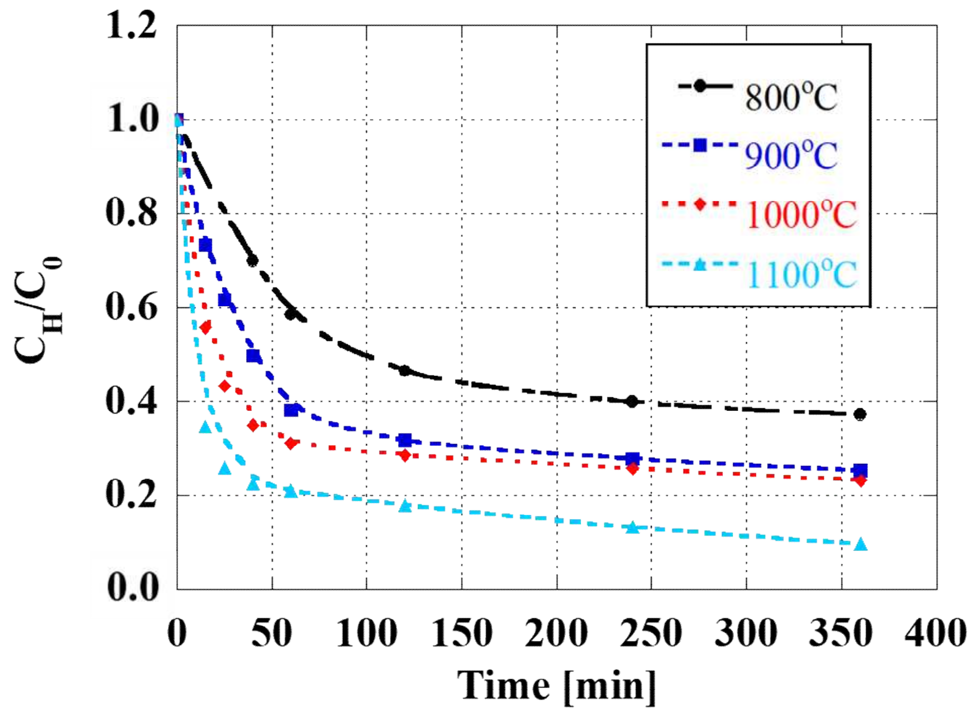

Figure 6.7: Fitting results for the ratio of D_0 to D_H at 800 to 1100°C.

reaction rate constants k at each annealing temperature can be obtained from the fitting results. Figure 6.8 shows the Arrhenius plots of the reaction rate constants of reactions 6.1 and 6.2. The dissociation activation energy was estimated to be 0.79 eV (reaction 6.1) and 0.42 eV (reaction 6.2) from the Figure 6.7. I discuss these dissociation activation energies and binding states of trapped hydrogen in the next section.

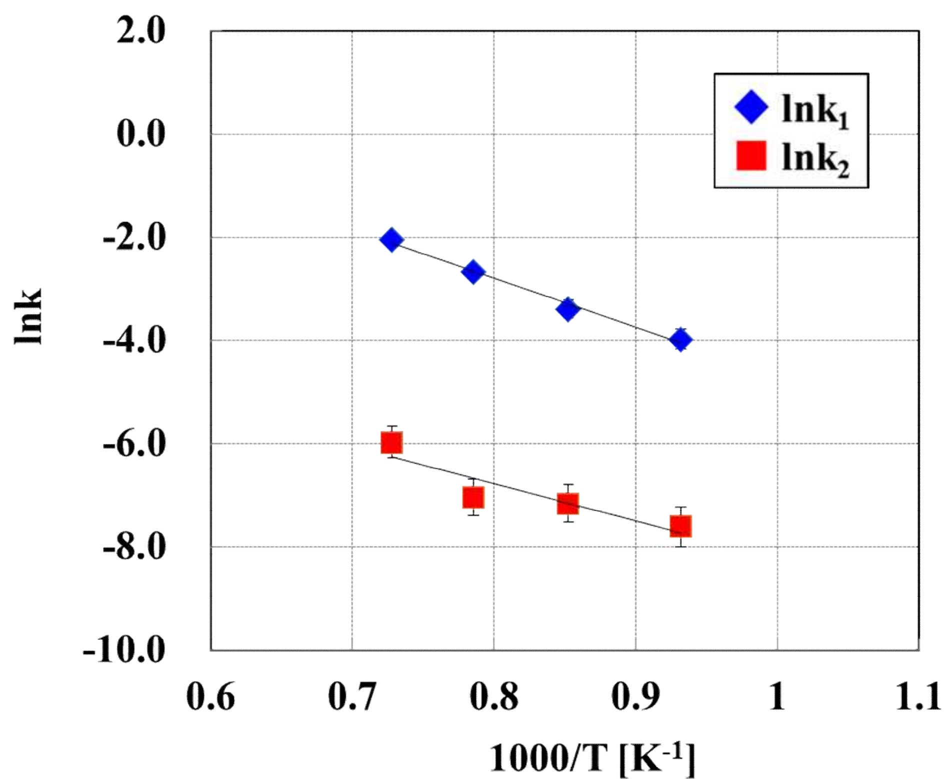

Figure 6.8: Arrhenius plots of the reaction rate constants k_1 and k_2 of reactions expressed in reactions 6.1 and 6.2.

6.5 Mechanism of hydrogen diffusion in implanted region

First, I considered the activation energy of 0.79 eV for reaction 6.1 (short time annealing). In the case of reaction 6.1, the dissociation activation energy of 0.79 eV is close to the diffusion activation energy of 0.78 eV of molecular hydrogen [63, 99, 100]. Markevich *et al.* reported that the activation energy for the diffusion of molecular hydrogen located at the T_d site is 0.78 eV [63]. Another possibility is a binding state in which hydrogen is trapped by the carbon impurities in the hydrocarbon-molecular-ion implanted regions. Hourahine et al reported that the energy of binding of a hydrogen molecule to a carbon impurity in a C-H_2 defect is 0.8 eV [62]. Therefore, the C-H_2 binding state and out-diffusion of molecular hydrogen are indicated by the dissociation activation energy for reaction 6.1. However, previous studies investigated the hydrogen diffusion behavior after low-temperature annealing up to 400°C. In this study, hydrogen was trapped in the implanted region of C_3H_5 after high-temperature annealing. Thus, it is considered that the trapping sites where molecular hydrogen dissociates during high temperature annealing are different from a simple C-H_2 binding state. Therefore, I speculated that the carbon complexes contribute to the trapping of hydrogen in the hydrocarbon-molecular-ion implanted regions. Pinacho *et al.* demonstrated that carbon and silicon self-interstitial complexes (CI clusters) are formed in carbon-rich silicon with regard to the behavior of carbon complexes in bulk silicon [61]. I inferred that CI clusters are formed in the implanted region of a hydrocarbon molecular ion because the hydrocarbon-molecular-ion implanted regions is extremely narrow at high concentrations of carbon, as shown in Figure 6.1. Furthermore, carbon profiles were evaluated by SIMS analysis after epitaxial growth in order to confirm carbon and hydrogen peak depths.

Figure 6.9 shows the carbon and hydrogen profiles after epitaxial growth at a C_3H_5 dose of 1.6×10^{14} molecular ions/cm^2 obtained by SIMS analysis. I found that hydrogen was trapped in the region of the carbon peak concentration. The sharp peak region was observed in the carbon profile. In addition, the carbon profile was distributed in the 1.0 μm region around the peak region. Hydrogen was trapped in the carbon sharp peak region but not around the peak region. To further evaluate this carbon profile, I actually simulate a C_3H_5-implanted epitaxial wafer by TCAD using the TCAD Sentaurus process simulator from Synopsys Inc. [51]. The simulator has the model for the formation of CI clusters (C_xI_y) [52]. This cluster model is described a complex of carbon and Si self-interstitials in the formation of C_xI_y. Therefore, I simulated the C_3H_5 ion implantation and silicon epitaxial

growth processes by using TCAD Sentaurus process to analyze the formation of CI clusters. Figure 6.10 shows the profiles of total carbon (dotted line), C_3I_3 clusters (solid line) and carbon interstitials (C_i) (dashed line) after epitaxial growth at a C_3H_5 dose of 1.6×10^{14} atoms/cm^2 by TCAD simulation. Silicon epitaxial layers of 4.0 μm thickness were grown at 1100°C. The results indicate that the peak of carbon concentration in the C_3H_5-implanted region is mainly attributable to by C_3I_3 clusters. The C_3I_3 cluster size is maximum for the current TCAD model [51]. On the other hand, Fukata *et al.* demonstrated that voids or platelet defects form complexes and binding states with hydrogen in carbon-doped silicon after hydrogen atomic treatment [113–115, 137]. Thus, it is observed by high-resolution cross-sectional transmission electron microscopy (HR-XTEM) that voids or platelet defects were formed in the implanted region of C_3H_5.

Figure 6.11 shows a (a) low-magnification XTEM image and an (b) HR-XTEM image of an epitaxially grown sample. C_3H_5 implantation defects are observed in the implanted region of C_3H_5 in Figure 6.11 (a). A defect of approximately 5 nm was found to be formed in the implanted region of C_3H_5, as shown Figure 6.11 (b). As a result, no voids or platelet defects were observed in the implanted region of C_3H_5. Thus, hydrogen in the implanted region of C_3H_5 was not in the binding state trapped by voids and platelet defects. In addition, I simulated the hydrocarbon molecular ion implantation and the silicon epitaxial growth process using the kinetic Monte Carlo (KMC) code in the TCAD Sentaurus process simulator from Synopsys Inc. in order to confirm the formation of CI clusters [62]. Figure 6.12 shows an (a) HR-XTEM image of the C_3H_5 implanted region and the (b) KMC simulation result of CI clusters. The distribution of carbon (black) and Si self-interstitials (red) is shown in Figure 6.12 (b). Consequently, it is speculated that 5 nm defects may be CI clusters. It is inferred that the CI clusters contribute to the trapping of molecular hydrogen.

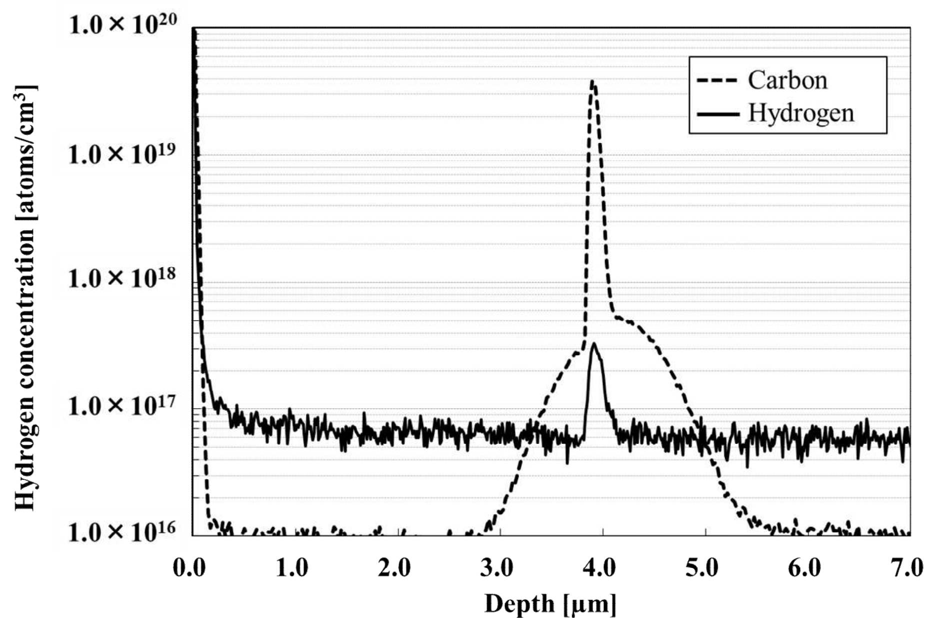

Figure 6.9: Carbon and hydrogen profiles after epitaxial growth at C_3H_5 dose of 1.6×10^{14} atoms/cm^2 obtained by SIMS analysis.

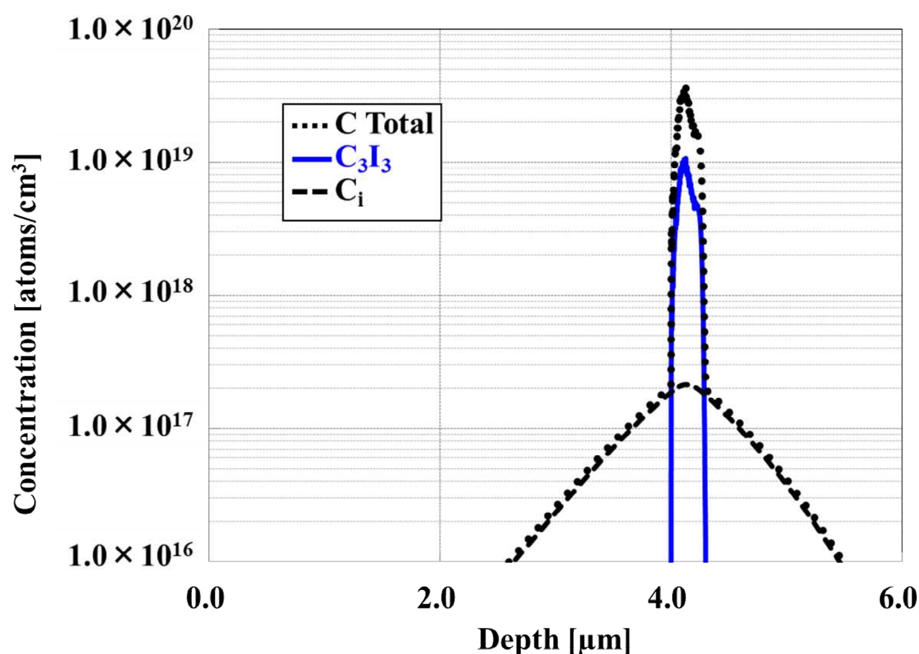

Figure 6.10: Profiles of total carbon (dotted line), C_3I_3 clusters (solid line) and carbon interstitials (C_i) (dashed line) after epitaxial growth at C_3H_5 dose of 1.6×10^{14} atoms/cm^2 obtained by TCAD simulation.

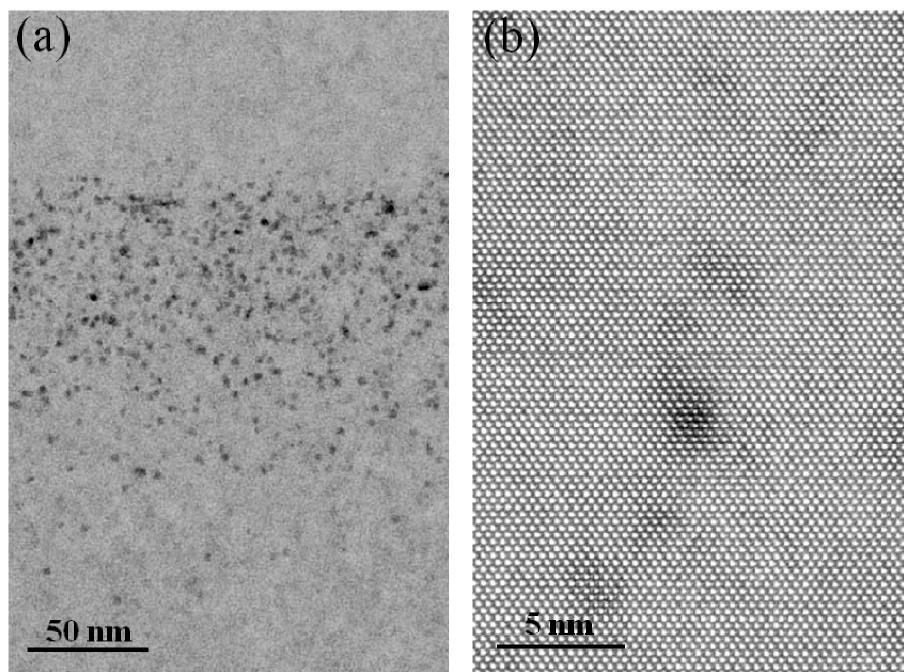

Figure 6.11: (a) low-magnification XTEM image and (b) HR-XTEM image of epitaxially grown sample.

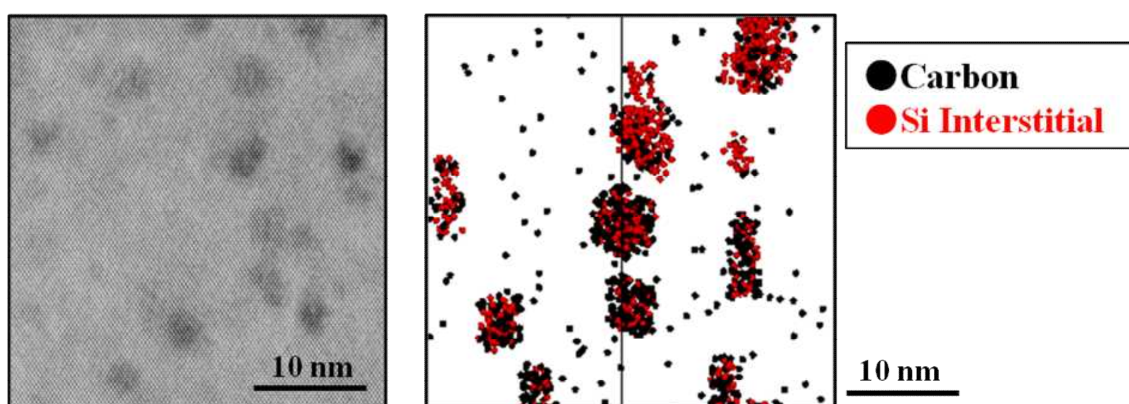

Figure 6.12: HR-XTEM image of C_3H_5 implanted region and (b) KMC simulation result of CI clusters.

I now discuss the activation energy of 0.42 eV for reaction 6.2 (long time annealing). This activation energy is close to the commonly reported atomic hydrogen diffusion activation energy of 0.48 eV [89,90]. Therefore, the out-diffusion of atomic hydrogen is suggested by the dissociation activation energy for reaction 6.2. However, the binding state of the atomic hydrogen trapped in the implanted region of C_3H_5 is unclear.

One possibility is a binding state in which atomic hydrogen is trapped by vacancy-related complexes in the hydrocarbon-molecular-ion implanted regions. Previous studies indicated that hydrogen in complexes with vacancies (*e.g.*, VH_4) dissociated after annealing at 600°C [113–115, 137]. In the case of hydrocarbon molecular ion implantation, vacancies and interstitial silicon are generated during molecular ion implantation. Since interstitial silicon forms a CI clusters with carbon, it is presumed that the vacancies and hydrogen-related complexes are formed in the hydrocarbon-molecular-ion implanted regions. Thus, it is considered that atomic hydrogen out-diffuses from the vacancy-related complexes.

Other possibility is considered that oxygen trapped in the implanted region of C_3H_5 may be bonded to hydrogen. The binding energy of oxygen and hydrogen (O-H) in bulk silicon is reported to be 0.47 eV [137]. Previous studies have shown that the implanted region of C_3H_5 also trapped oxygen. Figure 6.13 shows depth profiles of carbon, oxygen and hydrogen obtained by SIMS analysis after epitaxial growth. Furthermore, Onaka-Masada reported that the 5 nm defects observed by HR-XTEM is a carbon aggregate and oxygen is trapped inside the 5 nm defects. Consequently, it is considered that atomic hydrogen diffused after a long annealing because oxygen and hydrogen are bonded inside the 5 nm defects. Therefore, it is inferred that atomic hydrogen was released during a long high-temperature annealing. Finally, these results suggest that hydrogen in the C_3H_5 implanted region out-diffuses as molecular and atomic hydrogen. Therefore, molecular and atomic hydrogen diffusing from the C_3H_5 implanted region can effectively passivate interface state defects at the SiO_2/Si interface.

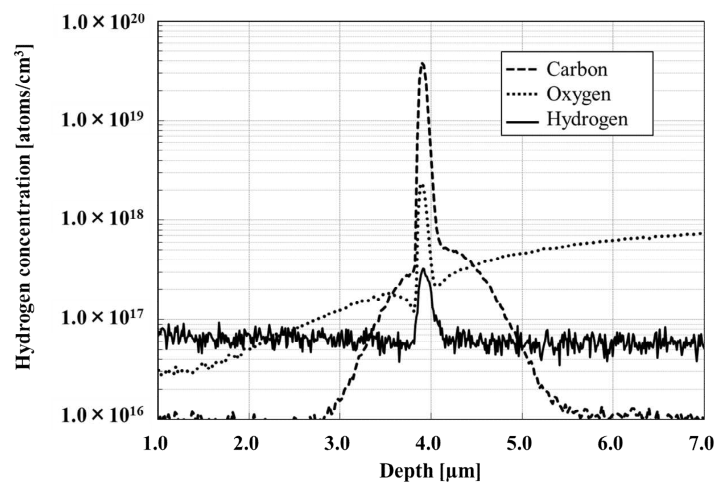

Figure 6.13: Depth profiles of carbon, oxygen and hydrogen by SIMS analysis after epitaxial growth.

6.6 Summary

I demonstrated the hydrogen diffusion behavior in the C_3H_5 implanted region. First, hydrogen was observed after epitaxial growth. The hydrogen peak concentration increased depending on the dose of C_3H_5 after epitaxial growth, but decreased depending on temperature after annealing. The out-diffused hydrogen density from 600 to 1100°C was approximately in the range from 1.0×10^{12} to 9.0×10^{12} atoms/cm^2. I assumed that this out-diffused hydrogen density range is sufficient for the passivation of interface state defects. I also derived the dissociation activation energy assuming two dissociation reactions. The activation energies of hydrogen dissociation from the implanted region were calculated to be 0.79 and 0.42 eV. This result suggests the possibility of molecular and atomic hydrogen diffusion from the C_3H_5 implanted region. I conclude that hydrogen diffusion in the implanted region of a hydrocarbon molecular ion can contribute to the high electrical performance characteristics of CMOS image sensors.

Chapter 7

Termination effect of hydrocarbon molecular ion implanted silicon wafers

7.1 Introduction

As shown in previous sections, CMOS image sensor has been widely used ubiquitous devices such as smart-phone and smart-watch. Consumer market strongly demand more high sensitivity and more high speed image data processing for achieving fabricate high performance CMOS image sensors [24, 66, 122, 124–126]. However, there are some serious technical issues for achieving fabricates high performance CMOS image sensor manufacturing. Very important issue is dark current noise, fix pattern noise and random telegraph noise generation from CMOS image sensor circuits. It is well known that these noise origins are the transfer gate oxide at SiO_2/Si interface states, local oxidation of silicon (LOCOS), shallow trench isolation (STI) and deep trench isolation (DTI) interface states defects [128–130]. The interface defects forms deep energy level in the silicon band-gap which can act as generation-recombination (G-R) center. The G-R center strongly affects electrical device performance of CMOS image sensor. Therefore, CMOS image sensor manufacturer efforts reduction of various sensor circuit noises using optimum circuit design and device fabrication process. In the past, some circuit design researchers proposed new circuit design concept for reduction of noise from CMOS image sensor circuit [132, 138]. As a result, it is not enough to improvement of noise reduction performance. Other solution is low temperature hydrogen annealing after back end of line (BEOL) [89, 130, 136]. I call them forming gas annealing (FGA) treatment. FGA process is able to passivation of interface state defect by diffusing hydrogen. However, recently year, multi-film deposition process has been

widely by BEOL process using atomic layer deposition (ALD). Hydrogen does not reach the interface state region for as acting diffusion barrier effect of multi-film during the FGA process. In addition, the DTI structure to reduce in crosstalk has increased the hydrogen consumption required for the reduction of interface state density. Therefore, there is concern that the hydrogen termination effect may be reduced. Consequently, it is essential to perform FGA treatment before BEOL process. However, desorption of hydrogen from the SiO_2/Si interface may occur due to low temperature annealing during the BEOL process. FGA treatment is not effective solution for above the technical issue.

Other previous studies has reported the reduction of interface state density (D_{it}) at the SiO_2/Si interface by forming a SiO_2 layer after hydrogen ion implantation [139, 140]. However, since the high temperature annealing is repeatedly performed during the device process after the formation of SiO_2 layer, there is a concern that the interface state increases when hydrogen at the SiO_2/Si interface is released again during the high temperature annealing. In addition, the diffusion rate of hydrogen is known to be large in silicon wafers, and hydrogen does not remain in the silicon wafer after annealing. It is necessary to repeat the step of implanting hydrogen ions, which increases the device fabrication cost. Thus, the reduction of D_{it} using hydrogen ion implantation is difficult to apply to device process. Therefore, previous studies have developed alternative solution for technical issue of CMOS image sensor fabrication using hydrocarbon molecular ion implantation [30–36,134,135]. I demonstrated that hydrocarbon molecular ion implanted silicon wafer has high gettering capability for metallic impurity contamination during the CMOS image sensor fabrication process. I also found that the novel silicon wafer has three unique silicon wafer characteristics such as high gettering capability for metallic impurity, oxygen out-diffusion barrier effect and hydrogen storage effect of hydrocarbon implanted region. I have already reported our novel silicon wafer is dramatically improvement of CMOS device key parameter such as dark current and white spot defect using CMOS image sensor manufacturing line [31]. Above sections demonstrated that the diffusion reaction kinetic of hydrogen from hydrocarbon ion implanted region after isochronal annealing. However, they do not clearly show that hydrogen passivation mechanism of SiO_2/Si interface after isochronal annealing. Therefore, in this section, I focus on hydrogen passivation mechanism of SiO_2/Si interface state after isochronal annealing analyzed by capacitance-voltage measurement (C-V) and electron spin resonance (ESR) using MOS capacitance device structure.

7.2 Experiments

Figure 7.1 shows schematic of sample flow and structure. A p-type (100) wafer with a resistivity 10 ohm-cm was implanted with C_3H_5 as hydrocarbon molecular ion at room temperature. The C_3H_5 implantation dose and energy were 3.3×10^{14} molecular ion/cm^2 and 80 keV, respectively. Then, a p-type epitaxial silicon layers were grown with a resistivity 10 ohm-cm after C_3H_5 implantation. The epitaxial layer thickness was 5 μm. Also, the same p-type epitaxial wafers without C_3H_5 implantation were prepared in order to compare the passivation effect. The 25-nm SiO_2 layers were thermally grown in dry oxygen at 900°C for 100 min. Then, the samples were irradiated into electron beam with 800 keV and 2.0 MGy due to increase of interface state density at interface of SiO_2 and silicon. The samples irradiated by electron beam were isochronal annealed at 500, 600, 700, 800 and 900°C for 10, 30, 60 and 120 min in a nitrogen atmosphere. In addition, MOS structure formed by deposition of Al contacts with thickness 100 nm onto the oxide surface by electron beam evaporation using a mechanical mask for C-V measurement. Al electrode area square was 6.4×10^{-3} cm^2. Post-metallization annealing was carried out at 400°C for 30min. The D_{it} at interface of SiO_2 and silicon was measured using the standard quasi-static technique [54, 55]. ESR analyzed the samples without Al electrodes and derived the density of Pb center [56–59].

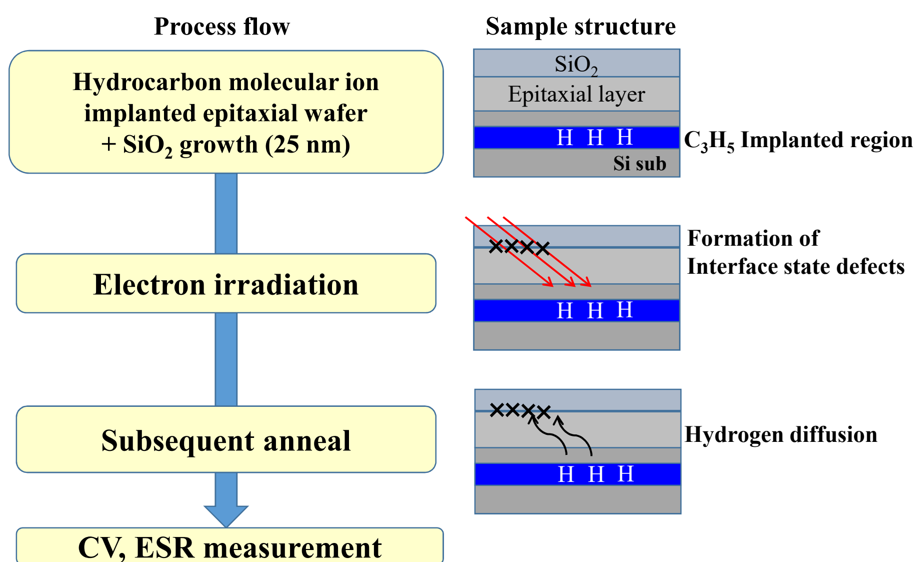

Figure 7.1: Schematic of sample flow and structure.

7.3 Hydrogen termination effect of hydrocarbon molecular ion implanted wafer

Figure 7.2 shows the results of C-V curve with theoretic calculation (black dotted line) and quasi static C-V measurement with the no annealed samples without C_3H_5 (blue dashed line) and with C_3H_5 (red solid line). The theoretical C-V curve and the measurement C-V curve with and without C_3H_5 were found to be different in Figure 7.2. These results indicate that D_{it} can be calculated using standard quasi static method [54, 55].

Figure 7.3 shows the calculation results of D_{it} without C_3H_5 (black circle) and with C_3H_5 samples (blue square) after 700°C annealing. The D_{it} at midgap of C_3H_5 implanted wafer was lower than that without C_3H_5 after 700°C annealing. Previous study demonstrated that the D_{it} of hydrogen FGA sample increases with annealing above 600°C because hydrogen desorbed from a SiO_2/Si interface during high temperature annealing [129]. However, the D_{it} with C_3H_5 decreased after 700°C annealing. The result demonstrated that the D_{it} with C_3H_5 implanted wafer may be decreased by the hydrogen diffused from the C_3H_5-implanted region after high temperature annealing. Then, the dependency of D_{it} on annealing temperature was analyzed by quasi static C-V method.

Figure 7.4 shows the D_{it} at midgap with annealing temperature in without C_3H_5 and with C_3H_5 implanted wafer. The D_{it} without C_3H_5 wafer decreased once after 500°C annealing, but increased after 900°C annealing. On the other hand, the D_{it} with C_3H_5 decreased depending on the annealing temperature. Previous study has reported that the density of hydrogen dissociation from the C_3H_5-implanted region increases depending on the annealing temperature. Thus, the D_{it} with C_3H_5 after 900°C annealing decreased than that after 500°C annealing. I consider that the density of hydrogen dissociated from the C_3H_5-implanted region was higher than the increase in the interface state density during 900°C annealing. Consequently, the reduction of D_{it} after 900°C annealing is considered to be the passivation effect of C_3H_5 implanted epitaxial silicon wafer.

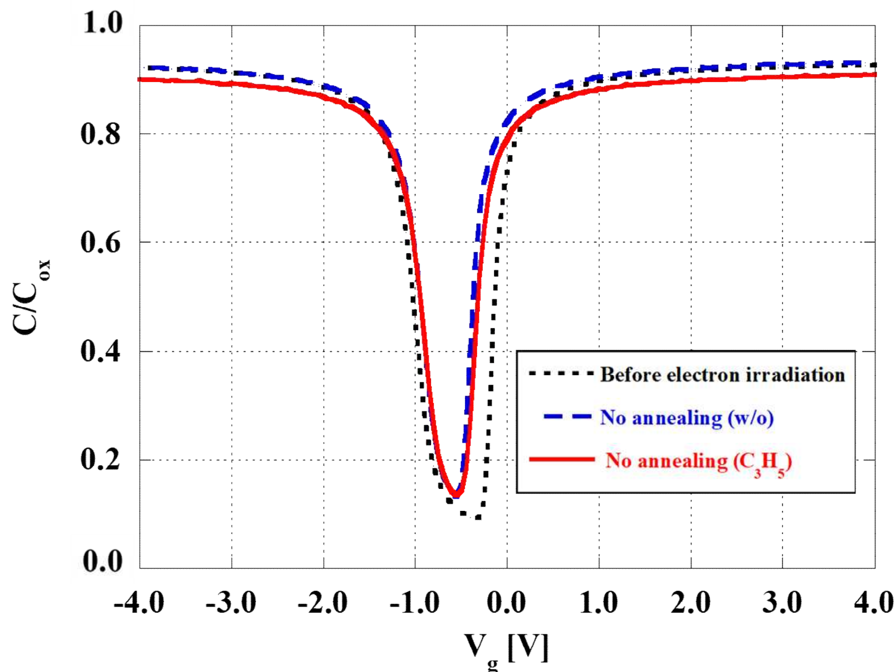

Figure 7.2: C-V curve of theoretic calculation (black dotted line) and quasi static C-V measurement with the unannealed samples without C_3H_5 (blue dashed line) and with C_3H_5 (red solid line).

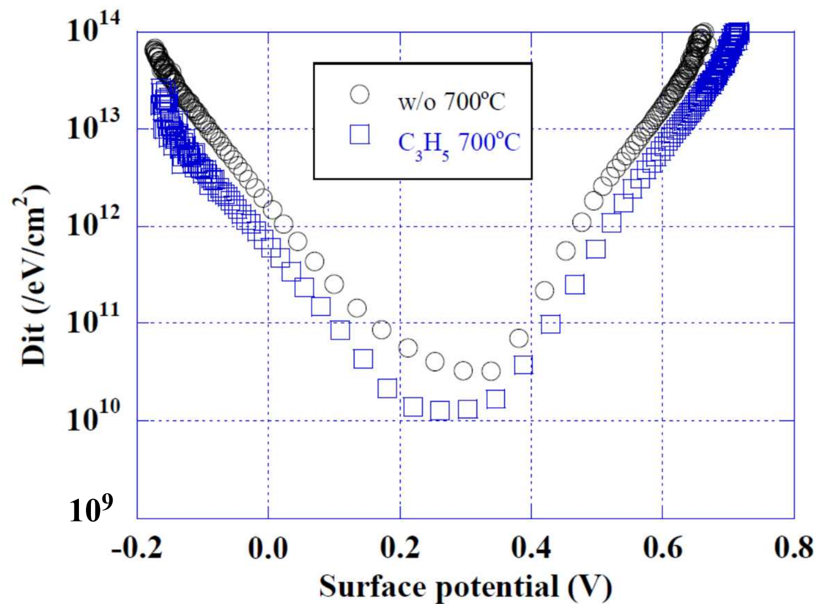

Figure 7.3: D_{it} without C_3H_5 (black circle) and with C_3H_5 samples (blue square) after 700°C annealing.

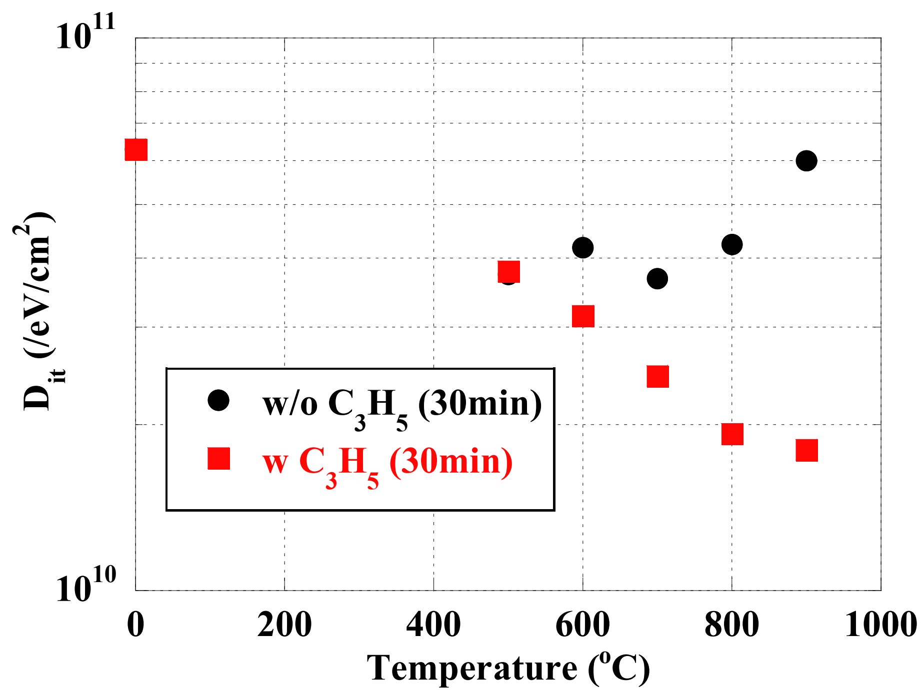

Figure 7.4: D_{it} at midgap with annealing temperature in without and with C_3H_5 implanted wafer.

Then, I analyzed the C-V measurement samples by ESR in order to identify the defects at SiO_2/Si interface related the reduction of D_{it}. ESR can analyze Pb centers known as interface state defects [56–58]. Most ESR studies of SiO_2 and silicon interface have dealt with the Pb center defects [58, 59]. In this section, one of the Pb center signal was observed as the Pb_0 center near the g value 2.0060-2.0062 for each annealed samples. Figure 7.5 shows ESR spectrum with C_3H_5 after annealing at 500°C for 30 min. In this study, electron beam irradiation was performed in order to increase the D_{it} to clarify the passivation effect of C_3H_5 implanted epitaxial wafer. There was a possibility that defects were also formed in the silicon bulk by electron beam irradiation. However, the ESR results showed a signal with a g value of 1.9996 due to hydrofluoric acid treatment and a signal with a g value of 2.0060 due to the Pb_0 center. The dangling bond densities in the silicon bulk were compared by ESR spectra with and without C_3H_5 implantation after removing all SiO_2, but no difference was observed after each annealing condition. Therefore, it is considered that dangling bonds in the silicon bulk formed by electron beam irradiation do not affect the C-V measurement results.

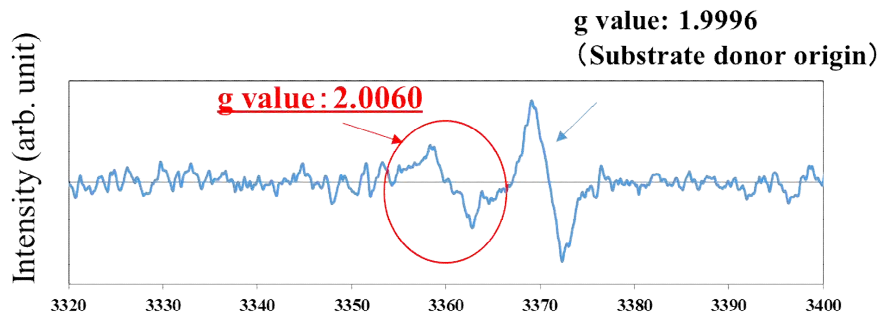

Figure 7.5: ESR spectrum with C_3H_5 after annealing at 500°C for 30 min.

It is known that the Pb_0 center has a structure in which all three bonds of silicon are silicon, and is represented by ·Si-Si_3 [142]. In addition, in order to verify the relation between the interface state and the Pb_0 center, I have plotted in Figure 7.6 D_{it} vs density of Pb_0 center each annealing temperature. The result indicate the density of Pb_0 center by ESR measurement is proportional to the D_{it} obtained by C-V measurement.

Consequently, it was revealed that D_{it} and Pb_0 center increased by electron beam irradiation can be reduced by using a C_3H_5 implanted epitaxial wafer. Figure 7.6 shows that the D_{it} without C_3H_5 is also proportional with the density of Pb_0 center. Then, I discuss the increase or decrease in D_{it} and Pb_0 center without C_3H_5 and with C_3H_5 after isochronal annealing. Firstly, I consider the change of D_{it} without C_3H_5. The decrease in D_{it} without C_3H_5 once at 500°C may be a passivation effect due to the nitrogen atmosphere. Previous studies have reported that D_{it} decreases

in a nitrogen atmosphere at 500°C [143]. However, it has been reported that the D_{it} after hydrogen FGA is lower than that after nitrogen atmosphere anneal. The increase in D_{it} without C_3H_5 at 900°C can be explained by two possibilities.

One is the interface state defects generation due to Si-O bond breaking by annealing and by the compressive stress [144]. Another is the dissociation of hydrogen or nitrogen in the SiO_2/Si interface during annealing [143]. On the other hands, the D_{it} of C_3H_5 implanted wafer decreased depending on annealing temperature. The results suggest that the hydrogen diffused from C_3H_5-implanted region can terminate to dangling bonds of silicon at SiO_2/Si interface during annealing at 900°C. Probably, the hydrogen terminated to interface state defects should also desorb from the SiO_2 and silicon interface of the C_3H_5 wafer. However, it is considered that hydrogen density out-diffused from the C_3H_5-implanted region more than dissociated hydrogen density during 900°C annealing. In fact, previous sections demonstrated the hydrogen density out-diffused from the C_3H_5-implanted region at 900°C is sufficient compared to the interface state density of SiO_2 and silicon. I analyzed the same condition samples that measured C-V characteristics by ESR in order to explore the interface state defects at SiO_2 and silicon interface in this study. Figure 7.6 shows that the Pb center density by ESR measurement is proportional to the D_{it} obtained by C-V measurement. Therefore, I consider that the D_{it} obtained by C-V measurement was reduced by terminating the Si dangling bond (·Si-Si_3) at the interface of SiO_2 and silicon with hydrogen diffused from C_3H_5-implanted region. This result can be explained when the hydrogen diffused from the C_3H_5-implanted region terminates the dangling bond at the interface of SiO_2 and silicon. Then, I consider how the diffused hydrogen terminated the dangling bonds. Previous study have shown that two types of molecular and atomic hydrogen are desorbed from the C_3H_5-implanted region. In this study, the SiO_2 film was formed at 900°C for 100 min, and then the sample irradiated with electron beam was annealed at 500 and 700°C for 30min. Previous study has been reported that molecular hydrogen is first desorbed from the C_3H_5-implanted region [135]. In addition, it has been demonstrated that atomic hydrogen diffuse remarkably by annealing at a temperature higher than 800°C. For this reason, the molecular hydrogen diffusion was dominant during subsequent annealing at 500 and 700°C.

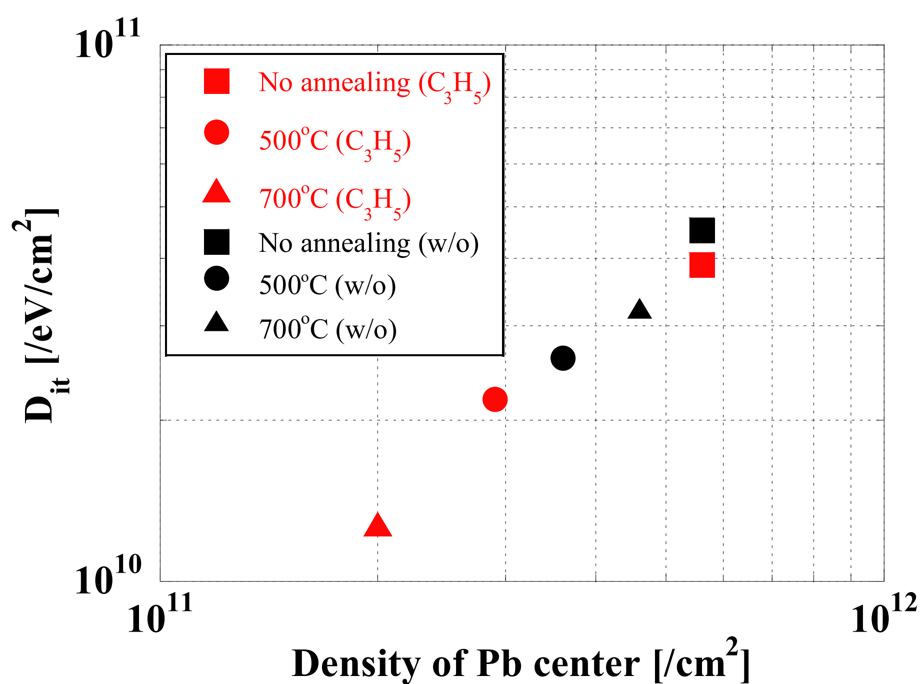

Figure 7.6: D_{it} vs density of Pb_0 center each annealing temperature in without and with C_3H_5.

7.4 Mechanism of hydrogen termination effect of hydrocarbon molecular ion

Then, in order to analyze the mechanism of the hydrogen passivation effect of the hydrocarbon-molecular-ion implanted wafer, the reaction at the SiO_2/Si interface was considered by analyzing with D_{it} decreasing with respect to the annealing time. Therefore, the dependence of D_{it} of wafers with C_3H_5 on the annealing time for each annealing temperature was evaluated using quasi-static C-V measurement. Figure 7.7 shows D_{it} at the midgap of wafer with C_3H_5 implantation after 500, 600, 700, 800 and 900°C annealing. D_{it} of the wafer with C_3H_5 implantation decreased with increasing annealing temperature and time. In the high-temperature annealing, D_{it} decreased significantly in a short time. Previous studies have reported the effect of hydrogen passivation by hydrogen FGA below 500°C [143]. It has never been reported that the time-dependent decrease in D_{it} during higher annealing at 500°C, as shown in this study. This is a unique D_{it} reduction behavior that has never been seen in the previous study. Understanding the mechanism of D_{it} reduction due to the hydrogen passivation effect of hydrocarbon-molecular-ion implanted wafers is also an important factor for the application of CMOS image sensors to device processing.

Therefore, I analyzed using the reaction kinetic analysis assuming a reaction model in order to analyze the mechanism of D_{it} reduction by using a hydrocarbon ion implanted wafer. The reaction equation for the time change of D_{it} obtained from the assumed reaction model was derived, and fitted with the experimental results for the annealing time dependence of D_{it}. Furthermore, the activation energy during hydrogen passivation at the SiO_2/Si interface was derived by obtaining the reaction rate constant of the assumed reaction model from the fitting results. A reaction model of the hydrogen passivation effect at the SiO_2/Si interface was considered. The reaction between hydrogen and a silicon dangling bond at the SiO_2/Si interface is expressed by the following equation 7.1. This is a reaction model in which hydrogen bonds to silicon dangling bonds (·Si) to form Si-H. The reaction equation obtained from equation 7.1 is shown in equation 7.2.

$$Si \cdot + H \rightarrow Si - H, \tag{7.1}$$

$$\frac{dSi\cdot}{dt} = -L_1[Si\cdot][H]. \tag{7.2}$$

$[Si\cdot]$ corresponds to the interface state density (D_{it}) obtained in the experiment. In the past, Reed *et al.* reported a model that considered the reaction related

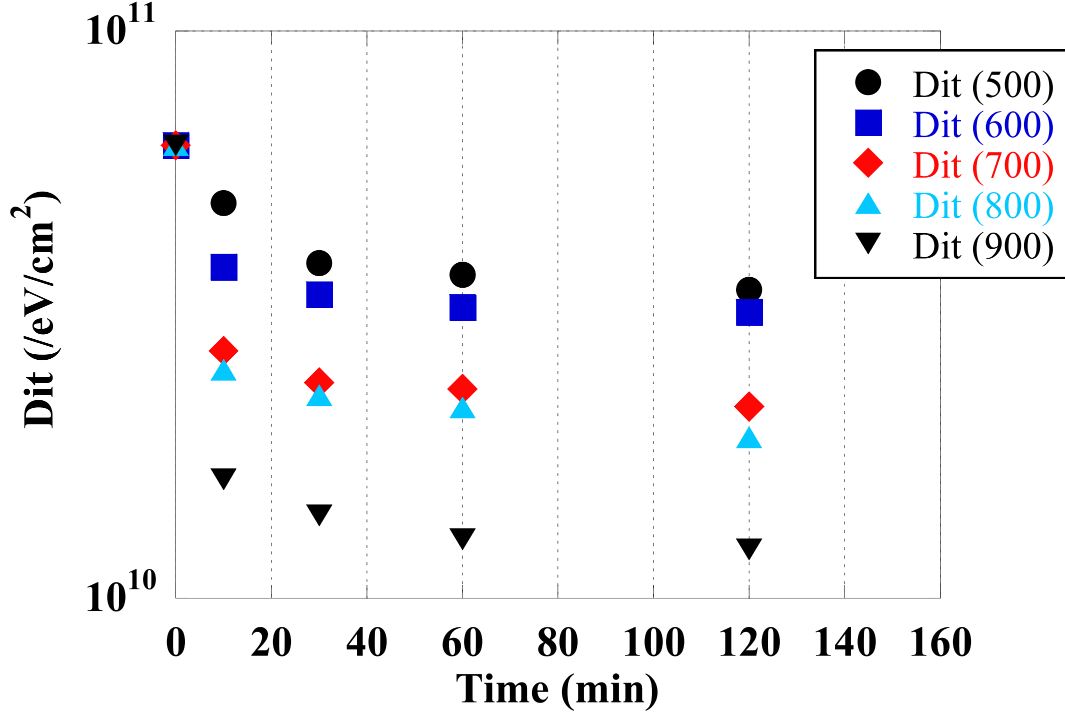

Figure 7.7: D_{it} at the midgap of wafer with C_3H_5 implantation after 500, 600, 700, 800 and 900°C annealing.

to hydrogen during hydrogen passivation of D_{it} as a two reaction model when considering the reaction model at the interface during hydrogen FGA at low temperature [143]. The reaction model and reaction equation are as shown in the following equations 7.3 and 7.4.

$$2H \rightarrow H_2, \tag{7.3}$$

$$\frac{d[H]}{dt} = -2L_2[H]^2. \tag{7.4}$$

This reaction model is derived from experimental results on hydrogen passivation at low temperatures. However, in order to consider the hydrogen passivation mechanism at the interface during the high temperature annealing, the following equation 7.5 was derived from the above reaction expressed by equations 7.1 and 7.2.

$$[Si\cdot] = \frac{[Si\cdot]_0}{(1 + 2L_2[H]_0 t)^{\frac{L_1}{2L_2}}}. \tag{7.5}$$

L_1 and L_2 are the reaction rate constants of reaction models 7.1 and 7.3. t is the annealing time. $[Si]_0$ is the initial density of D_{it}, and $[H]_0$ is the initial concentration of hydrogen out-diffused from the C_3H_5-implanted region. In addition, $[H]_0$ is expressed by the desorption activation energy and the initial hydrogen concentration

in the C_3H_5-implanted region as follows:

$$[H]_0 = 1.02 \times 10^{18} exp(\frac{-0.78}{k_B t})\ [atoms/cm^3]. \tag{7.6}$$

L_2 was expressed by the following equation:

$$L_2 = 1.30 \times 10^{-12} exp(\frac{-0.75}{k_B t})\ [atoms/cm^3]. \tag{7.7}$$

Using L_1 in equation 7.5 as a parameter, I tried to derive L_1 by fitting with the experimental results of the annealing time dependence of D_{it} of wafer with C_3H_5 implantation. Figure 7.8 shows the result of fitting the D_{it} plot from equation 7.5. In addition, Figure 7.9 shows the Arrhenius plot using L_1 for each temperature. It was shown that the reaction at the SiO_2/Si interface can be expressed by a model assuming L_1 as a parameter obtained from the fitting results and the propotion of the Arrhenius plot. The L_1 obtained from the Arrhenius plot is shown below.

$$L_1 = 7.03 \times 10^{-13} exp(\frac{1.67}{kt})\ [atoms/cm^3]. \tag{7.8}$$

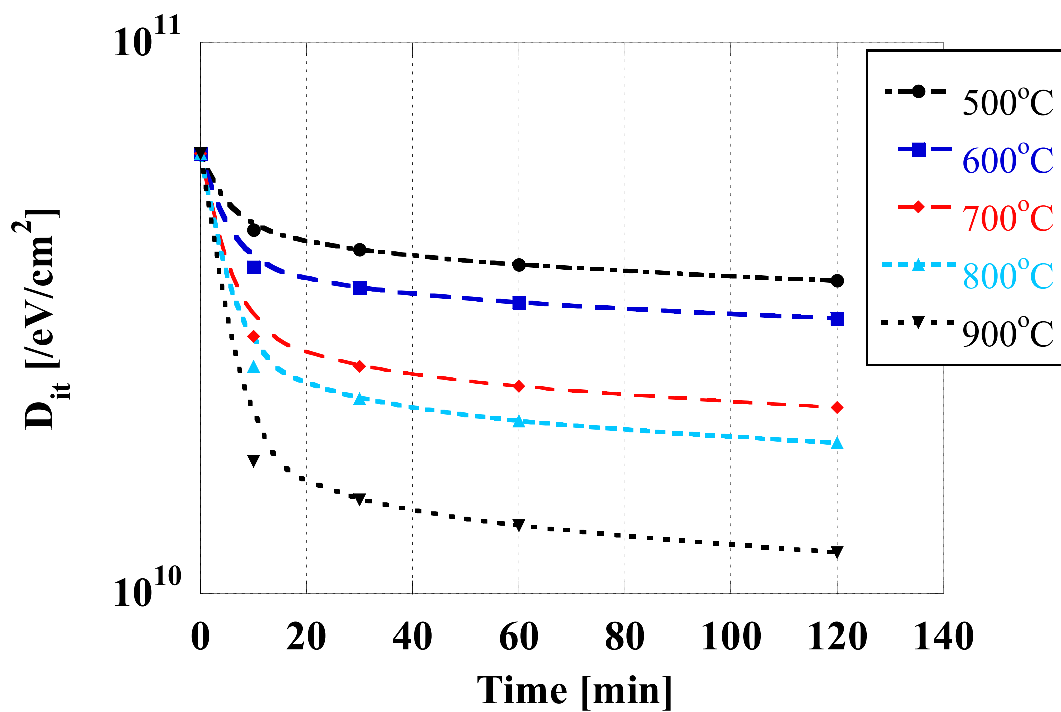

Figure 7.8: Fitting result of the D_{it} plot from equation 7.5.

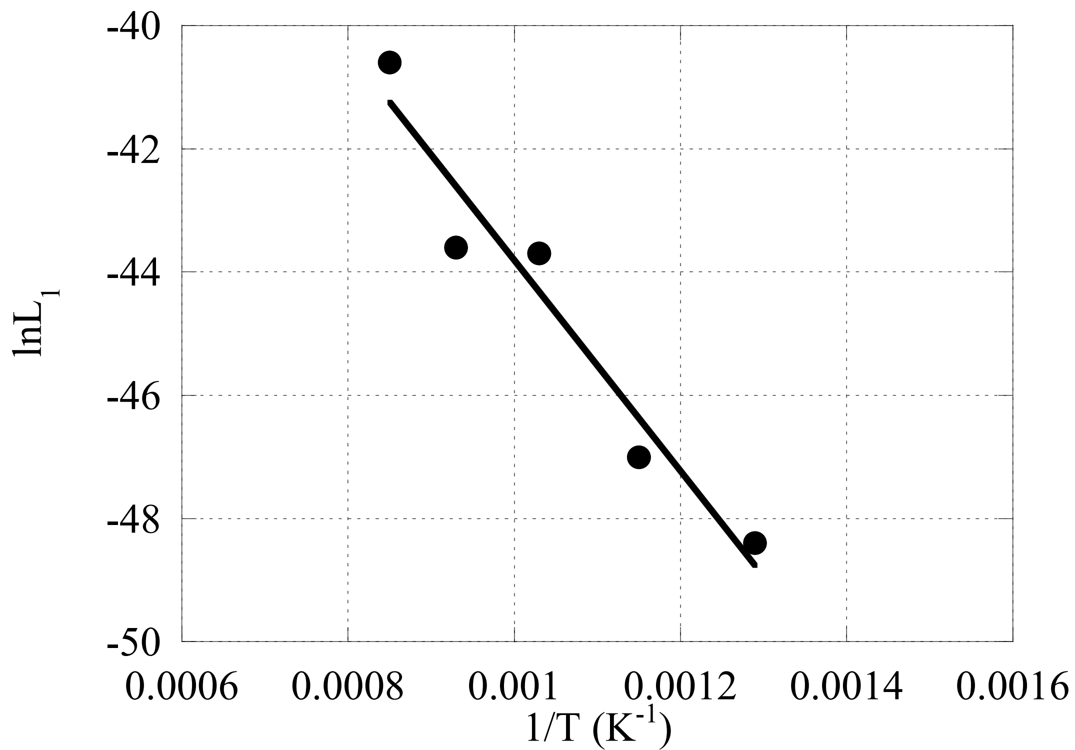

Figure 7.9: Arrhenius plot using L_1 for each temperature.

Then, I discuss the obtained activation energy of 1.67 eV. Stesmans reported that the activation energy in the reaction where hydrogen molecules terminate the Pb_0 center at the SiO_2/Si interface formed by dry oxidation on Si (100) is 1.51 eV [145]. The following is a model of the reaction at the SiO_2/Si interface by hydrogen molecules.

$$Si \cdot + H_2 \rightarrow Si - H + H. \tag{7.9}$$

Chapter 6 has demonstrated that hydrogen out-diffused from the C_3H_5-implanted region is hydrogen molecule under the annealing temperature and time below 900°C and 120 min. In addition, it was clarified in the above section that the change of D_{it} increased by electron beam irradiation has the proportion with the Pb_0 center density obtained by ESR method. Therefore, I found that hydrogen molecules out-diffusing from the implanted region of hydrocarbon-molecular-ion implantation region can reduce the SiO_2/Si interface state. Figure 7.10 shows a schematic diagram where hydrogen molecules diffused from the wafer at the Pb_0 center terminate. It is known that the diffusion rate of hydrogen molecules in silicon wafers is also high, and they can easily reach the SiO_2/Si interface. In the past, hydrogen was easily desorbed from the SiO_2/Si interface at annealing temperature above 500°C. The analysis of hydrogen passivation was limited to low-temperature annealing below 500°C. However, the activation energy for hydrogen passivation in high-temperature annealing at above 500°C has been derived assuming two reaction models for the SiO_2/Si interface and hydrogen. In addition, the hydrogen passivation effect of the hydrocarbon molecular ion implanted wafer at the high annealing temperature, which has not been reported before, was able to show the D_{it} reduction effect. It was found that the activation energy of the hydrogen termination reaction for the silicon dangling bond at the SiO_2/Si interface by hydrogen molecules even at the high temperature annealing is close to that of previous studies. The ability to reduce D_{it} under annealing conditions at 500 to 900°C is compatible with the device process, which has recently been progressing to lower temperatures. The results suggest that hydrogen molecules out-diffusing from the hydrocarbon-molecular-ion implanted region of hydrocarbon molecular ion can efficiently passivate the SiO_2/Si interface. This is an important characteristic that contributes to the reduction of the interface state of SiO_2/Si, which is required for high performance CMOS image sensors.

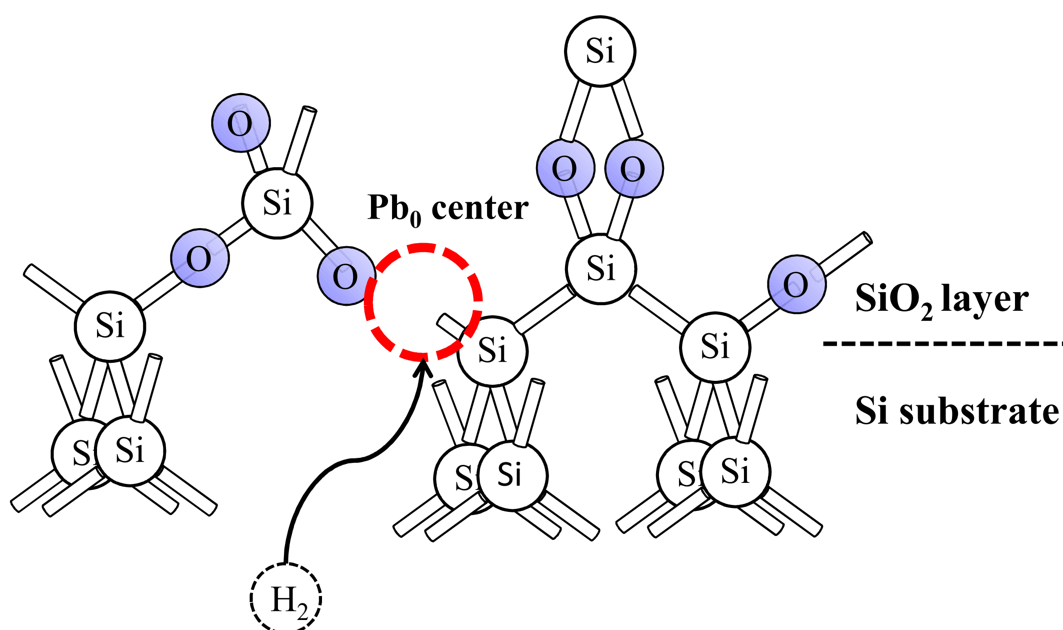

Figure 7.10: Schematic diagram of termination of Pb_0 center by molecular hydrogen diffused from C_3H_5-implanted region.

7.5 Summary

I demonstrated that C_3H_5 ion implanted epitaxial silicon wafer can reduce the D_{it} and Pb center density by C-V measurement and ESR, respectively. D_{it} and Pb center density without C_3H_5 increased after 700°C annealing. On the other hands, D_{it} and Pb center density with C_3H_5 decreased after 700°C annealing. These results indicate that C_3H_5 ion implanted epitaxial silicon wafer has the passivation effect for terminating the SiO_2/Si interface state defects. In addition, I derived the activation energy 1.67 eV of the hydrogen passivation reaction with hydrogen molecules and Si dangling bond at SiO_2/Si interface. Therefore, I found that hydrogen molecules out-diffusing from the implanted region of hydrocarbon-molecular-ion implantation region can reduce the SiO_2/Si interface state. I conclude that the passivation effects of the hydrocarbon molecular ion implanted epitaxial silicon wafer can contribute to the high electrical device performance such as low noise or dark current due to interface state defects at SiO_2/Si of CMOS image sensor.

Chapter 8

Conclusions

8.1 Thesis summary

This thesis related to the hydrocarbon molecular ion implanted epitaxial silicon wafer with hydrogen storage effect that contributes to the performance improvement of CMOS image sensors. Figure 8.1 shows the thesis approaches and solutions. This thesis clarified the hydrogen diffusion behavior and hydrogen termination effect of hydrocarbon-molecular-ion implanted wafers, which had not been previously clarified. These characteristics are expected to have the function of reducing white defect and noise by reducing the interface state density of CMOS image sensors.

In chapter 3 focused on the defect formation behavior after hydrocarbon molecular ion implantation and after epitaxial growth. The difference in defect formation between monomer carbon and hydrocarbon molecule ion implantation is shown. In addition, the effect of the implantation dose of hydrocarbon molecular ions on the defect formation behavior was clarified. Further, a defect of about 5 nm was observed in the projection range of hydrocarbon molecular ion after the epitaxial growth. It was analyzed by TCAD that they were formed as carbon-induced complexes.

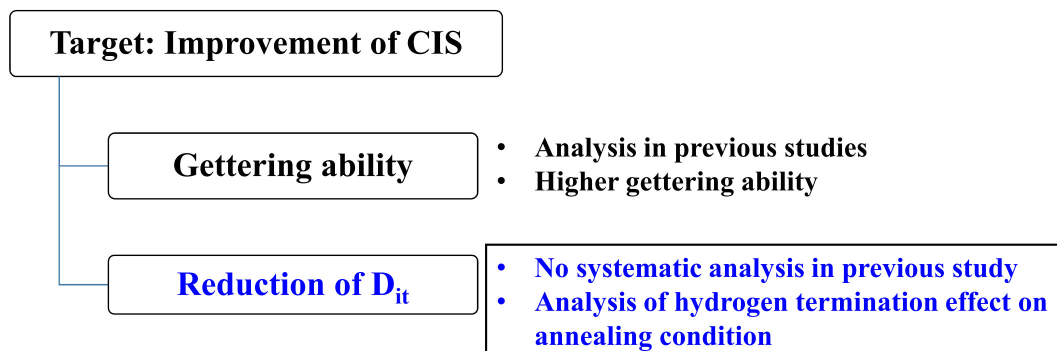

Figure 8.1: Thesis approaches and solutions.

In chapters 4 and 5, the hydrogen profile after hydrocarbon molecular ion implantation and the hydrogen diffusion behavior after epitaxial growth were investigated by SIMS analysis. Furthermore, the diffusion behavior that hydrogen is gradually re-released depending on the temperature and time conditions of the subsequent annealing has been clarified. Assuming a desorption model for this diffusion behavior, a dissociation activation energy of 0.76 eV was derived using reaction kinetic analysis. This activation energy was close to the C-H_2 binding energy in silicon bulk, and it was found that molecular hydrogen have been out-diffused from the projection range of hydrocarbon molecular ion. Furthermore, this chapter demonstrated that the defects due to the complex related to carbon having a size of 5 nm in chapter 3 are related to the binding state of hydrogen molecule.

Chapter 6 demonstrated the hydrogen diffusion behavior after higher temperature and longer time annealing than in chapter 4. It has been found that the diffusion behavior of hydrogen changes by a long-time annealing. I found that hydrogen desorbed from the projection range of hydrocarbon molecular ion may include not only molecular hydrogen but also atomic hydrogen.

In chapter 7, I demonstrated that C_3H_5 ion implanted epitaxial silicon wafer can reduce the D_{it} and Pb center density by CV measurement and ESR, respectively. D_{it} and Pb center density without C_3H_5 increased after 700°C annealing. On the other hands, D_{it} and Pb center density with C_3H_5 decreased after 700°C annealing. These results indicate that C_3H_5 ion implanted epitaxial silicon wafer has the passivation effect for terminating the SiO_2/Si interface state defects. In addition, I derived the activation energy 1.67 eV of the hydrogen termination reaction with hydrogen molecules and Si dangling bond at SiO_2/Si interface. Therefore, I found that hydrogen molecules out-diffusing from the projection range of hydrocarbon-molecular-ion implantation region can reduce the SiO_2/Si interface state.

I conclude that the hydrogen termination effects of the hydrocarbon molecular ion implanted epitaxial silicon wafer can contribute to the high electrical device performance such as low noise or dark current due to interface state defects at SiO_2/Si of CMOS image sensors.

8.2 Future technologies and directions

To further enhance CMOS image sensors performance, new gettering technology will have to introduce to complement the method of terminating the SiO_2/Si interface state. The new gettering technology uses not only hydrogen but also other elements that can terminate the SiO_2/Si interface state. This technology is called multi-element molecular ion implantation. For example, CH_3O added with oxygen and CH_4N added with nitrogen have been reported as multi-element molecular ions implanted epitaxial wafers [146, 147]. These multi-element molecular ion implanted epitaxial wafers have the same three characteristics as hydrocarbon molecular ion implanted wafers. In addition, the defect morphology in the projection range of multi-element molecular ion are two types of defect. One of defect is the same defect by the hydrocarbon molecular ion implantation. Another defect have been reported the formation of a {111} stacking fault defect in the projection range of multi-element molecular ion. Furthermore, the fundamental study have reported that hydrogen has two peaks in the projection range of multi-element molecular ion due to these two defects [141]. Therefore, multi-element molecular ion implanted wafer is considered to have a higher hydrogen storage effect than hydrocarbon molecular ion implanted wafer. This is likely to improve the hydrogen termination effect. Furthermore, CH_4N molecular-ion-implanted wafer added with nitrogen is expected the higher termination effect, because Si-CN binding energy is higher than Si-H binding energy. In chapter 7, there is concern that desorption of hydrogen from the SiO_2/Si interface may occur due to low temperature annealing during the BEOL process. Thus, CH_4N molecular-ion implanted wafer can be expected to have thermal stability. Also, the projection range is deeply implanted in CH_4N implantation unlike C_3H_5, it is considered that the termination effect is not affected because the epitaxial layer is thick.

Therefore, multi-element molecular ion implanted epitaxial wafer is also expected to contribute to the high performance of advanced CMOS image sensors.

8.3 Conclusions on this thesis

In the recent years, consumers require improvement the qualities such as high resolution imaging. Additionally, stacked CMOS image sensors are remarkable in terms of high resolution and integration compared to the conventional CMOS image sensors. Conventional CMOS image sensors are fabricated by using one wafer, which is formed logic circuit and pixel. On the other hand, multiple wafers are used for the stacked CMOS image sensors. The wafers are formed pixel, logic and memory, respectively and stacked by copper through-silicon via (TSV) to connect the wafers electrically. In addition, the each wafer is prepared by through different device fabrication processes, which is suitable for each purpose. For instance, device fabrication process for pixels needs low noise and low leakage characteristics. Whereas, device fabrication process for logic circuit needs high speed signal transmission and low resistivity. Thus, an important technical issues is known in the stacked CMOS image sensors. The issues is metallic impurities such as copper contamination in device active region and the increase of interface state in the stacked CMOS image sensors. In particular, copper is applied as TSV in stacked CMOS image sensors. Copper contamination in the device active region should be eliminated to improve the electrical performance of the stacked CMOS image sensors. Therefore, the gettering technology for the metal impurities contamination and the terminating of SiO_2/Si interface state will be extremely important.

I must simultaneously investigate the materials and the architectures to increase the performance of CMOS image sensors. Therefore, the silicon wafer design for advanced CMOS image sensors must be supremely important, and will need a very high level of technology. The imaging-devices contributed by our work has the responsibility to drive all of industry even for the future. Therefore, I would need to study and work aggressively for all happiness.

Bibliography

[1] IC Insights, "CMOS Image Sensor Growth Continues into Next Decade," 2019.

[2] S. R. Morrison, "A New Type of Photosensitive Junction Device," *Solid-State Electronics*, Vol.6, 1963, p. 485-494.

[3] J. W. Horton, R. V. Mazza and H. Dy, "The Scanistor a Solid State Image Scanner," in *Proc. IEEE*, 52, 12, 1964 p. 1513-1528.

[4] W. S. Boyle and G. E. Smith, "Charge Coupled Semiconductor Devices," *Bell System Technology Journal*, 49, 1970, p. 587-593.

[5] W. F. Kosonocky and J. E. Carnes, "Two-Phase Charge-Coupled Devices with Overlapping Polysilicon and Aluminum Gates," *RCA Review*, 1973, p.164-202.

[6] R. H. Walden, R. H. Krambeck, R. J. Strain, J. Mckenna, N. L. Schryer, and G. E. Smith, "The Buried Channel Charge Coupled Device," *Bell System Technology Journal*, 51, 1972, p.1636-1640.

[7] W. F. Kosonocky and J. E. Carnes, "Charge Coupled Digital Circuits," *IEEE J. Solid-State Circuits*, SC-6, 5, 1971, p. 314-322.

[8] E. R. Fossum, "Active pixel sensors (APS) - Are CCDs dinosaurs?," in *Proc. SPIE*, 1900, 1993, p. 2-14.

[9] E. R. Fossum, "CMOS Image Sensors: Electronic Camera-on-a-Chip," in *IEDM Tech. Dig.*, 1995, p. 17-25,.

[10] M. H. White, D. R. Lampe, F. C. Blaha, and I. A. Mack, "Characterization of surface channel CCD image arrays at low light levels," *IEEE J. Solid-State Circuits*, SC-9, 1, 1974, p.1-13.

[11] R. M. Guidash, T. H. Lee, P. P. K. Lee, D. H. Sackett, C. I. Drowley, M. S. Swensen, L. Arbaugh, R. Hollstein, F. Shapiro, and S. Domer, "A 0.6 nm CMOS Pinned Photodiode Color Imager Technology," in *IEDM Tech. Dig.*, 1997, p. 927-929.

[12] N. Teranishi, “No image lag photodiode structure in the interline CCD image sensor,” in *IEDM Tech. Dig.*, 1982, p. 113-116.

[13] E. R. Fossum, “CMOS Image Sensors: Electronic Camera on a Chip,” *IEEE Transaction Electron Device*, vol.44, no.10, 1997, p. 1689-1698.

[14] V. C. Venezia, A. C-W. Hsiung, K. Ai, X. Zhao, Z. Lin, D. Mao, Armin Yazdani, Eric A. G. Webster, and Lindsay A. Grant, “1.5μm dual conversion gain, backside illuminated image sensor using stacked pixel level connections with 13ke- full-well capacitance and 0.8e- noise,” in *IEDM Tech. Dig.*, 2018, p. 217.

[15] V. Goiffon, C. Virmontois, and P. Magnan, “Investigation of Dark Current Random Telegraph Signal in Pinned Photo Diode CMOS Image Sensors,” in *IEDM Tech. Dig.*, 2011, p. 841, Washington, USA.

[16] K. Graff, “Metal Impurities in Silicon-Devices Fabrication,” *Springer*, 1994.

[17] A. Goetzberger and W. Shockley, “Metal Precipitates in Silicon pn Junctions,” *Journal of Applied Physics*, Vol. 31, 1960, p. 1821.

[18] E. R. Weber, “Transition metals in silicon,” *Applied Phyics Letters*,30, 1983, p. 1.

[19] J.S. Kang and D.K. Schroder, “Gettering in silicon,” *Journal of Applied Physics*, 65, 1989, p. 2974.

[20] F. Shimura, “Semiconductor Silicon Crystal Technology” *Academic Press*, 1988.

[21] D. Gilles, E. R. Weber, and S. Hahn, “Mechanism of internal gettering of interstitial impurities in Czochralski-grown silicon,” *Physical Review*, 64, 1990, p. 196.

[22] M. Aoki, A. Hara, and A. Ohsawa, “Fundamental properties of intrinsic gettering of iron in a silicon wafer,” *Journal of Applied Physics* 72, 1992, p. 895.

[23] K-W. Lee, J-C. Bea, T. Fukushima, T. Tanaka, and M. Koyanagi, “Cu Retardation Performance of Extrinsic Gettering Layers in Thinned Wafers Evaluated by Transient Capacitance Measurement,” *Journal of Electrochemical Society*, 158, 2011, p. 795.

[24] H. I. Kwon, I. M. Kang, B. G. Park, J. D. Lee, and S. S. Park, “The analysis of dark signals in the CMOS APS imagers from the characterization of test structures,” *IEEE Transactionon Electron Devices* 51, 2004, p. 178.

[25] T. Kuroda, "Essential Principles of Image Sensors," *CRC press*, 2014.

[26] F. Domengie, J. L. Regolini, and D. Bauza, "Study of Metal Contamination in CMOS Image Sensors by Dark-Current and Deep-Level Transient Spectroscopies," *Journal of Electronic Materials*, 39, 2010, p. 625.

[27] T. Kuroi, Y. Kawasaki, S. Komori, K. Fukumoto, M. Inuishi, K. Tsukamoto, H. Shinyashiki, and T. Shingyouji, "Proximity Gettering of Heavy Metals by High-Energy Ion Implantation," *Japanese Journal of Applied Physics*, 32, 1993, p. 303.

[28] T. Higuchi, H. Kanbe,T. Kusaka, M. Ohashi, R. Takizawa, "Semiconductor substrate and solid-state image-pickup device and manufacture thereof" *Japan Patent* H06338507A, 1994.

[29] I. Yamada, J. Matsuo,M. Toyoda, and A. Kirkpatric, "Materials processing by gas cluster ion beams," *Materials Scienece and Engineering*, R34, 2001, p. 231.

[30] K. Kurita, T. Kadono, R. Okuyama, S. Shigematsu, R. Hirose, A. Onaka-Masada, Y. Koga, and H. Okuda, "Proximity gettering technology for advanced CMOS image sensors using carbon cluster ion implantation technique: A review," *Physica Status Solidi A*, 214, 2017, 1700216.

[31] K. Kurita, T. Kadono, S. Shigematsu, R. Hirose, R. Okuyama, A. Onaka-Masada, H. Okuda, and Y. Koga, "Proximity Gettering Design of Hydrocarbon-Molecular-Ion-Implanted Silicon Wafers Using Dark Current Spectroscopy for CMOS Image Sensors," *Sensors*, 19, 2019, p. 2073.

[32] K. Kurita, T. Kadono, R. Okuyama, R. Hirose, A. Onaka-Masada, Y. Koga, and H. Okuda, "Proximity gettering of C_3H_5 carbon cluster ion-implanted silicon wafers for CMOS image sensors: Gettering effects of transition metal, oxygen, and hydrogen impurities," *Japanese Journal of Applied Physics*, 55, 2016, p. 121301.

[33] A. Onaka-Masada, T. Nakai, R. Okuyama, H. Okuda, T. Kadono, R. Hirose, Y. Koga, K. Kurita, and K. Sueoka, "Effect of low-oxygen-concentration layer on iron gettering capability of carbon-cluster ion-implanted Si wafer for CMOS image sensors," *Japanese Journal of Applied Physics*, 57, 2018, p. 021304.

[34] A. Onaka-Masada, R. Okuyama, T. Nakai, S. Shigematsu, H. Okuda, K. Kobayashi, R. Hirose, T. Kadono, Y. Koga, M. Shinohara, K. Sueoka, and K. Kurita, "Gettering mechanism in hydrocarbon-molecular-ion-implanted

epitaxial silicon wafers revealed by three-dimensional atom imaging," *Japanese Journal of Applied Physics*, 57, 2018, p. 091302.

[35] A. Onaka-Masada, R. Okuyama, S. Shigematsu, H. Okuda, T. Kadono, R. Hirose, Y. Koga, K. Sueoka, and K. Kurita, "Gettering Sinks for Metallic Impurities Formed by Carbon-Cluster Ion Implantation in Epitaxial Silicon Wafers for CMOS Image Sensor," *IEEE Journal of the Electron Devices Society*, 6, 2018, p. 1200.

[36] R. Okuyama, A. Masada, T. Kadono, R. Hirose, Y. Koga, H. Okuda, and K. Kurita, "Trapping and diffusion kinetic of hydrogen in carbon-cluster ion-implantation projected range in Czochralski silicon wafers," *Japanese Journal of Applied Physics*, 56, 2017, p. 025601.

[37] M. Hourai, T. Naridomi, Y. Oka, K. Murakami, S. Sumita, N. Fujino and T. Shiraiwa, "A Method of Quantitative Contamination with Metallic Impurities of the Surface of a Silicon Wafer," *Japanese Journal of Applied Physics*, 27, 1988, p. 2361.

[38] S. Shigematsu, R. Okuyama, R. Hirose, T. Kadono, A. Onaka-Masada, A. Suzuki, K. Kobayashi, H. Okuda, Y. Koga and K. Kurita "Influence of oxygen on copper gettering in hydrocarbon molecular ion implanted region using atom probe tomography" *Nuclear Inst. and Methods in Physics Research B*, 478, 2020, p. 99.

[39] T. Shoyama, "Influence of various impurities on performance of CMOS image sensor," in *The 8th Forum on the 773 Science and Technology of Silicon Materials* 2018 (Okayama, Japan, 2018) p. 184-186.

[40] H. Kitagawa, S. Tanaka, H. Nakashima and M. Yoshida "Electrical Properties of Nickel in Silicon" *Journal of Electronic Materials*, 20, 1991, p. 441.

[41] T. Yamaguchi, in *145th JSPS Committee on Processing and Characterizations of Crystals*, 153th Seminar, 2017, p. 20.

[42] J. S. Kang and D. K. Schroder, "Gettering in silicon," *Journal of Applied Physics*, 65, 1989, p. 2974.

[43] J. L. Benton, P. A. Stoik, D. J. Eaglesham, D. C. Jacobson, J-Y. Cheng, J. M. Poate, N. T. Ha, T. E. Haynes and S. M. Myers, "Iron Gettering Mechanisms in Silicon," *Journal of Applied Physics*, 80, 1996, p. 3275.

[44] S. Shirasawa, K. Sueoka, T. Yamaguchi and K. Maekawa, "Density functional theory calculations for estimation of gettering sites of C, H, intrinsic point defects and related complexes in Si wafers," *Material Science Semiconductor Processing*, 44, 2016, p. 13.

[45] Honig, R.E., "The Growth of Secondary Ion Mass Spectrometry (SIMS) A Personal View of Its Development, in Secondary Ion Mass Spectrometry SIMS V," *Springer Berlin Heidelberg*, A. Benninghoven, et al., Editors. 1986, p. 2-15.

[46] Storms, H. A., K. F. Brown, and J. D. Stein, "Evaluation of a cesium positive ion source for secondary ion mass spectrometry," *Analytical Chemistry*, 49(13), 1977, p. 2023-2030.

[47] L . R. Lake and K Mauersberger, "Investigation of atomic oxygen in mass spectrometer ion sources," *International Journal of Mass Spectrometry and Ion Physics*, 13(4), 1974, p. 425-436.

[48] S. Horiuchi, "Fundamentals of High-Resolution Transmission Electron Microscopy" *Elsevier Science*, 1994.

[49] S. Morishita, J. Yamasaki, K. Nakamura, T. Kato, and N. Tanaka, "Diffractive imaging of the dumbbell structure in silicon by spherical-aberration-corrected electron diffraction," *Applied Physics Letters*, 93, 2008, p, 183103.

[50] R. W. Dutton, "Technology CAD Computer Simulation of IC Processes and Devices," in *Kluwer Academic Publishers*, 1993.

[51] "Synopsys Sentaurus Process Usersf Manual, Release J-2014.09" *Synopsys Inc., Z'́urich*, 2014.

[52] "Advanced front-end technology modeling for ultimate integrated circuits, Public final report," in *IST Project 027152 ATOMICS*, Oct. 2009.

[53] H. Wang, A. Chroneos, C. A. Londos, E. N. Sgourou and U. Schwingenschlogl "Carbon related defects in irradiated silicon revisited" *Scientific Reports*, 4, 2014, p. 4909

[54] C. N. Berglund, "Surface states at steam-grown silicon-silicon dioxide interfaces," *IEEE Transaction Electron Devices*, 13(10), 1966, p. 701.

[55] M. Kuhn, "A quasi-static technique for MOS C-V and surface state measurements," *Solid-State Electronics*, 13, 1970, p. 873.

[56] Y. Nishi, "Study of Silicon-Silicon Dioxide Structure by Electron Spin Resonance I," *Japanese Journal of Applied Physics*, 10, 1971, p. 52.

[57] Y. Nishi, T. Tanaka, and A. Ohwada, "Study of Silicon-Silicon Dioxide Structure by Electron Spin Resonance II," *Japanese Journal of Applied Physics*, 11, 1972, p. 85.

[58] P. J. Caplan, E. H. Poindexter, B. E. Deal, and R. R. Razouk, "ESR centers, interface states, and oxide fixed charge in thermally oxidized silicon wafers," *Journal of Applied Physics*, 50, 1979, p. 5847.

[59] E. H. Poindexter, P. J. Caplan, B. E. Deal, and R. R. Razouk, "Interface states and electron spin resonance centers in thermally oxidized (111) and (100) silicon wafers," *Journal of Applied Physics*, 52, 1981, p. 879.

[60] C. A. Londos, E. N. Sgourou, and A. Chroneos, "Defect engineering of the oxygen-vacancy clusters formation in electron irradiated silicon by isovalent doping: An infrared perspective," *Journal of Applied Physics*, 112, 2012, p. 123517.

[61] R. Pinacho, P. Castrillo, M. Jaraiz, I. Martin-Bragado, J. Barbolla, H. J. Gossmann, G. H. Gilmer and J. L. Benton, "Carbon in silicon: Modeling of diffusion and clustering mechanisms," *Journal of Applied Physics*, 92, 2002, p. 1582.

[62] B. Hourahine, R. Jones, S. Oberg, V. P. Markevich, R. C. Newman, J. Hermansson, M. Kleverman, J. L. Lindstrom, L. I. Murin, N. Fukata and M. Suezawa, "Evidence for H_2 trapped by carbon impurities in silicon," *Physica B*, 308, 2001, p. 197.

[63] V. P. Markevich and M. Suezawa, "Hydrogen-oxygen interaction in silicon at around 50°C," *Journal of Applied Physics*, 83, 1998, p. 2988.

[64] T. Mori, K. Otsuka, N. Umehara, K. Ishioka, M. Kitajima, S. Hishita and K. Murakami, "Thermal behavior of hydrogen molecules trapped by multivacancies in silicon," *Physica B*, 302-303, 2001, p. 239.

[65] B. Hourahine, R. Jones, S. Oberg, R. C. Newman, P. R. Briddon and E. Roduner, "Hydrogen molecules in silicon located at interstitial sites and trapped in voids," *Physical Review B*, 57 (1998) R12666.

[66] F. Russo, G. Moccia, G. Nardone, R. Alfonsetti, G. Polsinelli, A. DofAngelo, A. Patacchiola, M. Liverani, P. Pianezza, T. Lippa, M. Carlini, M. L. Polignano,

I. Mica, E. Cazzini, M. Ceresoli, and D. Codegoni, "Proximity gettering of slow diffuser contaminants in CMOS image sensors," *Solid-State Electron*, 91,2014, p. 91.

[67] N. Krause, H. Soltau, D. Hauff, J. Kemmer, D. Stotter, L. Struder, and J. Weber, "Metal contamination analysis of the epitaxial starting material for scientific CCDs," *Nuclear Instruments and Methods Physics Research Section A*, 439, 2000, p. 228.

[68] L. Jastrzebski, R. Soydan, H. Elabd, W. Henry, and E. Savoye, The Effect of Heavy Metal "Contamination on Defects in CCD Imagers: Contamination Monitoring by Surface Photovoltage," *Journal of Electrochemical Society*, Vol. 137, No. 1, 1990, p. 242.

[69] E. A. G. Webster, Member, IEEE, R. L. Nicol, L. Grant, and D. Renshaw, "Per-pixel dark current spectroscopy measurement and analysis in CMOS image sensors," *IEEE Transaction Electron Devices*,. 57, No. 9, 2010, p. 2176.

[70] L. Jastrzebski, "Heavy metal contamination during integrated-circuit processing: Measurements of contamination level and internal gettering efficiency by surface photovoltage," *Materials Science and Engineering*, B4, 1989, p. 113.

[71] B. Shen, J. Jablonski, T. Sekiguchi, and K. Sumino, "Influences of Cu and Fe Impurities on Oxygen Precipitation in Czochralski-Grown Silicon," *Japanese Journal of Applied Physics*, 35, 1996, p. 4187.

[72] K. D. Beyer and T. H. Yeh, "Impurity gettering of silicon damage generated by ion implantation through SiO_2 layers," *IJournal of Electrochemical Society*, 129, 1982, p. 2527.

[73] R. Hoelzl, K. J. Range, and L. Fabry, "Modeling of Cu gettering in p- and n-type silicon and in poly-silicon," *Applied Physics A*, 75, 2002, p. 525.

[74] Y. Kawai, N. Konishi, J. Watanabe, and T. Ohmi, " Ultra-low-temperature growth of high-integrity gate oxide films by low-energy ion-assisted oxidation," *Applied Physics Letters*, 64, 1994, p. 2223.

[75] K. Goto, J. Matsuo, T. Sugii, H. Minakata, and I. Yamada, "Novel shallow junction technology using decaborane," in *IEDM Tech Dig.*, 1996, IEEE, p. 435.

[76] H. Wong and N. W. Cheung, " Proximity gettering with mega-electron-volt carbon and oxygen implantations," *Applied Physics Letters*, 52, 1988, p. 1023.

[77] P. Werner, S. Eichler, G. Mariani, R. Kogler, and W. Skorupa, “Investigation of C_xSi defects in C implanted silicon by transmission electron microscopy,” *Applied Physics Letters*, 70, 1997, p. 252.

[78] J. W. Medernach, T. A. Hill, S. M. Myers, and T. J. Headley, “ Microstructural Properties of Helium Implanted Void Layers in Silicon as Related to Front-Side Gettering,” *IJournal of Electrochemical Society*, 143, 1996, p. 725.

[79] R. Liefting, R. C. M. Wijburg, J. S. Custer, H. Wallinga, Member, IEEE, and F. W. Saris, “Improved device performance by multistep or carbon co-implants,” *IEEE Transaction Electron Devices*,. 41, 1994, p. 50.

[80] R. Kogler, A. Peeva, A. Lebedev, M. Posselt, W. Skorupa, G. Ozelt, H. Hutter, and M. Behar, “Cu gettering in ion implanted and annealed silicon in regions before and beyond the mean projected ion range ,” *Journal of Applied Physics*, 94, 2003, p. 3834.

[81] C. David, B. Sundarvel, T. R. Ravindran, K. G. M. Nair, B. K. Panigrahi, H. P. Lenka, B. Joseph, and D. P. Mahapatra, “Observation of an enhanced gettering effect in silicon under germanium molecular ion implantation,” *Applied Physics A*, 88, 2007, p. 397.

[82] V. R. Chavva, B. Colombeau, K. V. Rao, J. C. Toh, and T. Henry, “An effective metals gettering process with a cryogenic carbon implant for CMOS image sensors,” *Ion Implantation Technology*, 1496, 2012, p. 265.

[83] M. Tanomura, D. Takeuchi, J. Matsuo, G. H. Takaoka, and I. Yamada, “Fullerene ion irradiation to silicon,” *Nuclear Instruments and Methods in Physics Research Section B*, 121, 1997, p. 480.

[84] T. Aoki, T. Seki, J. Matsuo, Z. Insepov, and I. Yamada, “Molecular dynamics simulation of a carbon cluster ion impacting on a carbon surface,” *Materials Chemistry and Physics*, 54, 1998, p. 139.

[85] L. Romano, K. S. Jones, K. Sekar, and W. A. Krull, “Amorphization of Si using cluster ions,” *Journal of Vacuum Society and Technology*, 27, 2009, p. 597.

[86] N. G. Rudawski, L. R. Whidden, V. Craciun, and K. S. Jones, “Amorphization and Solid-Phase Epitaxial Growth of C-Cluster Ion-Implanted Si,” *Journal of Electron Materials*, 38, 2009, p. 1926.

[87] H. J. Woo, G. D. Kim, H. W. Choi, and J. K. Kim, “Characterization of SiC nanostructures in crystalline and porous silicon formed by ion beam synthesis,” *Journal Korean Physics Society*, 56, No. 6, 2010, p. 2063.

[88] A. V. Wieringen and N. Warmoltz, "On the permeation of hydrogen and helium in single crystal silicon and germanium at elevated temperatures," *Physica*, 22, 1956, p. 849.

[89] S. J. Pearton, J. W. Corbett, and T. S. Shi, "Hydrogen in crystalline semiconductors," *Applied Physics A*, 43, 1987, p. 153.

[90] S. J. Pearton, J. W. Corbett, and M. Stavola, "Hydrogen Incorporation in Crystalline Semiconductors," *Hydrogen in Crystalline Semiconductors*, Springer, Berlin, 1992.

[91] B. P. Lemke and D. Haneman, "Dangling bonds on silicon," *Physical Review B*, 17, 1978, p. 1893.

[92] K. Ohyu, *Dr. Thesis, Faculty of Engineering, University of Tokyo*, Tokyo, 1997 [in Japanese].

[93] K. L. Brower, "Dissociation kinetics of hydrogen-passivated (111) Si-SiO_2 interface defects," *Physical Review B*, 42, 1990, p. 3444.

[94] K. Bergman, M. Stavola, S. J. Pearton, and J. Lopata, "Donor-hydrogen complexes in passivated silicon," *Physical Review B*, 37, 1988, p. 2770.

[95] J. I. Pankov, D. E. Carlson, J. E. Berkeyheiser, and R. O. Wance, "Neutralization of Shallow Acceptor Levels in Silicon by Atomic Hydrogen," *Physical Review Letters*, 51, 1983, p. 2224.

[96] A. D. Marwick, G. S. Oehrlein, and N. M. Johnson, "Structure of the boron-hydrogen complex in crystalline silicon," *Physical Review B*, 36, 1987, p. 4539.

[97] N. M. Johnson, C. Herring, and D. J. Chadi, "Interstitial hydrogen and neutralization of shallow-donor impurities in single-crystal silicon," *Physical Review Letters*, 56, 1986, p. 769.

[98] N. M. Johnson, F. A. Ponce, R. A. Street, and R. J. Nemanich, "Defects in single-crystal silicon induced by hydrogenation," *Physical Review B*, 35, 1987, p. 4166.

[99] K. Murakami, N. Fukata, S. Sasaki, K. Ishioka, M. Kitajima, S. Fujimura, J. Kikuchi, and H. Haneda, "Hydrogen Molecules in Crystalline Silicon Treated with Atomic Hydrogen," *Physical Review Letters*, 77, 1996, p. 3161.

[100] N. Fukata, S. Sasaki, K. Murakami, K. Ishioka, M. Kitajima, S. Fujimura, and J. Kikuchi, "Formation of Hydrogen Molecules in n-Type Silicon," *Japanese Journal of Applied Physics*, 35, 1996, p. L1069.

[101] N. Fukata, S. Sasaki, K. Murakami, K. Ishioka, K. G. Nakamura, M. Kitajima, S. Fujimura, J. Kikuchi, and H. Haneda, “Hydrogen molecules and hydrogen-related defects in crystalline silicon,” *Physical Review B*, 56, 1997, p. 6642.

[102] N. Fukata, S. Sasaki, S. Fujimura, H. Haneda, and K. Murakami, “Hydrogen Passivation of Donors and Hydrogen States in Heavily Doped n-Type Silicon,” *Japanese Journal of Applied Physics*, 35, 1996, p. 3937.

[103] N. Fukata, S. Sato, H. Morihiro, K. Murakami, K. Ishioka, M. Kitajima, and S. Hishita, “Dopant dependence on passivation and reactivation of carrier after hydrogenation,” *Journal of Applied Physics*, 101, 2007, p. 046107.

[104] S. J. Pearton and A. J. Tavendale, “ The electrical properties of deep copper and nickel related centers in silicon,” *Journal of Applied Physics*, 54, 1983, p. 1375.

[105] S. J. Pearton and A. J. Tavendale, “Electrical properties of deep silver-and iron-related centres in silicon,” *Journal of Physics C*, 17, 1984, p. 6701.

[106] T. Sadoh, K. Tsukamoto, A. Baba, D. Bai, A. Kenjo, T. Tsurushima, H. Mori, and H. Nakashima, “Deep level of iron-hydrogen complex in silicon,” *Journal of Applied Physics*, 82, 1997, p. 3828.

[107] J. W. Leung, C. E. Ascheron, and M. Petravic, “ Gettering of copper to hydrogen-induced cavities in silicon,” *Applied Physics Letters*, 66, 1995, p. 1231.

[108] B. Terreault, “Hydrogen blistering of silicon: Progress in fundamental understanding,” *Physica Status Solidi A*, 204, 2007, p. 2129.

[109] S. Reboh, M. F. Beaufort, J. F. Barbot, J. Grilhe, and P. F. P. Fichtner, “Orientation of H platelets under local stress in Si,” *Applied Physics Letters*, 93, 2008, p. 022106.

[110] G. F. Cerofolini, F. Corni, S. Frabboni, C. Nobili, G. Ottaviani, and R. Tonini, “Ultradense gas bubbles in hydrogen-or helium-implanted (or coimplanted) silicon,” *Materials Science and Engineering B*, 71, 2000, p. 196.

[111] K. J. Chang and D. J. Chadi, “Hydrogen bonding and diffusion in crystalline silicon,” *Physical Review B*, 40, 1989, p. 11644.

[112] D. J. Chadi and C. H. Park, “Electronic properties of hydrogen-derived complexes in silicon,” *Physical Review B*, 52, 1995, p. 8877.

[113] N. Fukata and M. Suezawa, "Annealing behavior of hydrogen-defect complexes in carbon-doped Si quenched in hydrogen atmosphere," *Journal of Applied Physics*, 87, 2000, p. 8361.

[114] N. Fukata and M. Suezawa, "Formation and annihilation of H-point defect complexes in quenched Si doped with C," *Journal of Applied Physics*, 88, 2000, p. 4525.

[115] N. Fukata, A. Kasuya, and M. Suezawa, "Vacancy Formation Energy of Silicon Determined by a New Quenching Method," *Japanese Journal of Applied Physics*, 40, 2001, p. 854.

[116] T. Akiyama and A. Oshiyama, "Multivacancy and Its Hydrogen Decoration in Crystalline Si," *Japanese Journal of Applied Physics*, 38, 1999, p. L1363.

[117] K. Ishioka, M. Kitajima, S. Tateishi, K. Nakanoya, N. Fukata, T. Mori, K. Murakami, and S. Hishita, "Hydrogen molecules trapped by multivacancies in silicon," *Physical Review B*, 60,1999, p. 10852.

[118] T. Mori, K. Otsuka, N. Umehara, K. Ishioka, M. Kitajima, S. Hishita, and K. Murakami, "Multivacancies trapping hydrogen molecules," *Physica B*, 308-310, 2001, p. 171.

[119] A. L. Endros, W. Kruhler, and F. Koch, "Electronic properties of the hydrogen-carbon complex in crystalline silicon," *Journal of Applied Physics*, 72, 1992, p. 2264.

[120] B. N. Mukashev, Kh. A. Abdullin, Yu. V. Gorelkinskii, M. F. Tamendarov, and S. Zh. Tokmoldin, "Hydrogen-enhanced clusterization of intrinsic defects and impurities in silicon," *Physica B*, 302-303, 2001, p. 249.

[121] O. Andersen, A. R. Peaker, L. Dobaczewski, K. B. Nielsen, B. Hourahine, R. Jones, P. R. Briddon, and S. Oberg, "Electrical activity of carbon-hydrogen centers in Si," *Physical Review B*, 66, 2002, p. 235205.

[122] F. Russo, G. Nardone, M. L. Polignano, A. DofErcole, F. Pennella, M. D. Felice, A. D. Monte, A. Matarazzo, G. Moccia, G. Polsinelli, A. DofAngelo, M. Liverani, and F. Irrerac, "Dark Current Spectroscopy of Transition Metals in CMOS Image Sensors," *ECS Journal of Solid State Science and Technology*, 6, 2017, p. 217.

[123] A. Ohtani and T. Kaneda, "Analysis of Image lag Phenomenon Mechanism of CMOS image sensor" in *Ext. Abstr. 77th Autumn Meet. Japan Society of Applied Physics and Related Societies*, 2016, 14p-P6-11.

[124] J. Jung, D. W. Kwon, and J. Kim, "Decreasing Dark Current of Complementary Metal Oxide Semiconductor Image Sensors by New Postmetallization Annealing and Ultraviolet Curing," *Japanese Journal of Applied Physics*, 47, 2008, p. 139.

[125] B. Park, J. Jung, C-R. Moon, S. Hwang, Y. Lee, D. Kim, K. Paik, J. Yoo, D. Lee, and K. Kim, "Deep Trench Isolation for Crosstalk Suppression in Active Pixel Sensors with 1.7 μm Pixel Pitch," *Japanese Journal of Applied Physics*, 46, 2007, p. 2454.

[126] J. Jung, D-W. Kwon, and J. Kim, "Reduction of Random Noise in Complementary Metal Oxide Semiconductor Image Sensors by Gate Oxide Interface Control," *Japanese Journal of Applied Physics*, 45, 2006, p. 3466.

[127] J. P. Carrere, S. Place, J. P. Oddou, D. Benoit, and F. Roy, "CMOS image sensor: Process impact on dark current," in *IEEE Int. Reliability Physics Symp. (IRPS)*, 2014, 3C11.

[128] D. Benoit, J. Regolini, and P. Morin, "Hydrogen desorption and diffusion in PECVD silicon nitride application to passivation of CMOS active pixel sensors," *Microelectronic Engineering*, 84, 2007, p. 2169.

[129] L. D. Thanh and P. Balk, "Elimination and Generation of Si-SiO_2 Interface Traps by Low Temperature Hydrogen Annealing," *Journal of Electrochemical Society*, 135, 1988, p. 1797.

[130] J. L. Regolini, D. Benoit, and P. Morin, "Passivation issues in active pixel CMOS image sensors," *Microelectronics Reliability*, 47, 2007, p. 739.

[131] V. Goiffon, P. Magnan, P. Martin-Gonthier, C. Virmontois, and M. Gaillardin, "New Source of Random Telegraph Signal in CMOS Image Sensors," in *International Image Sensor Workshop*, June 2011, Hakodate, Japan R27.

[132] B. Zhang, K. Kagawa, T. Takasawa, M. W. Seo, K. Yasutomi and S. Kawahito, "RTS noise and dark current white defects reduction using selective averaging based on a multi-aperture system," *Sensors*, 14, 2014, p. 1528.

[133] A. Vici, F. Russo, N. Lovisi, L. Latessa, A. Marchioni, A. Casella, F. Irrera, "Through-silicon-trench in back-side-illuminated CMOS image sensors for the improvement of gate oxide long term performance," in *IEEE International Electron Devices Meeting (IEDM 2018)*, Dec 2018, Sanfrancisco, USA, 32.3.

[134] R. Okuyama, A. Masada, T. Kadono, R. Hirose, Y. Koga, H. Okuda, and K. Kurita, "Gettering Ability of Carbon Cluster Ion Implanted Epitaxial Silicon Wafer for Metal-Impurity Contamination during Device Fabrication Process," in *Proc. 18th Scientific Int. Symp. SIMS and Related Techniques Based on Ion-Solid Interactions*, 2016, p. 20.

[135] R. Okuyama, S. Shigematsu, R. Hirose, A. Masada, T. Kadono, Y. Koga, H. Okuda, and K. Kurita, "Trapping and diffusion behaviour of hydrogen simulated with TCAD in projection range of carbon-cluster implanted silicon epitaxial wafers for CMOS image sensors," *Phys. Status Solidi C*, 14, 2017, p. 1700036.

[136] E. Cartier, J. H. Stathis, and D. A. Buchanan, "Passivation and depassivation of silicon dangling bonds at the Si/SiO2 interface by atomic hydrogen," *Applied Physics Letters*, 63, 1993, p. 1510.

[137] P. Santos, J. Coutinho, S. Oberg, M. Vaqueiro-Contreras, V. P. Markevich, M. P. Halsall, and A. R. Peaker, " Theory of a carbon-oxygen-hydrogen recombination center in n-type Si," *Phys. Status Solidi A*, 214, N0.7, 2017, p. 1700309.

[138] S. Kawahito, and Min-W. Seo, "Noise Reduction Effect of Multiple-Sampling-Based Signal-Readout Circuits for Ultra-Low Noise CMOS Image Sensors," *Sensors*, 16, 2016, p. 1867.

[139] D. Misra and R. K. Jarwal, "Interface Hardening with Deuterium Implantation," *Journal of the Electrochemical Society*, 149(8), 2002, p. G446.

[140] T. Kundu and D. Misra, "Si/SiO_2 Interface Passivation Using Hydrogen and Deuterium Implantation," *Electrochemical and Solid-State Letters*, 8(2), 2005, p. G35.

[141] R. Okuyama, A. Onaka-Masada, A. Suzuki, K. Kobayashi, S. Shigematsu, T. Kadono, R. Hirose, Y. Koga, K. Kurita, "Molecular and Atomic Hydrogen Diffusion Behavior by Reaction Kinetic Analysis in Projection Range of Hydrocarbon Molecular Ion for CMOS Image Sensors," *Physica Status Solidi A*, 216(17), 2019, p. 1900175.

[142] P. M. Lenahan and J. F. Conley, "What can electron paramagnetic resonance tell us about the Si/SiO_2 system?," *Journal of Vacuum Science and Technology*, B 16(4), 1998, p. 2134.

[143] M. L. Reed and J. D. Plummer, " Chemistry of Si-SiO_2 interface trap annealing," *Journal of Applied Physics*, 63(12), 1988, p. 5776.

[144] I. Kurachi, H. Takano, and H. Kanie, "Study of oxide-silicon interface state generation and annihilation by rapid thermal processing," *Japanese Journal of Applied Physics*, 54, 2015, p. 086501.

[145] A. Stesmans, "Passivation of Pb_0 and Pb_1 interface defects in thermal (100) Si/SiO_2 with molecular hydrogen," *Applied Physics Letters*, 68(15), 8, 1996, p. 2076.

[146] R. Hirose, T. Kadono, R. Okuyama, S. Shigematsu, A. Onaka-Masada, H. Okuda, Y. Koga, and K. Kurita, "Proximity gettering of silicon wafers using CH_3O multielement molecular ion implantation technique," *Japanese Journal of Applied Physics*, 57, 2018, p. 096503.

[147] A. Suzuki, T. Kadono, R. Hirose, R. Okuyama, A. Masada, S. Shigematsu, K. Kobayashi, Y. Koga, K. Kurita, "Fundamental Characteristics of Cyanide Related Multielement Molecular Ion Implanted Epitaxial Si Wafers for High Performance CMOS Image Sensors," *Physica Status Solidi A*, 216, 2019, p. 1900172.

[148] R. Okuyama, A. Onaka-Masada, S. Shigematsu, T. Kadono, R. Hirose, Y. Koga, H. Okuda, and K. Kurita, "Diffusion kinetic of hydrogen in CH_3O-molecular-ion-implanted silicon wafer for CMOS image sensors," *Japanese Journal of Applied Physics*, 57, 2018, p. 081302.

List of Papers and Presentations

Papers in International Journals

1. Kazunari Kurita, Takeshi Kadono, Ryosuke Okuyama, Ryo Hirose, Ayumi Onaka- Masada,Yoshihiro Koga and Hidehiko Okuda, "Proximity Gettering of Carbon Cluster Ion Implanted Silicon Wafers for CMOS Image Sensors," *Japanese Journal of Applied Physics*, Vol. 55, 2016, pp. 121301.

2. Ryosuke Okuyama, Ayumi Onaka-Masada, Takeshi Kadono, Ryo Hirose, Yoshihiro Koga, Hidehiko Okuda and Kazunari Kurita, "Trapping and diffusion kinetic of hydrogen in carbon-cluster ion-implantation projected range in Czochralski silicon wafers," *Japanese Journal of Applied Physics*, Vol. 56, 2017, pp. 025601.

3. Ryosuke Okuyama, Satoshi Shigematsu, Ayumi Onaka-Masada, Takeshi Kadono, Ryo Hirose, Yoshihiro Koga, Hidehiko Okuda and Kazunari Kurita, "Trapping and diffusion behaviour of hydrogen simulated with TCAD in projection range of carbon-cluster implanted silicon epitaxial wafers for CMOS image sensors," *Physica Status Solidi C: Current Topics in Solid State Physics*, 2017, pp. 170036.

4. Kazunari Kurita, Takeshi Kadono, Ryousuke Okuyama, Satoshi Shigematsu, Ryo Hirose, Ayumi Onaka-Masada,Yoshihiro Koga and Hidehiko Okuda, "Proximity gettering technology for advanced CMOS image sensors using carbon cluster ion-implantation technique : A review," *Physica Status Solidi A*, 2017, pp. 1700216.

5. Ryousuke Okuyama, Ayumi Masada, Satoshi Shigematsu, Takeshi Kadono, Ryo Hirose, Yoshihiko Koga, Hidehiko Okuda, and Kazunari Kurita, "Effect of dose and size on defect engineering in carbon cluster implanted silicon wafers," *Japanese Journal of Applied Physics*, Vol. 57, 2018, pp. 011301.

6. Ayumi Onaka-Masada, Toshiro Nakai, Ryosuke Okuyama, Hidehiko Okuda, Takeshi Kadono, Ryo Hirose, Yoshihiro Koga, Kazunari Kurita, and Koji Sueoka, "Effect of low-oxygen-concentration layer on iron gettering capability of carbon-cluster ion-implanted Si wafer for CMOS image sensors" *Japanese Journal of Applied Physics*, Vol. 57, 2018, pp. 021304.

7. Ryosuke Okuyama, Ayumi Onaka-Masada, Satoshi Shigematsu, Takeshi Kadono, Ryo Hirose, Yoshihiro Koga, Hidehiko Okuda, and Kazunari Kurita, "Diffusion kinetic of hydrogen in

CH_3O-molecular-ion-implanted silicon wafer for CMOS image sensors," *Japanese Journal of Applied Physics*, Vol. 57, 2018, pp. 081302.

8. Ayumi Onaka-Masada, Ryosuke Okuyama, Toshiro Nakai, Satoshi Shigematsu, Hidehiko Okuda, Koji Kobayashi, Ryo Hirose, Takeshi Kadono, Yoshihiro Koga, Masanori Shinohara, Koji Sueoka, and Kazunari Kurita, "Gettering mechanism in hydrocarbon-molecular-ion-implanted epitaxial silicon wafers revealed by three-dimensional atom imaging," *Japanese Journal of Applied Physics*, Vol. 57, 2018, pp. 091302.

9. Ayumi Onaka-Masada, Ryosuke Okuyama, Satoshi Shigematsu, Hidehiko Okuda, Takeshi Kadono, Ryo Hirose, Yoshihiro Koga, Koji Sueoka, and Kazunari Kurita, "Gettering Sinks for Metallic Impurities Formed by Carbon-Cluster Ion Implantation in Epitaxial Silicon Wafers for CMOS Image Sensor," *Journal of the Electron Devices Society*, Vol. 6, 2018, pp. 1200.

10. Yoshihiro Koga, Takeshi Kadono, Satoshi Shigematsu, Ryo Hirose, Ayumi Onaka-Masada, Ryousuke Okuyama, Hidehiko Okuda, and Kazunari Kurita, "Room-temperature bonding of epitaxial layer to carbon-cluster ion-implanted silicon wafers for CMOS image sensors," *Japanese Journal of Applied Physics*, Vol. 57, 2018, pp. 096503.

11. Ryo Hirose, Takeshi Kadono, Ryosuke Okuyama, Satoshi Shigematsu, Ayumi Onaka-Masada, Hidehiko Okuda, Yoshihiro Koga, and Kazunari Kurita "Proximity gettering of silicon wafers using CH3O multielement molecular ion implantation technique," *Japanese Journal of Applied Physics*, Vol. 57, 2018, pp. 061302.

12. Kazunari Kurita, Yoshihiro Koga, Ryousuke Okuyama, Takeshi Kadono, Satoshi Shigematsu, Ayumi Onaka Masada, Ryo Hirose, and Hidehiko Okuda, "(Invited) Proximity Gettering Design of Hydrocarbon Molecular Ion Implanted Silicon Wafers Using Direct Bonding Technique for Advanced CMOS Image Sensors: A Review," *ECS Transaction*, Vol. 86, 2018, pp. 77.

13. Ryosuke Okuyama, Ayumi Onaka-Masada, Akihiro Suzuki, Koji Kobayashi, Satoshi Shigematsu, Takeshi Kadono, Ryo Hirose, Yoshihiro Koga, and Kazunari Kurita, "Molecular and Atomic Hydrogen Diffusion Behavior by Reaction Kinetic Analysis in Projection Range of Hydrocarbon Molecular Ion for CMOS Image Sensors," *Physica Status Solidi A*, 2019, p. 1900175.

14. Akihiro Suzuki, Takeshi Kadono, Ryo Hirose, Ryosuke Okuyama, Ayumi Masada, Satoshi Shigematsu, Koji Kobayashi, Yoshihiro Koga,

and Kazunari Kurita, "Fundamental Characteristics of Cyanide-Related Multielement Molecular Ion-Implanted Epitaxial Si Wafers for High-Performance CMOS Image Sensors," *Physica Status Solidi A*, 2019, p. 1900172.

15. Kazunari Kurita, Takeshi Kadono, Satoshi Shigematsu, Ryo Hirose, Ryosuke Okuyama, Ayumi Onaka-Masada, Hidehiko Okuda and Yoshihiro Koga, "Proximity Gettering Design of Hydrocarbon-Molecular-Ion-Implanted Silicon Wafers Using Dark Current Spectroscopy for CMOS Image Sensors," *Sensors*, 19, 2019, p. 2073.

16. Ryo Hirose, Takeshi Kadono, Ryosuke Okuyama, Ayumi Onaka-Masada, Satoshi Shigematsu, Koji Kobayashi, Yoshihiro Koga, and Kazunari Kurita, "Proximity gettering technique using CH3O multielement molecular ion implantation for white spot defect density reduction in CMOS image sensor," *Japanese Journal of Applied Physics*, Vol. 58, 2019, pp. 091002.

17. Ryo Hirose, Ayumi Onaka-Masada, Ryosuke Okuyama, Takeshi Kadono, Satoshi Sigematsu, Koji Kobayashi, Akihiro Suzuki, Yoshihiro Koga, Jiro Matsuo, and Kazunari Kurita, *Japanese Journal of Applied Physics*, Vol. 58, 2019, pp. 121002.

18. Takeshi Kadono, Ryosuke Okuyama, Ayumi Onaka-Masada, Ryo Hirose, Satoshi Shigematsu, Yoshihiro Koga, Hidehiko Okuda, and Kazunari Kurita, "Effect of hydrocarbon molecular ion size for amorphous region formation analyzed by X-ray photoelectron spectroscopy" *Japanese Journal of Applied Physics*, Vol. 59, 2020, pp. 025510.

Oral Presentations in International Conferences

1. Ryosuke Okuyama, Ayumi Masada, Takeshi Kadono, Ryo Hirose, Yoshihiro Koga, Hidehiko Okuda and Kazunari Kurita, "Gettering Ability of Carbon Cluster Ion Implanted Epitaxial Silicon Wafers for Metal Impurities Contaminated Device Fabrication Process," in *The Scientific International Symposium on SIMS and Related Techniques Based on Ion-Solid Interactions(2016)*, 2016.

2. Ryo Hirose, Ryosuke Okuyama, Takeshi Kadono, Ayumi Onaka-Masada, Hidehiko Okuda, Yoshihiro Koga, Kazunari Kurita and Naoki Miyamoto, "Characteristics of Carbon Cluster Ion Implanted Epitaxial Silicon Wafers," in *21th International Conference on Ion Implantation Technology (IIT)*, NCK University, Taiwan, 2016.

3. Kazunari Kurita, Takeshi Kadono, Ryousuke Okuyama, Ryo Hirose, Ayumi Onaka-Masada, Satoshi Shigematsu, Hidehiko Okuda and Yoshihiko Koga, "Proximity Gettering Technology for Advanced CMOS Image Sensors Using Carbon Cluster Ion Implantation" in *Ninth International Meeting on Recent Developments in The Study of Radiation Effects in Matter*, 2016, Kyoto, Japan, 2016.

4. Kazunari Kurita, Takeshi Kadono, Ryousuke Okuyama, Ryo Hirose, Ayumi Onaka-Masada, Satoshi Shigematsu, Hidehiko Okuda and Yoshihiko Koga, "Proximity Gettering Technology for CMOS Image Sensors Using a Carbon Cluster Ion Implantation," in *The 7th International Symposium on Advanced Science and Technology of Silicon Materials (JSPS Si Symposium)*, 2016, Kona, Hawaii, USA, 2016.

5. Kazunari Kurita, Takeshi Kadono, Ryousuke Okuyama, Ryo Hirose, Ayumi Onaka-Masada, Satoshi Shigematsu, Hidehiko Okuda, and Yoshihiko Koga, "Proximity Gettering Technology for Advanced CMOS Image Sensors Using Carbon Cluster Ion Implantation Techniues," in *IEEE-EDTM (Electron Devices Technology and Manufacturing) 2017*, Toyama, Japan, 2017, p. 105.

6. Takeshi Kadono, Ryousuke Okuyama, Ryo Hirose ,Ayumi Onaka-Masada, Satoshi Shigematsu, Hidehiko Okuda, Yoshihiko Koga and Kazunari Kurita, "Impact of Hydrogen Annealing Behavior of C3H5 Carbon Cluster Ion Implanted Projection Range using Microwave heat treatment," in *IEEE-EDTM (Electron Devices Technology and Manufacturing) 2017*, Toyama, Japan, 2017, p. 61.

7. Satoshi Shigematsu, Ryosuke Okuyama, Ryo Hirose, Ayumi Masada, Takeshi Kadono, Yoshihiro Koga, Hidehiko Okuda, Kazunarai Kurita, "Oxygen Gettering Mechanism of Carbon Cluster Ion-Implanted Silicon Wafers for CMOS Image Sensors revealed by Three-Dimensional Laser-Assisted Atom Probe Tomography," in *The Scientific International Symposium on SIMS and Related Techniques Based on Ion-Solid Interactions*, 2017.

8. Kazunari Kurita, Takashi Kadono, Ryosuke Okuyama, Ryo Hirose, Ayumi Onaka-Masada, Satoshi Shigematsu, Hidehiko Okuda, Yoshihiro Koga, Kazunari Kurita, "Proximity gettering technology for advanced CMOS image sensors using carbon cluster ion implantation techniques," in *ICDS2017: 29th International Conference on Defect in Semiconducter*, 2017, Matsue, Japan.

9. Ryo Hirose, Takeshi Kadono, Ryosuke Okuyama, Satoshi Shigematsu, Ayumi Masada, Hidehiko Okuda, Yoshihiro Koga and Kazunari Kurita, "Development study of silicon epitaxial wafer for CMOS image sensors by using multi-element molecular cluster ion implantation," in *ICDS2017: 29th International Conference on Defect in Semiconducter*, 2017, Matsue, Japan.

10. Kazunari Kurita, Takeshi Kadono, Ryosuke Okuyama, Ryo Hirose, Ayumi Onaka-Masada, Satoshi Shigematsu, Hidehiko Okuda and Yoshihiro Koga, "Proximity gettering technology for advanced CMOS image sensors using carbon cluster ion implantation techniques," in *GADEST2017: Gettering and Defects Engineering in Semiconductor Technology*, Lopata, Georgia, 2017.

11. Ryosuke Okuyama, Ayumi Onaka-Masada, Takeshi Kadono, Ryo Hirose, Yoshihiro Koga, Hidehiko Okuda and Kazunari Kurita, "Trapping and diffusion behaviour of hydrogen simulated with TCAD in projection range of carbon-cluster implanted silicon epitaxial wafers for CMOS image sensors," in *GADEST2017: Gettering and Defects Engineering in Semiconductor Technology*, Lopata, Georgia, 2017.

12. Ayumi Onaka-Masada, Ryousuke Okuyama, Takeshi Kadono, Ryo Hirose, Satoshi Shigematsu, Hidehiko Okuda, Yoshihiko Koga and Kazunari Kurita, "Iron Gettering and Structural Characterization of Defects Formed in Carbon-cluster Ion Implanted Epitaxial Silicon Wafers," in *IEEE-EDTM (Electron Devices Technology and Manufacturing Conference) 2018*, Kobe, Japan, 2018, p. 166.

13. Satoshi Shigematsu, Ryosuke Okuyama, Ayumi Masada, Takeshi Kadono, Ryo Hirose, Yoshihiro Koga, Hidehiko Okuda, Kazunari Kurita, "Segregation Behavior around CH_3O Molecular Ion Implantation Related Extended Defects for CMOS Image Sensors," in *The Scientific International Symposium on SIMS and Related Techniques Based on Ion-Solid Interactions(2018)*, 2018.

14. Koji Kobayashii, Ryosuke Okuyama, Takeshi Kadono, Ryo Hirose, Ayumi Onaka-Masada, Satoshi Shigematsu, Yoshihiko Koga and Kazunari Kurita, "Re-crystallization Behavior of Amorphous Layer in Hydrocarbon Molecular Ion Implanted Region Using Flash Lamp Annealing," in *2018 22nd International Conference on Ion Implantation Technology (IIT)*, W΄urzburg, Germany, 2018, p. 357.

15. Kazunari Kurita, Takeshi Kadono, Ryosuke Okuyama, Ryo Hirose, Ayumi Onaka-Masada, Satoshi Shigematsu, Hidehiko Okuda and Yoshi-

hiko Koga, "Proximity Gettering Design of Silicon Wafers using Hydrocarbon Molecular Ion Implantation Technique for Advanced CMOS Image Sensors," in *2018 22nd International Conference on Ion Implantation Technology (IIT)*, W´urzburg, Germany, 2018, p. 275.

16. Kazunari Kurita, Yoshihiro Koga, Ryousuke Okuyama, Takeshi Kadono, Satoshi Shigematsu, Ayumi Onaka-Masad, Ryo Hirose and Hidehiko Okuda, "Proximity Gettering Design of Hydrocarbon Molecular Ion Implanted Silicon Wafers using Direct Bonding Technique for Advanced CMOS Image Sensors," in *2018 ECS and SMEQ Joint International Meeting*, Cancun, Mexico, 2018, p. 77.

17. Satoshi Shigematsu, Ryosuke Okuyama, Ayumi Masada, Takeshi Kadono, Ryo Hirose, Yoshihiro Koga, Hidehiko Okuda, Kazunari Kurita, "Gettering Behavior of Copper in Hydrocarbon Molecular Ion Implanted Silicon Wafers for CMOS Image Sensors Revealed by Atom Probe Tomography," in *14th International Conference on Atomically Controlled Surfaces, Interfaces and Nanostructures (ACSIN-14)*, Sendai, Miyagi, Japan, 2018, p. 23p-113.

18. Ryosuke Okuyama, Ayumi Onaka-Masada, Koji Kobayashi, Satoshi Shigematsu, Takeshi Kadono, Ryo Hirose, Yoshihiro Koga, Hidehiko Okuda, and Kazunari Kurita, "Diffusion behavior of hydrogen in molecular ion implanted silicon epitaxial wafers for advanced CMOS image sensor," in *The 8th Forum on the Science and Technology of Silicon Materials 2018*, Okayama, JAPAN, 2018.

19. Ryosuke Okuyama, Ayumi Onaka-Masada, Akihiro Suzuki, Koji Kobayashi, Satoshi Shigematsu, Ryo Hirose, Takeshi Kadono, Yoshihiro Koga, Kazunari Kurita, "Reaction kinetic analysis of hydrogen diffusion behaviour in hydrocarbon molecule ion implanted silicon wafers for advanced CMOS image sensors," in *GADEST2019: Gettering and Defects Engineering in Semiconductor Technology*, Zeuthen, Germany, 2019.

20. Akihiro Suzuki, Takeshi Kadono, Ryo Hirose, Ryosuke Okuyama, Ayumi Masada, Satoshi Shigematsu, Koji Kobayashi, Yoshihiro Koga, and Kazunari Kurita, "Fundamental Characteristics of Cyanide-Related Multielement Molecular Ion-Implanted Epitaxial Si Wafers for High-Performance CMOS Image Sensors," in *GADEST2019: Gettering and Defects Engineering in Semiconductor Technology*, Zeuthen, Germany, 2019.

21. Ryo Hirose, Takeshi Kadono, Ryosuke Okuyama, Ayumi Onaka-Masada, Satoshi Shigematsu, Koji Kobayashi, Yoshihiro Koga and Kazunari Kurita, "The effect of proximity gettering technology using CH_3O molecular ion implantation on CMOS image sensor fabrication process" in *22nd International Conference on Secondary Ion Mass Spectrometry (SIMS-22)*, Kyoto, Japan, 2019, p. 23-3-O4.

22. Satoshi Shigematsu, Ryosuke Okuyama, Ryo Hirose, Takeshi Kadono, Ayumi Onaka-Masada, Akihiro Suzuki, Koji Kobayashi, Hidehiko Okuda, Yoshihiro Koga, and Kazunari Kurita, "Influence of oxygen on copper gettering in hydrocarbon molecular ion implanted region using atom probe tomography" in *23rd International Workshop on Inelastic Ion-Surface Collisions (IISC-23)*, Matsue, Japan, 2019, p. 22-O-1.